

2013

# Design of reconfigurable multi-mode RF circuits

Xiaohua Yu  
Iowa State University

Follow this and additional works at: <https://lib.dr.iastate.edu/etd>



Part of the [Electrical and Electronics Commons](#)

## Recommended Citation

Yu, Xiaohua, "Design of reconfigurable multi-mode RF circuits" (2013). *Graduate Theses and Dissertations*. 13257.  
<https://lib.dr.iastate.edu/etd/13257>

This Dissertation is brought to you for free and open access by the Iowa State University Capstones, Theses and Dissertations at Iowa State University Digital Repository. It has been accepted for inclusion in Graduate Theses and Dissertations by an authorized administrator of Iowa State University Digital Repository. For more information, please contact [digirep@iastate.edu](mailto:digirep@iastate.edu).

**Design of reconfigurable multi-mode RF circuits**

by

**Xiaohua Yu**

A dissertation submitted to the graduate faculty  
in partial fulfillment of the requirements for the degree of  
**DOCTOR OF PHILOSOPHY**

Major: Electrical Engineering

Program of Study Committee:  
Nathan M. Neihart, Major Professor  
Degang Chen  
Aymen A. Fayed  
Jiming Song  
Sumit Chaudhary

Iowa State University  
Ames, Iowa  
2013

Copyright © Xiaohua Yu, 2013. All rights reserved.

## DEDICATION

To my parents

## TABLE OF CONTENTS

DEDICATION .....	ii
LIST OF FIGURES .....	v
LIST OF TABLES .....	ix
ACKNOWLEDGEMENTS .....	x
ABSTRACT .....	xi
CHAPTER 1. INTRODUCTION .....	1
1.1 Motivation .....	1
1.2 Review of Literature .....	5
1.2.1 Multi-band low noise amplifier .....	5
1.2.2 LC oscillator for multi-band applications .....	6
1.2.3 Application of transformers in LNA and VCO design .....	7
1.3 Dissertation Organization .....	8
CHAPTER 2. TRANSFORMER-BASED TUNABLE RESONATORS .....	9
2.1 Inductor-Based Resonators .....	9
2.2 Transformer-Based Resonators .....	15
2.2.1 Resonant frequency .....	15
2.2.2 Tuning methods .....	22
2.3 Summary .....	23
CHAPTER 3. DESIGN AND CHARACTERIZATION OF MULTI-TAP TRANSFORMERS .....	24
3.1 Transformer Basics .....	25
3.2 Multi-Tap Transformer .....	27
3.2.1 Design method .....	27
3.2.2 Modeling .....	30
3.2.3 Simulation results .....	31
3.3 Characterization of a Switched Multi-Tap Transformer .....	36
3.3.1 Analysis of the switch loss in a switched multi-tap transformer .....	36
3.3.2 Experimental results .....	40
3.4 Summary .....	47
CHAPTER 4. RECONFIGURABLE MULTIMODE LOW-NOISE AMPLIFIER USING A MULTITAP TRANSFORMER .....	49

4.1 Reconfigurable Multimode LNA .....	50
4.1.1 Multimode input matching network .....	51
4.1.2 Design strategy .....	55
4.1.3 Noise analysis .....	57
4.2 Circuit Details .....	60
4.2.1 Integrated multitap transformer .....	62
4.2.2 Simulation results .....	64
4.3 Experimental Results .....	68
4.4 Summary .....	75
<b>CHAPTER 5. TRANSFORMER-BASED TRIPPLE-MODE VOLTAGE CONTROLLED OSCILLATOR .....</b>	<b>76</b>
5.1 Multi-Frequency Oscillator .....	78
5.2 Operation of Dual-Coupled Triple-Mode VCO .....	80
5.2.1 Oscillation frequency and start-up conditions .....	81
5.2.2 Oscillation amplitude and stable oscillation condition .....	87
5.2.3 Choice of the coupling coefficient .....	91
5.3 Circuit Details and Experimental Results .....	93
5.4 Summary .....	105
<b>CHAPTER 6. CONCLUSIONS .....</b>	<b>106</b>
6.1 Contributions .....	106
6.2 Future Work .....	107
<b>BIBLIOGRAPHY .....</b>	<b>109</b>
<b>VITA .....</b>	<b>115</b>

## LIST OF FIGURES

Figure 1.1.	Next generation wireless device.....	2
Figure 1.2.	Block diagram of a reconfigurable SDR receiver with capability of concurrent dual-carrier reception. ....	3
Figure 2.1.	Schematic of (a) a parallel and (b) a series LC resonator.....	10
Figure 2.2.	Magnitude and phase of the impedance of (a) a parallel and (b) a series LC resonator.....	11
Figure 2.3.	Schematic of a series combination of (a) two parallel and (b) a parallel and a series resonators, and a parallel combination of (c) two series and (d) a parallel and a series resonators.....	13
Figure 2.4.	Magnitude and phase of the impedance of a series combination of (a) two parallel and (b) a parallel and a series resonators, and a parallel combination of (c) two series and (d) a parallel and a series resonators.....	14
Figure 2.5.	Schematic of (a) a parallel and (b) a series transformer-based LC resonator.....	15
Figure 2.6.	Magnitude and phase of the impedance of the resonator in Fig. 2.5 (a) with a switch as the tuning circuitry.....	17
Figure 2.7.	Resonant frequency vs. coupling coefficient, assuming the self-resonant frequency of tank is 3 GHz.....	17
Figure 2.8.	Resonant frequency vs. the current phase difference, assuming the self-resonant frequency of tank is 3 GHz.....	18
Figure 2.9.	Schematic of (a) a parallel and (b) a series transformer-based high order resonator.....	19
Figure 2.10.	Magnitude and phase of the impedance of (a) a parallel and (b) a series transformer-based high order resonator, shown in Fig. 2.9.....	20
Figure 2.11.	Resonant frequency vs. coupling coefficient, $k$ , for $\omega_L=2\pi*3$ GHz and $\omega_H=2\pi*5$ GHz. ....	20
Figure 2.12.	Contour plot showing how (a) $\omega_L$ and (b) $\omega_H$ changes as a function of $\omega_1$ and $\omega_2$ for a coupling coefficient, $k=0.5$ . ....	21
Figure 3.1.	Integrated spiral transformer (a) concentric, (b) interleaved, and (c) stacked.....	26

Figure 3.2. Symmetric 6-terminal multi-tap transformer (a) concentric and (b) interleaved .....	27
Figure 3.3. Multi-tap transformer segmentation (a) concentric half-winding, (b) interleaved half-winding, and (c) sub-segments of a half-winding.....	28
Figure 3.4. Symmetric multi-tap transformer model .....	30
Figure 3.5. Extraction setup for (a) self-inductance and (b) mutual inductance.....	32
Figure 3.6. Quality factor of primary, secondary and its sub-sections of the designed multi-tap transformer (a) concentric (b) interleaved.....	35
Figure 3.7. Simulation results of Momentum and the lumped-element model versus frequency for (a) self-inductance of the primary and each section of the secondary (b) mutual inductance between the primary and each section of secondary (c) mutual inductance between each section of the secondary. ....	35
Figure 3.8. Schematic of a switched multi-tap transformer.....	37
Figure 3.9. Simplified model for the analysis of the multi-tap transformer where the secondary is terminated using either (a) a short-circuit or (b) a capacitor. ....	38
Figure 3.10. Die photo of the switched multi-tap transformer. ....	41
Figure 3.11. (a) Equivalent inductance and (b) quality factor of the switched multi-tap transformer (solid line: post-layout simulation, dashed line: measured). ....	42
Figure 3.12. (a) Series and (b) parallel resonator with the switched multi-tap transformer as a tunable inductor ( $Z_L$ ).....	43
Figure 3.13. (a) Resonant frequency and (b) quality factor of the series resonator with variable control voltage of $V_{M1}$ and $V_{M2}$ when $C_1= 1$ pF. ....	44
Figure 3.14. (a) Resonant frequency (b) quality factor of the series resonator with variable control voltage of $V_{M3}$ when $C_1= 1$ pF.....	45
Figure 4.1. Input of (a) a conventional inductively degenerated LNA (b) the proposed multi-mode LNA with a reconfigurable multi-tap transformer as the gate inductor. ....	51
Figure 4.2. Transformer operating as inductor with secondary winding terminated with (a) an open, (b) a short, and (c) a capacitive load .....	52

Figure 4.3.	Plot of low-band and high-band resonant frequency as a function of capacitance $C_p$ for $L_1 = L_2 = 6.8$ nH, $L_{2a} = 1.7$ nH, $L_{2b} = 3.4$ nH, $k_a = 0.63$ , and $k_b = 0.87$ .....	56
Figure 4.4.	Noise model of the multi-mode LNA.....	58
Figure 4.5.	Schematic of the proposed multi-mode LNA.....	61
Figure 4.6.	(a) Multi-tap transformer layout, (b) broadband lumped-element model of the multi-tap transformer, (c) simulated equivalent inductance, and (d) quality factor of the multi-tap transformer with switches and capacitors (the region of operation are plotted in bold). ....	63
Figure 4.7.	Theoretical and simulated S11 for (a) mode 1, 2, and 4, (b) mode 3, and (c) mode 5.....	65
Figure 4.8.	Theoretical and simulated noise figure (a) mode 1, (b) mode 2, (c) mode 3, (d) mode 4, and (e) mode 5 (the shaded box denotes the desired band of operation).....	67
Figure 4.9.	Microphotograph of the LNA employing a multi-tap transformer. ....	68
Figure 4.10.	Measured and simulated $S_{11}$ and $S_{21}$ for (a) mode 1, (b) mode 2, (c) mode 3, (d) mode 4, and (e) mode 5. ....	69
Figure 4.11.	Measured and simulated noise figure for (a) mode 1, (b) mode 2, (c) mode 3, (d) mode 4, and (e) mode 5. ....	71
Figure 4.12.	Measured IIP3 of the proposed multi-mode LNA across the bands for all 5 modes. ....	72
Figure 5.1.	Schematic of a transformer-coupled triple-mode VCO [23]. ....	77
Figure 5.2.	Block diagram of a conceptual multi-frequency oscillator. ....	78
Figure 5.3.	Ideal output waveform of an oscillation oscillating at 3 GHz and 5 GHz simultaneously. ....	79
Figure 5.4.	Corresponding (a) current waveform following in the tank and (b) its frequency spectrum when the $g_m$ is realized with ideal switches and the ideal 4 <sup>th</sup> order tank has the same impedance at 3 GHz and 5 GHz. ....	79
Figure 5.5.	Schematic of the proposed dual-coupled triple-mode VCO.....	80
Figure 5.6.	Small signal model of the proposed triple mode VCO.....	81

Figure 5.7.	(a) Effective conductance of the primary inductor in the tank, and (b) real of the voltage ratio, $v_2/v_1$ , between secondary and primary turn (case 1: $L_1= 1.7$ nH, $R_1= 3.5$ $\Omega$ , $L_2= 3.4$ nH, $R_2= 3.8$ $\Omega$ , $k= 0.45$ , $f_1= 4.68$ GHz, $f_2= 3.2$ GHz; case 2: $L_1= 3.4$ nH, $R_1= 3.8$ $\Omega$ , $L_2= 1.7$ nH, $R_2= 3.5$ $\Omega$ , $k= 0.45$ , $f_1= 3.2$ GHz, $f_2= 4.68$ GHz). .....	85
Figure 5.8.	(a) Impedance and (b) phase of the tank with various $g_{m2}$ . .....	86
Figure 5.9.	Upper bound of the coupling coefficient, $k$ , vs. the frequency ratio, $\omega_H/\omega_L$ . .....	92
Figure 5.10.	Impedance of the tank with resonant frequencies of $\omega_L= 2\pi*3$ GHz, $\omega_H= 2\pi*5.6$ GHz for various coupling confidents, $k$ , for the configuration of $L_1= 1.7$ nH, $R_1= 3.5$ $\Omega$ , $L_2= 3.4$ nH, and $R_2= 3.8$ $\Omega$ . .....	92
Figure 5.11.	The extract (a) The self-inductance, (b) quality factor, and (c) coupling coefficient from the EM simulation and the lumped-element model. ....	94
Figure 5.12.	Microphotograph of the dual-coupled triple mode VCO. ....	95
Figure 5.13.	Measured output spectrum of (a) mode 1, single oscillation in high band, (b) mode 2, single oscillation in low band, and (c) mode 3, concurrent dual oscillation in both low and high band. ....	96
Figure 5.14.	Measured tuning range of (a) mode 1 ( $V_{t2}=0$ ), (b) mode 2 ( $V_{t2}=0$ : dashed line and $V_{t2}=1.2$ V: solid line), and (c) mode 3 for fixed $I_{t2}=0.2$ mA, (d) mode 3 for tunable $I_{t2}$ . .....	98
Figure 5.15.	Measured phase noise of (a) mode 1, single oscillation in high band, (b) mode 2, single oscillation in low band. ....	100
Figure 5.16.	Measured and simulated phase noise in mode 3. ....	101
Figure 5.17.	Simulated transient waveform of mode 3 (a) the differential output, (b) the output filtered by an ideal BPF centered at 5.3 GHz, and (c) the output filtered by an ideal BFP centered at 3.45 GHz. ....	102

## LIST OF TABLES

Table 3.1.	Comparison of transformer structures .....	26
Table 3.2.	Calculated and extracted parameters of 3:3 multi-tap transformers .....	33
Table 3.3.	Performance of the series and parallel LC resonator with a switched multi-tap transformer.....	46
Table 4.1.	Switch configuration for different modes of operation .....	54
Table 4.2.	Mode-dependent terms for noise factor calculation .....	60
Table 4.3.	Summary of LNA performance and comparison to previously published designs .....	74
Table 5.1.	Configuration of operation modes .....	86
Table 5.2.	Summary of VCO performance and comparison to previously published designs .....	104

## ACKNOWLEDGEMENTS

First and foremost, I wish to express my sincere appreciation to my advisor Dr. Nathan Neihart for his guidance and support over the last several years. He is more than a mentor, he is also a friend. He has made my years of Ph.D. life a wonderful journey. I have learned a lot from him which is going to help me in my professional career and personal life.

I would also like to thank my committee members for their guidance and encouragement: Dr. Degang Chen, Dr. Aymen Fayed, Dr. Jiming Song, and Dr. Sumit Chaudhary.

In addition, I would like to express my thanks to my friends, colleagues and anyone who helped me with various aspects of conducting this Ph.D. work.

Last, but not least, I would like to thank my parents and brother for their love, trust, and continuous support. My love and gratitude for them is forever.

## ABSTRACT

Wireless communication systems and devices have been developing at a much faster pace in the past few years. With the introduction of new applications and services and the increasing demand for higher data rate comes the need for new frequency bands and new standards. One critical issue for next generation wireless devices is how to support all of the existing and emerging bands while not increasing the cost and power consumption. A feasible solution is the concept of the software-defined radio where a single receiver can be reconfigured to operate in different modes, each of which supports one or several bands and/or standards. To implement such a reconfigurable receiver, reconfigurable RF building blocks, such as the LNA, mixer, VCO, etc., are required. This dissertation focuses on two key blocks: the low noise amplifier (LNA) and the voltage controlled oscillator (VCO).

First the design, modeling and characterization of a multi-tap transformer are discussed. Simple mathematical calculations are utilized to estimate the inductances and coupling coefficients from the physical parameters of a multi-tap transformer. The design method is verified with several designed multi-tap transformers that are characterized up to 10 GHz using Momentum simulation results. The effect of switch loss on a switched multi-tap transformer is explored and a broadband lumped-element model of the multi-tap transformer is also proposed.

Next a reconfigurable multimode LNA capable of single-band, concurrent dual-band, and ultra-wideband operation is presented. The multimode operation is realized by incorporating a switched multi-tap transformer into the input matching network of an inductively degenerated common source amplifier. The proposed LNA achieves single band

matching at 2.8, 3.3, and 4.6 GHz; concurrent dual-band matching at 2.05 and 5.65 GHz; and ultra-wideband matching from 4.3 to 10.8 GHz. The chip was fabricated in a 0.13  $\mu\text{m}$  CMOS process, and occupies an area of 0.72  $\text{mm}^2$ , and has a power dissipation of 6.4 mW from a 1.2-V supply.

Finally, a triple-mode VCO using a transformer-based 4<sup>th</sup> order tank with tunable transconductance cells coupling the primary and secondary inductor is introduced. The tank impedance can be re-shaped by the transconductance cells through the tuning of their biasing currents. With the control of biasing current, VCO is configured in three modes, capable of generating a single frequency in 3- and 5- GHz bands, respectively, and two frequencies in both 3- and 5- GHz bands simultaneously. The triple-mode VCO was fabricated in a 0.13  $\mu\text{m}$  CMOS process, occupies an area of 0.16  $\text{mm}^2$ , and dissipates 5.6 mW from a 1.2-V supply.

## CHAPTER 1. INTRODUCTION

### 1.1 Motivation

Wireless communication systems have developed dramatically in the past few years as the increased demand of mobile devices for online social networking, web surfing, voice and video calling, video streaming, online gaming, etc.. The support of 2G/3G cellular feature, global positioning system (GPS) navigation, Bluetooth, Wireless Local Area Network (WLAN), is becoming more and more common in a ubiquitous mobile device. Recently, new features, such as support of 4G Long Term Evaluation (LTE), near field communication (NFC), etc., are being added to the wireless devices. To support the different applications, a wireless device needs to cover a wide frequency ranges because each application corresponds to one or several different standard operating in different frequency bands. For example, the prominent 2G/3G cellular phone supports global system for mobile communications (GSM), code division multiple access (CDMA), wideband code division multiple access (WCDMA) in the bands of 850-, 900-, 1700-, 1900-, and 2100-MHz. Besides those frequencies, some extra bands, such as in 700-, 1500-, 2300-, and 2600-MHz etc., have been added for 4G LTE. With further development of 4G LTE, the support of much more bands will be expected as a total of 43 bands have been proposed in the standard. Like the cellular feature, the WLAN also requires the support of different standards. The prominent standards are IEEE 802.11 a/b/g/n in 2.4- and 5- GHz and the next generation WLAN standard, IEEE802.11 ac, is being developed. As the development of wireless technology, a

next generation wireless device, as shown in Fig. 1.1, is likely to support these existing and emerging standards, such as GSM/CDMA/WCDMA/LTE, WLAN (IEEE 802.11 a/b/g/n/ac), GPS, Bluetooth, WiMax, Wireless HD, NFC, etc..

With the ever increasing number of standards and applications for wireless communication systems comes the need for multi-band multi-standard radios. A straight forward way to implement such radios is to employ parallel narrowband receiver paths. Unfortunately, this approach suffers from significant problems with power consumption, die area, etc. In order to reduce the power consumption and lower hardware cost, it is desirable

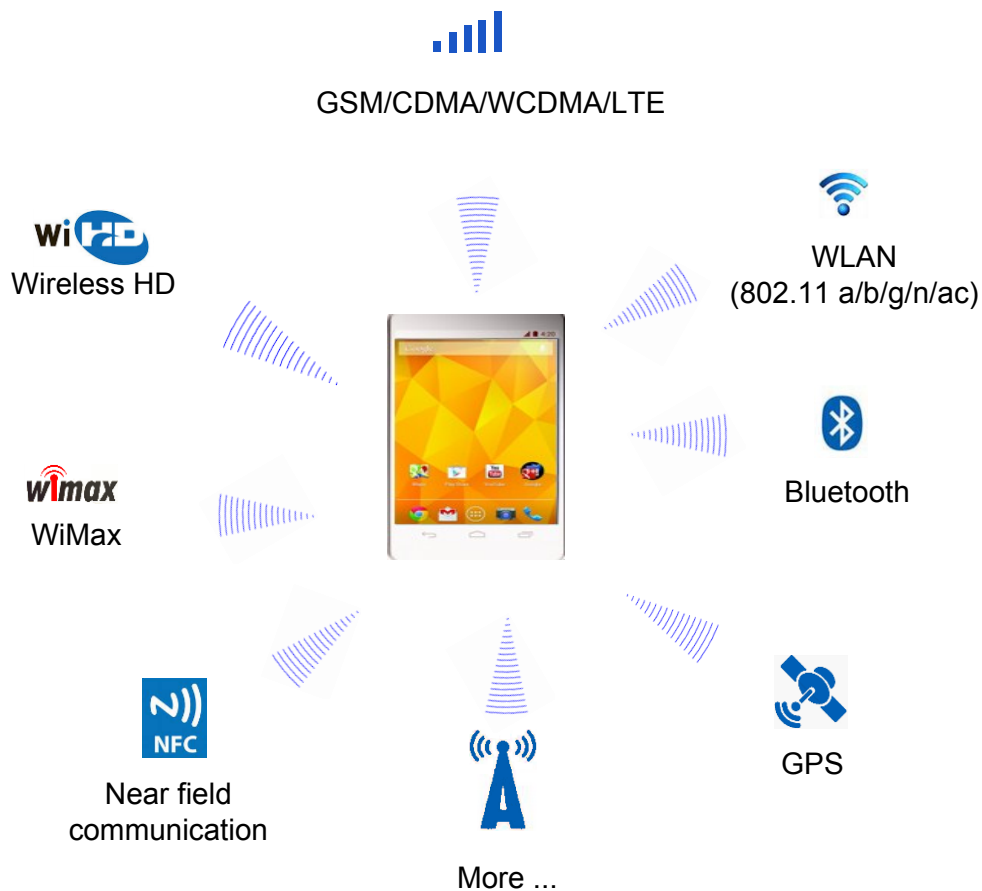


Figure 1.1. Next generation wireless device.

to use a single radio system capable of multi-band multi-standard communication. One multi-band multi-standard radio platform that has gained a lot of attention in recent years is the software defined radio (SDR). Ideally, a SDR receiver would be reconfigurable to receive a channel of arbitrary bandwidth and frequency. Moreover, successful SDR implementations should be capable of receiving two or more channels concurrently [1].

A reconfigurable SDR receiver with the capability of receiving two carriers simultaneously is illustrated in Fig. 1.2. The low noise amplifier amplifies the incoming signal in the covered bands with minimum degradation of signal-to-noise-ratio (SNR) while providing input matching. The mixer down converts the amplified signal to baseband. The phase lock loop (PLL) selects the signal channel. The receiver may receive signals carried by a single center frequency, typically called carrier frequency or simply carrier. The receiver

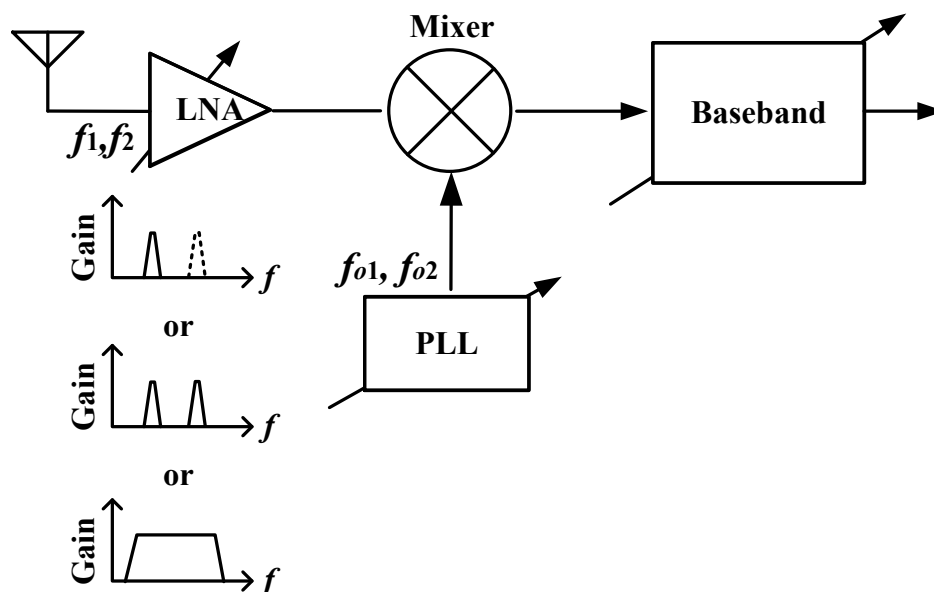


Figure 1.2. Block diagram of a reconfigurable SDR receiver with capability of concurrent dual-carrier reception.

may also be configured to receive signals simultaneously carried by two different carrier frequencies using carrier aggregation mechanism [2]. The signals with two carrier frequencies may be received either in a single band, named dual-carrier intra-band reception, or in two different bands, named dual-carrier inter-band reception, where a band is defined as a small contiguous frequency range that is used for the same application. In the single carrier and intra-band dual-carrier case, the receiver operates similarly to a traditional single-carrier, single-band receiver, where the low noise amplifier (LNA) just need cover one band at a time and the PLL just needs to provide a single local oscillator signal. While in the inter-band dual-carrier case, the LNA and mixer need cover two bands at a time and the PLL need provide local oscillation signal with two different frequency components simultaneously. To successfully realize such a SDR receiver, it requires flexible reconfigurable building blocks that are area and power efficient.

The LNA as the first building block determines the operating frequency range of the receiver. The LNA is required to cover all desired frequency bands; however, signals in all covered bands could enter the receiver, acting as in-band interferences and causing severe distortion. It is desirable that a LNA can provide a wide range of operating frequencies thus allowing multi-band and wideband operation as well as out-of-band filtering. This would enable SDR systems to smartly choose the operation mode of the LNA depending on the intended application and surrounding RF environment.

Another challenging block that limits the operating frequency range of the receiver is the PLL, which typically consists of a phase detector, a loop filter, an oscillator, and a frequency divider. The output frequency range of a PLL is primarily determined by the tuning range of the oscillator. In order to support concurrent reception, the oscillator is

required to generate LO signals for all carriers. A straight forward solution is to use to an oscillator for each band, while a cost-effective solution is to use a single oscillator for all bands.

Ideally, the LNA and the oscillator are able to cover any band either one at a time or simultaneously. A practical application would be limited to multiple single band and concurrent dual-band. This research investigates the two building blocks, LNA and VCO, in a multi-standard multi-band receiver that can be reconfigured to operate either in a single band mode or in concurrent-dual band mode.

## 1.2 Review of Literature

### 1.2.1 Multi-band low noise amplifier

Several techniques exist for increasing the operating range of the LNA. The most straightforward approach is to use a wideband LNA capable of spanning all of the desired frequency bands [1, 3-5]. In addition to covering a wide range of frequencies, wideband LNAs also allow for the concurrent reception of multiple disparate frequencies. This is also the source of a primary drawback, however; out-of-band interferers are not filtered but are passed along with the desired signal. This places stringent linearity requirements on the LNA and subsequent RF stages [1, 3, 6, 7]. In an effort to improve the linearity, [6] proposed the use of a current mode LNA thereby eliminating any RF voltage gain. Blocker-elimination was achieved in [6] by implementing impedance-filtering at the LNA and mixer outputs to reduce the out-of-band voltage gain. These approaches relax the linearity requirements for the subsequent stages, but at the cost of requiring a relatively high out-of-band linearity for the LNA.

Traditionally, the linearity requirement of the RF front-end is relaxed by attenuating the out-of-band interferers via filtering at the input of the LNA. A narrow-band LNA with a tunable matching network was proposed in [8] as an alternative to the wideband LNA. Not only are narrow-band, tunable LNAs limited to receiving a single frequency band, the tuning range tends to be too narrow for use in SDR systems. As a compromise between the relaxed linearity of the tunable narrow-band architecture and the ability to receive multiple frequency bands simultaneously, concurrent dual-band LNA architectures, capable of supporting two frequency bands simultaneously, were proposed in [9, 10]. Unfortunately, these systems still suffer from severe tradeoffs between the number of supported bands and the attenuation of out-of-band interferers.

### **1.2.2 LC oscillator for multi-band applications**

LC Oscillator is well-known for its superior phase noise and is the most popular oscillator topology in modern RFICs [11]. In multi-band applications, wide-tuning range oscillators are desirable. Several techniques are proposed to extend the frequency range of oscillator. The oscillation frequency is traditionally tuned with a combination of varactors and switched capacitor banks. However, the tuning range is limited due to parasitic capacitance and the phase noise requirement [1]. Multi-tap inductors [12-14], inductor- and transformer-based high-order resonant tanks [15-19], and magnetic tuning method [20] are proposed to expand the tuning range of a LC oscillator. Though the tuning range of the oscillators has been extended to several GHz with above techniques, only a single frequency can be generated at a time in those reported oscillators.

While there are so many works on the multi-band and wide-tuning range VCO, concurrent resonant oscillators have yet not drawn much attention and there is only few works reported [21-23]. In [21], a concurrent oscillator implemented in printed circuit board (PCB) was reported to generate two synchronous frequencies. Common-emitter oscillator topology was adopted, thus only single-end output was available. A total of four resonators were used to sustain the concurrent dual oscillation. In [22], an integrated circuit version of concurrent dual-frequency oscillator was realized in SiGe BiCMOS technology, generating two asynchronous frequencies simultaneously. Differential Hartley oscillator topology was used to offer differential outputs. Significant area was occupied by the five inductors that were used to form a high order resonator. Moreover, the oscillator was realized with the BJT transistors and is not able to be integrated into a CMOS chip. In [23], two coupled oscillators using a transformer was proposed to realize a concurrent and dual-band oscillator in CMOS technology. The transformer-based high order tank helped reducing the chip area to  $0.4 \times 0.575 \text{ mm}^2$ . However, two current nodes and a voltage node need to be controlled. Besides, a special voltage range is needed for the voltage node to ensure concurrent dual oscillation.

### **1.2.3 Application of transformers in LNA and VCO design**

Recently, transformers attract lots of attention in LNA and VCO design for its intrinsic characteristic of inductive feedback [4, 5, 19, 20, 24, 25] and the ability to form a high order resonator [15-18, 26, 27]. The adoption of transformers in the VCO design is a natural evaluation from the LC oscillator. Transformer was used for magnetically tuning in [19, 20, 25] to extend the tuning range and in [24] to realize differential tuning to achieve good common-mode noise rejection. Transformer was also used in [15-18] to realize a multi-

mode VCO, where the transformer formed a high order tank. The mode switching was realized with reconfigurable capacitors connecting the two transformer windings [15, 16] and with switched transconductances [17, 18]. The tuning range is greatly extended with the help of mode switching besides the use of switched capacitor banks. Inspired from its ability of extending the tuning range of an oscillator, transformers are adopted in the wideband LNA design, where transformer is typically used to achieve wideband input matching. In [4, 5], the wideband input matching was achieved with gate-source and source-drain reactive feedback, respectively, which also helped to boost the gain and improve the noise figure. Wideband and dual band input matching were also reported using a transformer-based high order network in [10, 26].

### **1.3 Dissertation Organization**

The dissertation is organized as follows. Chapter 2 begins with a review of inductor and transformer-based resonators. The resonant frequency, quality factor, and the frequency tuning methods of the transformer-based resonator will be discussed. Chapter 3 introduces the design methods and the broadband model of multi-tap transformers that are validated using Agilent's Advanced Design System (ADS) Momentum simulation and a fabricated switched multi-tap transformer. Chapter 4 presents a reconfigurable multi-mode LNA utilizing a multi-tap transformer capable of single-band, concurrent dual band, and wideband operation, which is verified with a prototype LNA. Chapter 5 demonstrates a triple-mode VCO capable of generating a single frequency signal in two different bands and a signal with two asynchronous tones simultaneously. Finally, Chapter 6 summarizes the research contributions and discusses the future work.

## CHAPTER 2. TRANSFORMER-BASED TUNABLE RESONATORS

Inductors have been widely used in various RF circuits, such as LNAs, VCOs, etc., to obtain proper operation in the desired bands by resonating with the intended capacitors and unwanted parasitic capacitors. With the increasing demand to support more frequency bands, the number of inductors will significantly increase, resulting in larger chip area and higher cost. The operation of transformers, consisting of magnetically coupled inductors, is based on the mutual inductance between those coupled inductors [28]. Transformers not only carry all characteristics of inductors but also save area and bring new characteristics such as reactive feedback and DC isolation. Transformers can be a favorable area-saving option to replace multiple inductors in the LC resonators.

The resonant frequency and quality factor are the key characteristics of a resonator. This chapter will focus on the resonant frequency and tuning method of a resonator, while its quality factor will be discussed in Chapter 3. In this chapter, Inductor-based resonators will be first reviewed in Section 2.1. Then, transformer-based resonators will be analyzed in the form of resonant frequency, quality factor, and tuning methods in Section 2.2. Finally, Section 2.3 will conclude and summarize this chapter.

### 2.1 Inductor-Based Resonators

A basic parallel and a basic series LC resonator are shown in Fig. 2.1. The parallel resonator consists of an inductor,  $L_p$ , and a capacitor,  $C$ . The resistor,  $R_p$ , represents the equivalent parallel parasitic resistor of the inductor,  $L_p$ . The series resonator consists of an

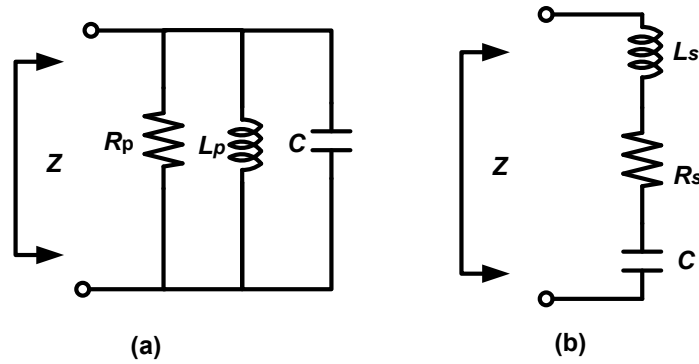


Figure 2.1. Schematic of (a) a parallel and (b) a series LC resonator.

inductor,  $L_s$ , and a capacitor,  $C$ . The resistor,  $R_s$ , represents the equivalent series parasitic resistor of the inductor,  $L_s$ . In both resonators, the parasitic resistor of the capacitor is neglected as its quality factor is typically much larger than the quality factor of an inductor.

The impedance of the two resonators can be expressed as

$$Z_p = \frac{sL_p}{s^2L_pC + sL_p/R_p + 1} \quad (2-1)$$

$$Z_s = sL_s + R_s + \frac{1}{sC} \quad (2-2)$$

The magnitude and phase of the parallel and series resonators are illustrated in Fig. 2.2. It can be seen that the parallel resonator appears like an open circuit at its resonant frequency  $\omega_p$ , which is desirable for a tank in a VCO and at the output of a LNA, and the series resonator appears like a short circuit at its resonant frequency  $\omega_s$ , which is applicable to the input matching network of a LNA. The resonant frequencies are calculated as

$$\omega_p = \frac{1}{\sqrt{L_pC}} \quad (2-3)$$

$$\omega_s = \frac{1}{\sqrt{L_sC}} \quad (2-4)$$

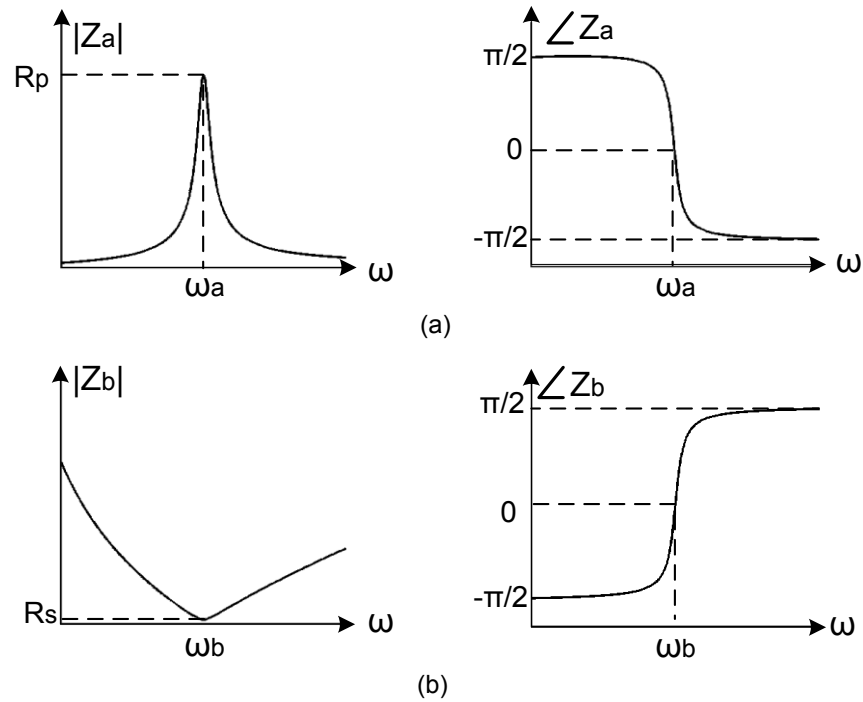


Figure 2.2. Magnitude and phase of the impedance of (a) a parallel and (b) a series LC resonator.

respectively. The quality factor of the tank is primarily determined by the quality factor of the inductors. At their resonant frequency, the quality factors are expressed as:

$$Q_p = \frac{R_p}{\omega_p L_p} \quad (2-5)$$

$$Q_s = \frac{\omega_s L_s}{R_s} \quad (2-6)$$

,respectively.

A combination of the parallel and series resonators, either in series or in parallel, can form a high order resonator, as shown in Fig. 2.3. The impedance of each combination can be calculated as

$$Z_a = \frac{sL_1}{s^2 L_1 C_1 + sL_1/R_1 + 1} + \frac{sL_1}{s^2 L_1 C_1 + sL_1/R_1 + 1} \quad (2-7)$$

$$Z_b = \frac{sL_1}{s^2L_1C_1 + sL_1/R_1 + 1} + sL_2 + R_2 + \frac{1}{sC_2} \quad (2-8)$$

$$Z_c = \frac{\left(sL_1 + R_1 + \frac{1}{sC_1}\right)\left(sL_2 + R_2 + \frac{1}{sC_2}\right)}{s(L_1 + L_2) + R_1 + R_2 + \frac{C_1 + C_2}{sC_1C_2}} \quad (2-9)$$

$$Z_d = \frac{sL_1\left(sL_2 + R_2 + \frac{1}{sC_2}\right)}{sL_1 + (s^2L_1C_1 + sL_1/R_1 + 1)\left(sL_2 + R_2 + \frac{1}{sC_2}\right)} \quad (2-10)$$

The resonant frequencies of the two tanks are given as:

$$\omega_1 = \frac{1}{\sqrt{L_1C_1}} \quad (2-11)$$

$$\omega_2 = \frac{1}{\sqrt{L_2C_2}} \quad (2-12)$$

Assuming  $\omega_1 < \omega_2$ , the magnitude and phase of the impedance of the high order tanks in Fig. 2.3 are illustrated in Fig. 2.4. It is seen that there are two poles and one zero in  $Z_a$  and  $Z_d$ , while there are one pole and two zeros in  $Z_b$  and  $Z_c$ . Assuming the quality factor of the inductors is high, the two poles in  $Z_a$  and the two zeros in  $Z_c$  approximately equal to the resonant frequencies of the two tanks,  $\omega_1$  and  $\omega_2$ , respectively. The zero in  $Z_a$  and the pole in  $Z_c$  is approximated as

$$\omega_z = \omega_1\omega_2\sqrt{\frac{L_1 + L_2}{L_1\omega_2^2 + L_2\omega_1^2}} \quad (2-13)$$

The two zeros in  $Z_b$  and the two pole in  $Z_d$  are approximately given as

$$\omega_L = \sqrt{\frac{\omega_1^2 + \omega_2^2 + \omega_3^2 - \sqrt{(\omega_1^2 + \omega_2^2 + \omega_3^2)^2 - 4\omega_1^2\omega_2^2}}{2}} \quad (2-14)$$

$$\omega_H = \sqrt{\frac{\omega_1^2 + \omega_2^2 + \omega_3^2 + \sqrt{(\omega_1^2 + \omega_2^2 + \omega_3^2)^2 - 4\omega_1^2\omega_2^2}}{2}} \quad (2-15)$$

where  $\omega_3 = 1/\sqrt{L_1 C_2}$  or  $\omega_3 = 1/\sqrt{L_2 C_1}$ . The pole in  $Z_b$  and the zero in  $Z_d$  locates at  $\omega_1$  and  $\omega_2$ , respectively. The above analysis implies that dual-band operation is possible for a LNA and a VCO with the tanks illustrated in Fig. 2.3. The configuration in Fig. 2.3 (a) and (d) may be applied as the tank of a dual-band or wide tuning range VCO [22, 29, 30] and the configuration in Fig. 2.3 (b) and (c) may be applied to the input matching network of a dual-band or wideband LNA [9].

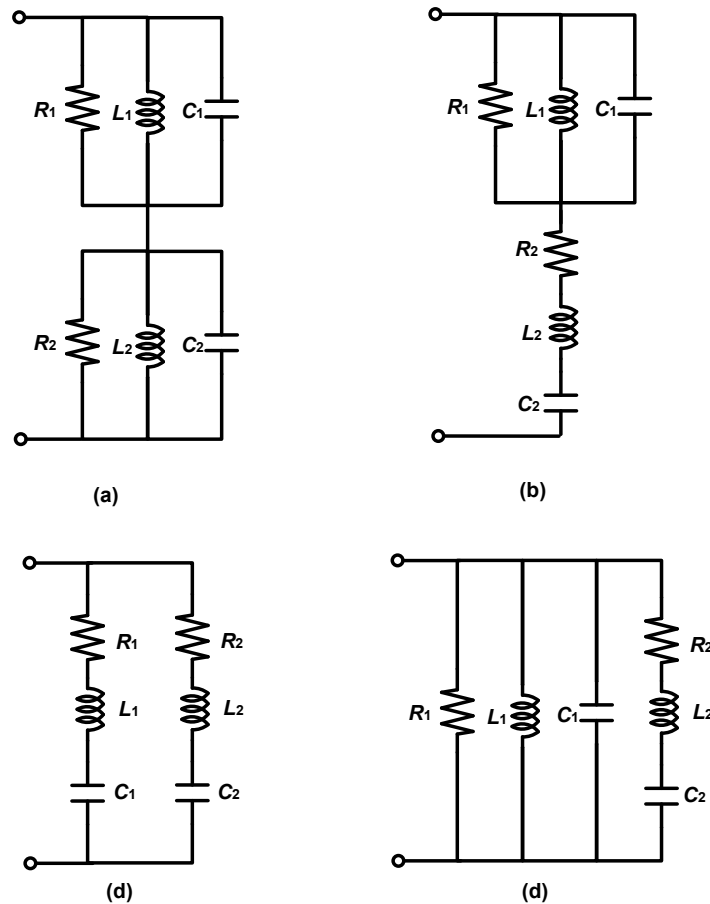


Figure 2.3. Schematic of a series combination of (a) two parallel and (b) a parallel and a series resonators, and a parallel combination of (c) two series and (d) a parallel and a series resonators.

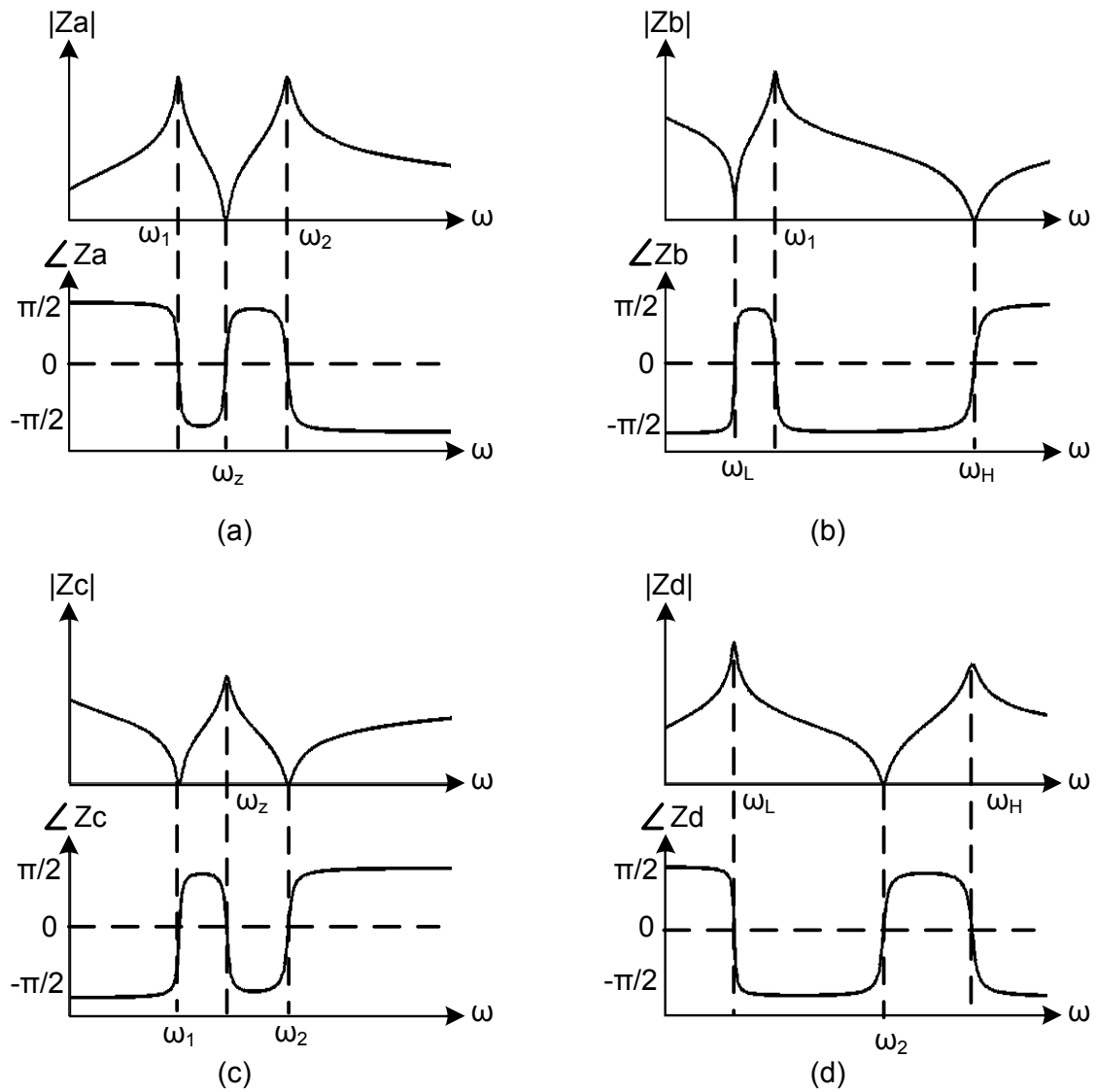


Figure 2.4. Magnitude and phase of the impedance of a series combination of (a) two parallel and (b) a parallel and a series resonators, and a parallel combination of (c) two series and (d) a parallel and a series resonators.

## 2.2 Transformer-Based Resonators

A transformer, consisting of coupled inductors, may be used to replace the inductor in a LC resonator in the design of LNAs [4, 10, 26, 31, 32], band-pass filters [33, 34], and VCOs [15-20, 23, 25, 35]. The transformer-based resonators can be easily tuned and be configured to a high order resonator because of the magnetically coupling among the inductors, which is normally characterized using mutual inductance,  $M$ , or coupling coefficient,  $k$ .

### 2.2.1 Resonant frequency

The schematic of a parallel and a series transformer-based second order resonator, consisting of a primary inductor  $L_1$ , a secondary inductor,  $L_2$ , and a capacitor,  $C_1$ , are shown in Fig. 2.5. The coupling coefficient between  $L_1$  and  $L_2$  is denoted as  $k$ . The primary inductor and the capacitor form a second order LC resonator the same as the LC resonator, shown in Fig. 2.1, and the magnitude and phase of the impedance is also similar as shown in Fig. 2.2. A key characteristic of the transformer-based resonator is that the inductance of the primary

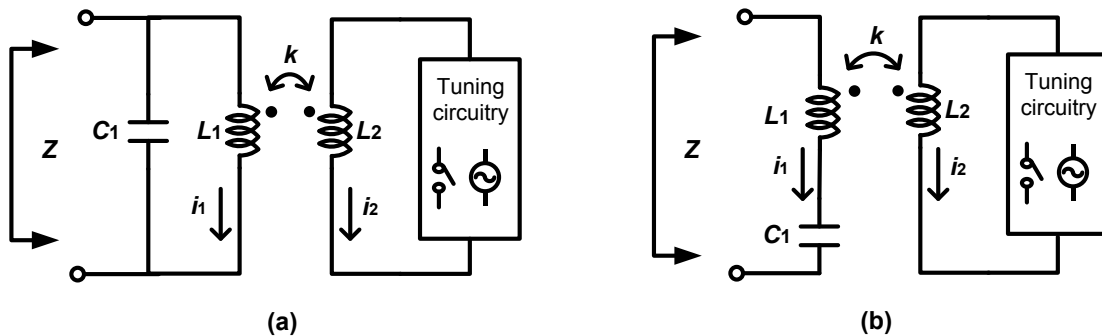


Figure 2.5. Schematic of (a) a parallel and (b) a series transformer-based LC resonator.

inductor can be tuned by the current flowing in the secondary inductor,  $i_2$ , which is determined by the tuning circuitry, such as a switch, an AC current source, etc.. The impedance of the parallel and series resonator is express as

$$Z_p = \frac{sL'_1}{s^2L'_1C+1} \quad (2-16)$$

$$Z_s = sL'_1 + \frac{1}{sC} \quad (2-17)$$

where  $L'_1$  is the effective inductance of the primary inductor, and  $L'_1 = L_1 + Re\left(\frac{i_2}{i_1}\right)k\sqrt{L_1L_2}$ .

The resonant frequency is calculated as:

$$\omega'_1 = \frac{1}{\sqrt{L'_1C_1}} \quad (2-18)$$

When the secondary is shorted by a switch,  $L'_1 = L_1(1 - k^2)$ . The resonant frequency is shifted from  $\omega_1$  to a higher frequency,  $\omega_1/\sqrt{1 - k^2}$ . As an example, the amplitude and phase of the impedance of the parallel resonator Fig. 2.5 (a) are compared when a switch is turned on and off, and are plotted in Fig. 2.6. A plot of the resonant frequency as a function of  $k$  is shown in Fig. 2.7, assuming the self-resonant frequency of the tank is 3 GHz.

When  $i_2$  is controlled by an AC current source,  $L'_1$  will be also determined by the relative amplitude and phase between  $i_1$  and  $i_2$  for a given transformer. A plot of the resonant frequency over the relative phase between  $i_1$  and  $i_2$  at different current amplitude ratios is illustrated in Fig. 2.8. The resonant frequency increases as the relative phase increases. The frequency also increases as the current amplitude ratio increases when the relative phase is larger than 90 degree, but the frequency decreases as the current amplitude ratio increases when the relative phase within 90 degree. The frequency reaches minimum frequency when

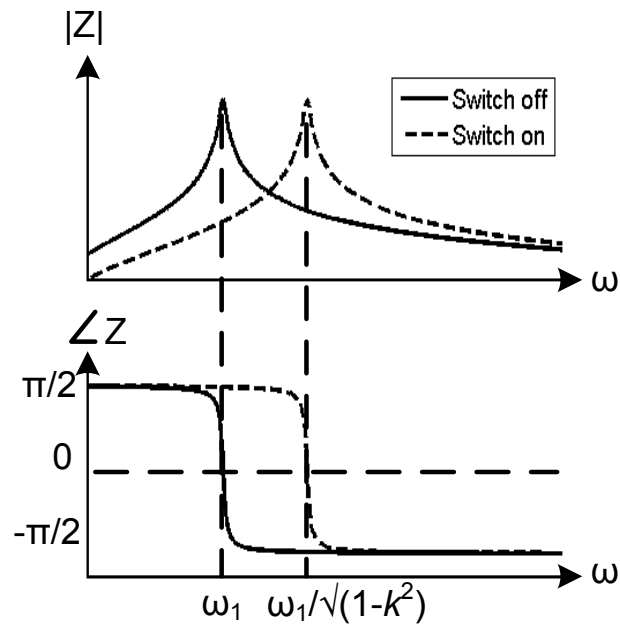


Figure 2.6. Magnitude and phase of the impedance of the resonator in Fig. 2.5 (a) with a switch as the tuning circuitry.

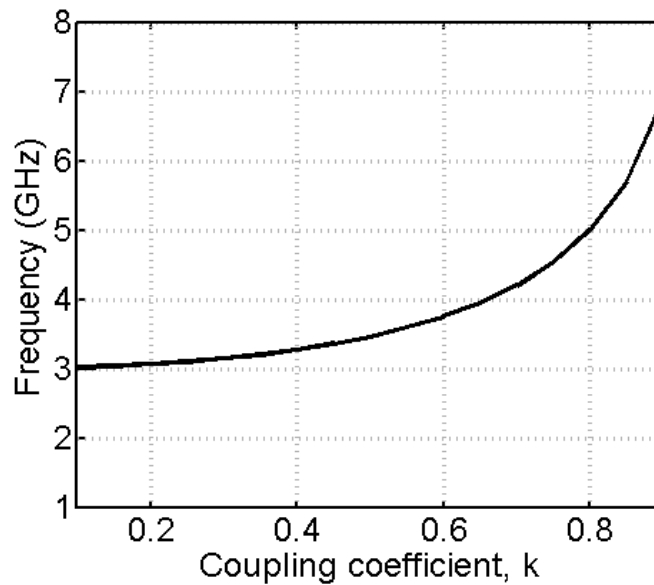


Figure 2.7. Resonant frequency vs. coupling coefficient, assuming the self-resonant frequency of tank is 3 GHz.

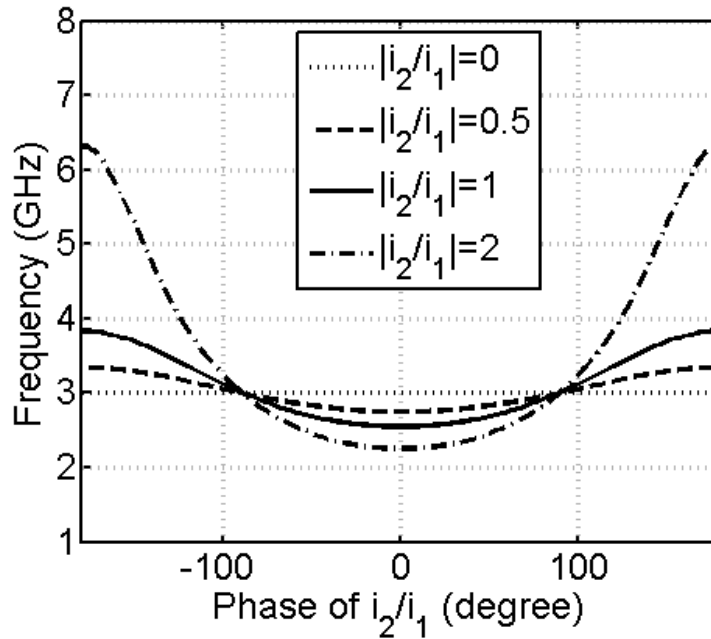


Figure 2.8. Resonant frequency vs. the current phase difference, assuming the self-resonant frequency of tank is 3 GHz.

the currents are in phase and reaches maximum frequency when the current are out-of phase. It is worth to mention that when  $i_1$  and  $i_2$  are not in-phase and out-of phase, extra loss is added to the primary inductor.

Transformer can also replace the inductor to form a high order resonator. The schematic of a parallel and a series transformer-based high order resonator, consisting of a primary inductor  $L_1$ , a secondary inductor,  $L_2$ , two capacitors,  $C_1$  and  $C_2$ , are shown in Fig. 2.9. The coupling coefficient between  $L_1$  and  $L_2$  is  $k$ . The self-resonant frequency of the primary and secondary tank are  $\omega_1 = 1/\sqrt{L_1 C_1}$  and  $\omega_2 = 1/\sqrt{L_2 C_2}$ , respectively. The impedance of the parallel and series resonator is express as

$$Z_{p1} = \frac{sL_1(1+s^2L_2C_2(1-k^2))}{s^2L_1C_1(1+s^2L_2C_2(1-k^2))+s^2L_2C_2+1} \quad (2-19)$$

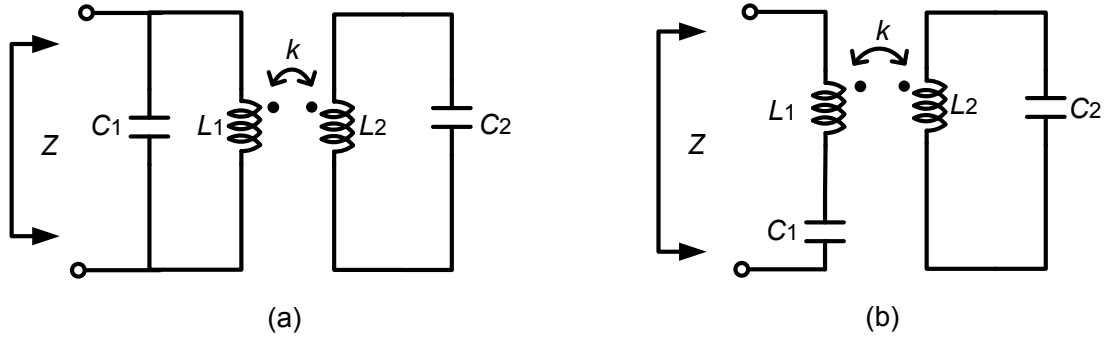


Figure 2.9. Schematic of (a) a parallel and (b) a series transformer-based high order resonator.

$$Z_{s1} = sL_1 \frac{1+s^2L_2C_2(1-k^2)}{s^2L_2C_2+1} + \frac{1}{sC_1} \quad (2-20)$$

The magnitude and phase of the impedance of the resonators shown in Fig. 2.9 are illustrated in Fig. 2.10, showing that there are two frequencies at which the impedance of the parallel resonant tank is maximized and the impedance of the series tank is minimized. The two frequencies correspond to the resonant frequency of the two high order tanks and can be expressed as:

$$\omega_L = \sqrt{\frac{\omega_1^2 + \omega_2^2 - \sqrt{(\omega_1^2 - \omega_2^2)^2 + 4k^2\omega_1^2\omega_2^2}}{2(1-k^2)}} \quad (2-21)$$

$$\omega_H = \sqrt{\frac{\omega_1^2 + \omega_2^2 + \sqrt{(\omega_1^2 - \omega_2^2)^2 + 4k^2\omega_1^2\omega_2^2}}{2(1-k^2)}} \quad (2-22)$$

The resonant frequencies depend on the self-resonant frequencies of the two tanks,  $\omega_1$  and  $\omega_2$ , and the coupling coefficient,  $k$ . For a given set of  $\omega_1$  and  $\omega_2$ ,  $\omega_L$  and  $\omega_H$  separate more when  $k$  increases, as shown in Fig. 2.11. For a fixed  $k$ , a contour plot of the  $\omega_L$  and  $\omega_H$  with respect to  $\omega_1$  and  $\omega_2$  (assuming  $\omega_1 < \omega_2$ ) is shown in Fig. 2.12. It clearly shows that the  $\omega_L < \omega_1 < \omega_2 < \omega_H$  and the resonant frequencies increases as  $\omega_1$  and  $\omega_2$  become larger.

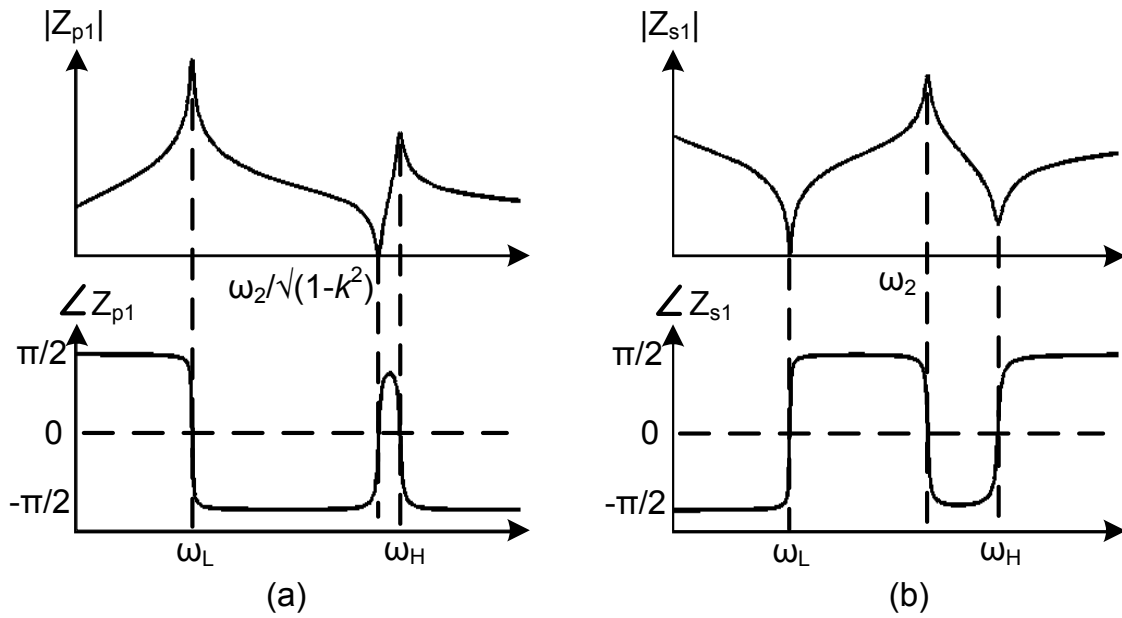


Figure 2.10. Magnitude and phase of the impedance of (a) a parallel and (b) a series transformer-based high order resonator, shown in Fig. 2.9.

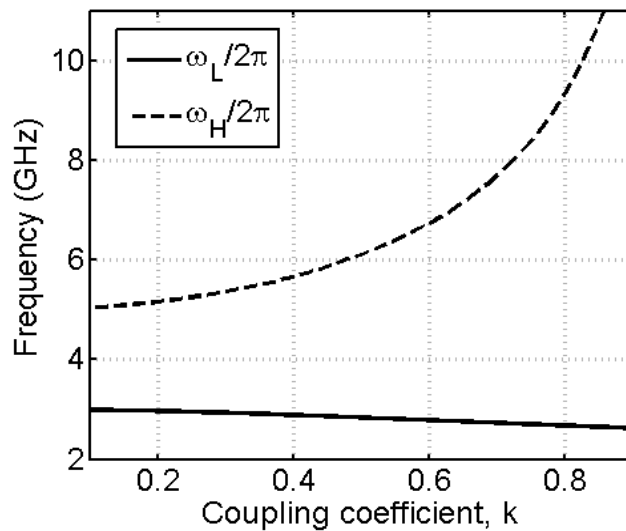


Figure 2.11. Resonant frequency vs. coupling coefficient,  $k$ , for  $\omega_L=2\pi*3$  GHz and  $\omega_H=2\pi*5$  GHz.

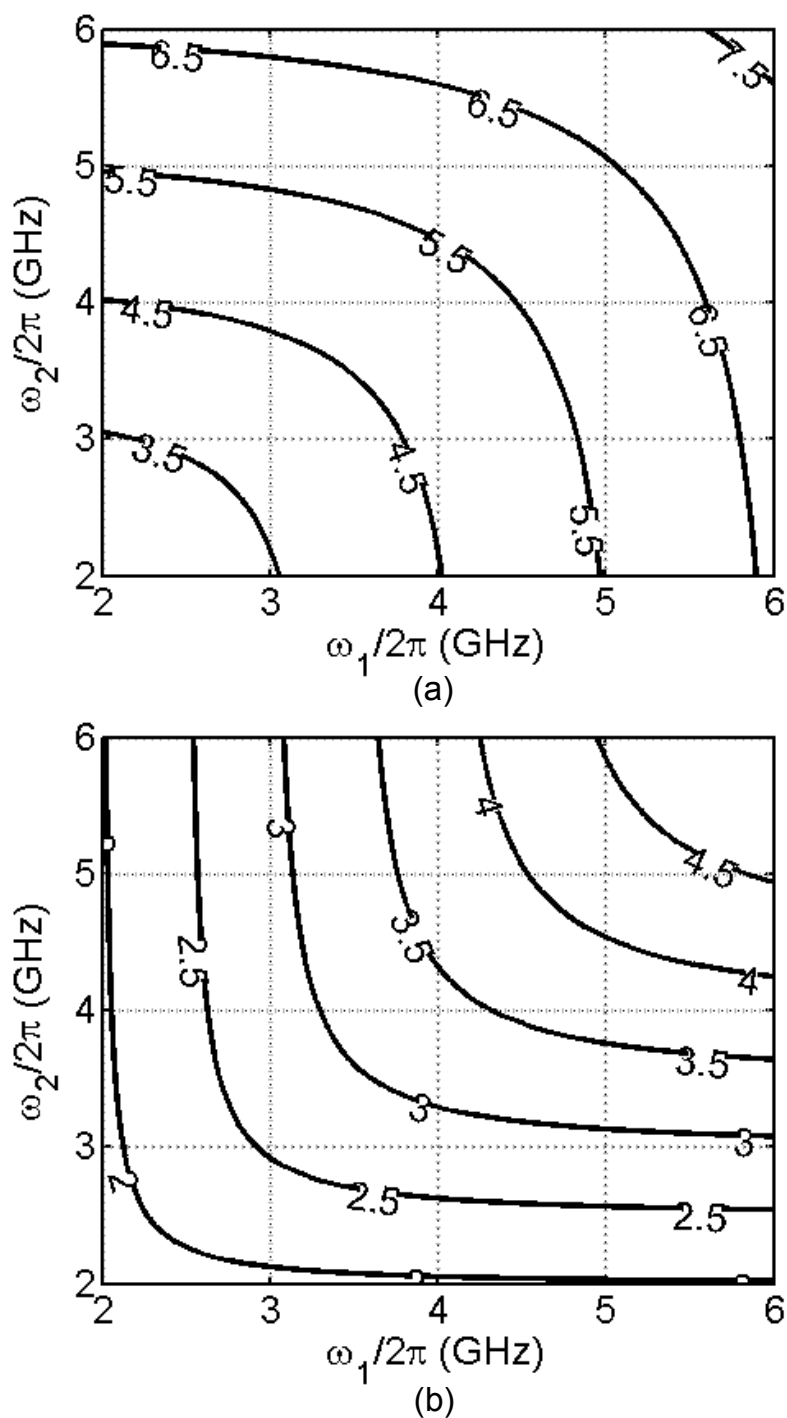


Figure 2.12. Contour plot showing how (a)  $\omega_L$  and (b)  $\omega_H$  changes as a function of  $\omega_1$  and  $\omega_2$  for a coupling coefficient,  $k=0.5$ .

## 2.2.2 Tuning methods

As discussed in Section 2.2.1, the resonant frequency of a transformer-based resonator is determined by the self-resonant frequency of the primary and secondary tank, the coupling coefficient, the termination of the secondary inductor, etc.. Thus, the resonant frequency may be tuned by changing any of the related factors. Based on whether the frequency tuning requires additional current consumption, the tuning methods may be divided into two groups: passive tuning and active tuning.

Passive tuning is the most popular frequency tuning method of a resonator as it does not consume extra current. It may be realized through tuning the capacitance, switching the active cores connected to the resonator, terminating the secondary switch a switch, adopting a multi-tap and a multi-coupled transformer, etc.. Traditionally, the passive tuning is primary referred to capacitive tuning using a varactor and switched capacitor banks [15-18, 25, 35, 36] because the degradation of the resonator's quality factor is minimized under the fact that the quality factor of a capacitor is typically much larger than an inductor. Besides the capacitive tuning, the frequency tuning in the design of VCOs may be achieved by reconfiguring the negative transconductance connected to a transformer-based resonator [16-18]. A switch termination in the secondary inductor is used for resonant frequency switching when the circuit is not sensitive to the quality factor degradation, such as a very frequency tank where the quality factor of the capacitor is comparable or worse than that of the inductor [19], an input matching network where a low quality factor of the tank is acceptable [32], etc.. The inductance and the coupling coefficient may also be controlled by adopting a multi-tap transformer [37] and a transformer with more than three coupled inductors [19].

The frequency tuning can also be realized with active tuning by consuming extra current in the secondary inductor, as shown in Fig. 2.5, where the control circuitry is a controlled current source. The controlled current may be a feedback current controlled by the output of an amplifier[31], a feedback current triggered by the quadrature output in a Quadrature VCO [20], a feedback current self-controlled by the transformer [33, 34], etc..

### 2.3 Summary

Inductor- and transformer-based LC resonators in the form of second order and high order configurations are investigated regarding their tank impedance and resonator frequencies. In the transformer-based resonators, the effector of different terminations of the secondary inductor, the coupling coefficient,  $k$ , and the self-resonant frequencies of the primary and secondary tanks, are also analyzed. Based on the analysis of the resonant frequencies, the frequency tuning methods, both passive and active tuning, are summarized.

## CHAPTER 3. DESIGN AND CHARACTERIZATION OF MULTI-TAP TRANSFORMERS

Multi-band radio architectures are an attractive solution for multi-standard communication. In a multi-band radio, on-chip inductors and transformers are widely used in various key blocks, such as the low noise amplifier, voltage-controlled oscillators (VCO), etc., to obtain proper operation in each of the desired bands. Inductors and transformers are, however, the most area consuming devices due to the fact that passives do not scale with technology. With the increasing demand to support more frequency bands, the number of inductors and transformers will significantly increase, resulting in larger chip area and higher cost. To save area and reduce cost, while retaining the necessary functionality, multi-port inductors have been adopted by some designers for use in switchable band-selective loads [38], LC ladders for distributed amplifiers [39], and dual-resonant tanks in voltage-controlled oscillators [13, 14]. Recently, multi-tap transformers have also been proposed as a shared input and output balun [40] and for reconfigurable multi-mode input matching [41].

A primary challenge in utilizing multi-port inductors and multi-tap transformers in RFIC design is the lack of well-designed and characterized devices. Though there have been many papers focusing on the design, modeling, and characterization of conventional integrated inductors and transformers [42-45], there have been relatively few papers focusing on the modeling and characterization of multi-port inductors [13, 14, 39], and virtually no work has been published that addresses the characterization and modeling of multi-tap transformers.

In this chapter, the design and characterization of multi-tap transformers will be investigated. Section 3.1 first reviews the basics of transformers. Then, a new design method for quickly evaluating many different transformer designs is presented along with a broadband lumped-element model in Section 3.2. Two 3:3 multi-tap transformers are designed and characterized to verify the design method and the model. A switched multi-tap transformer will be analyzed regarding the switch loss in Section 3.3. Its effect on the resonance frequency and quality factor (Q) of LC resonators with the switched multi-tap transformer will be discussed with simulated and measured results. Finally, Section 3.4 will summarize this chapter.

### 3.1 Transformer Basics

The conventional transformer is a four terminal device, consisting of two magnetically coupled inductors, which are typically called primary and secondary inductor or coil, respectively. The transformer provides voltage, current, and impedance transformation between primary and secondary inductor through magnetically coupling while offering complete DC isolation between them. There are three configurations for integrated transformers: concentric, interleaved, and stacked, shown in Fig. 3.1. In a concentric transformer configuration (Fig. 3.1(a)), the magnetic coupling is relatively weak because the common periphery between the primary and secondary windings is limited to a single turn. The interleaved and stacked configuration (Fig. 3.1(b) and (c)), on the other hand, experience coupling between each turn of the primary and secondary windings and hence have a strong coupling interaction. The stacked configuration is very area efficient because of the overlapping of primary and secondary coil. Its area is only the same as a single inductor..

However, the stacked transformer needs to be implemented using lower metal layers for the secondary coil, thus low quality factor is expected for its secondary coil and its self-resonant frequency is also reduced due to larger parasitic capacitance to the substrate. Comparing to the stacked structure, both primary and secondary coil of the concentric and interleaved transformer can be designed using the top metal, thus good quality factor as well as high self-resonant frequency can be achieved. But, both the concentric and interleaved transformer occupy larger area when the primary and secondary coils are implemented using a same metal layer. The tradeoff among the coupling coefficient, quality factor, self-resonant frequency, area, etc. must be considered when designing a transformer. The tradeoffs for the three structures are summarized in Table 3.1. These tradeoffs also apply to the multi-tap transformers that will be discussed later in this chapter.

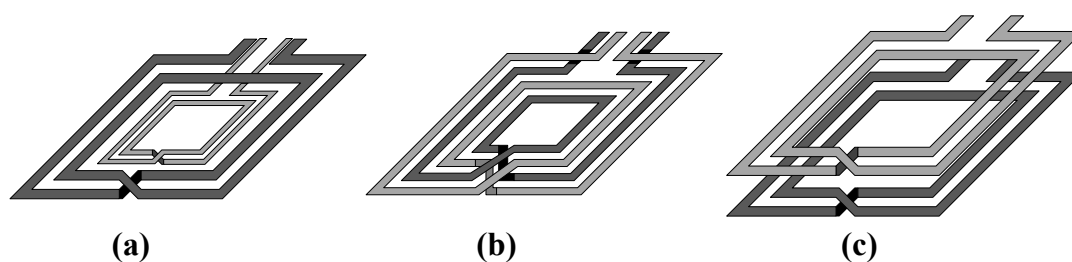


Figure 3.1. Integrated spiral transformer (a) concentric, (b) interleaved, and (c) stacked

Table 3.1. Comparison of transformer structures

Structure	Quality factor	Self-resonant frequency	Area efficiency	Coupling factor $k$
Concentric	+	+	—	Small
Interleaved	+	+	—	Large
Stacked	—	+	+	Large

## 3.2 Multi-Tap Transformer

### 3.2.1 Design method

Grover partial inductance calculations [46] were adopted in [45] to allow for the rapid evaluation of many different conventional integrated transformer designs. A similar tool is presented herein for the rapid evaluation of different physical designs for multi-tap transformers. Two different 3:3 symmetric multi-tap transformers are used as design examples. The structures of Fig. 3.2(a) and Fig. 3.2(b) can be broken down into half-windings, as shown in Fig. 3.3(a) and Fig. 3.3(b), respectively. Half-windings 1-6 belong to the primary, 7-10 are the middle section of the secondary, and 11 and 12 are the head and tail section of the secondary, respectively. Each half-winding is further divided into five sub-segments as shown in Fig. 3.3(c).

The partial self-inductance of a sub-segment and the partial mutual inductance between

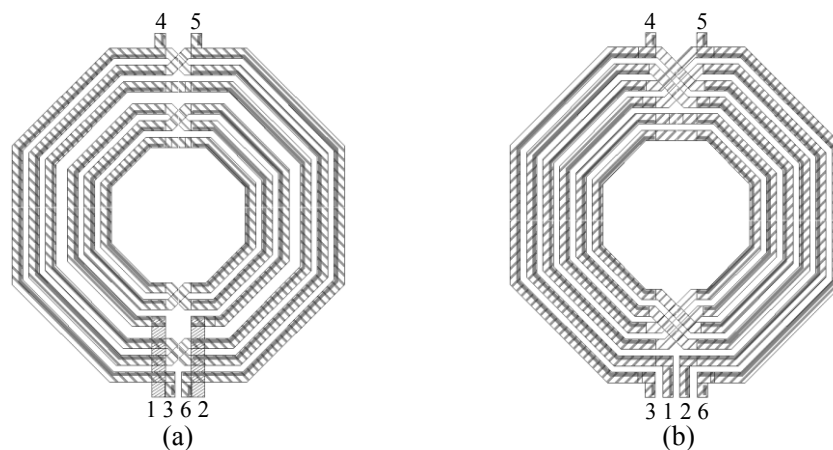


Figure 3.2. Symmetric 6-terminal multi-tap transformer (a) concentric and (b) interleaved

two sub-segments can be calculated by applying the equations developed in [45, 46]. With the calculated partial inductances of the sub-segments, the partial self-inductance of a half-winding and the partial mutual inductance between half-windings can be obtained. These inductances can be further summed to calculate the self-inductances of the primary and secondary winding of the transformer and the mutual-inductances between them. The self-inductances of the 3:3 symmetric multi-tap transformer are calculated as :

$$L_p = \sum_{j=1}^6 (L_j + 2 \sum_{k=j+1}^6 M_{j,k}) \quad (3-1)$$

$$L_{s1} = L_{11} = L_{12} \quad (3-2)$$

$$L_{s2} = \sum_{j=7}^{10} (L_j + 2 \sum_{k=j+1}^{10} M_{j,k}) \quad (3-3)$$

where  $L_p$  is the total inductance of the primary,  $L_{s1}$  is the total inductance of the head (and tail) section of the secondary,  $L_{s2}$  is the total inductance of the middle section of the secondary,  $L_j$  is the partial self-inductance of the  $j^{\text{th}}$  half-winding, and  $M_{j,k}$  is the partial

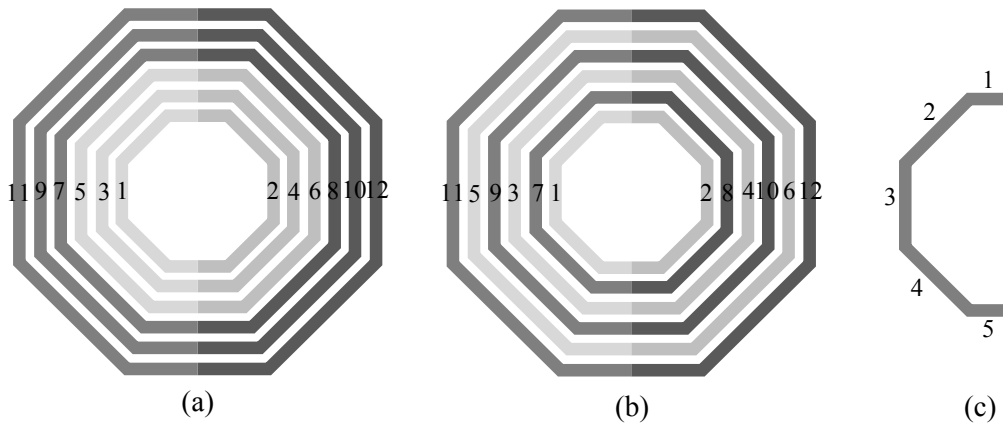


Figure 3.3. Multi-tap transformer segmentation (a) concentric half-winding, (b) interleaved half-winding, and (c) sub-segments of a half-winding

mutual-inductance between the  $j^{\text{th}}$  and  $k^{\text{th}}$  half-windings. The total mutual-inductances of the example transformer are found by:

$$M_{p,s1} = \sum_{j=1}^6 M_{j,11} = \sum_{j=1}^6 M_{j,12} \quad (3-4)$$

$$M_{p,s2} = \sum_{j=1}^6 \sum_{k=7}^{10} M_{j,k} \quad (3-5)$$

$$M_{s1,s1} = M_{11,12} \quad (3-6)$$

$$M_{s1,s2} = \sum_{j=7}^{10} M_{j,11} = \sum_{j=7}^{10} M_{j,12} \quad (3-7)$$

where  $M_{p,s1}$  and  $M_{p,s2}$  are the mutual inductance between inductors  $L_p$  and  $L_{s1}$  and inductors  $L_p$  and  $L_{s2}$ , respectively;  $M_{s1,s1}$  is the mutual inductance between the head ( $L_{s1}$ ) and tail ( $L_{s1}$ ) inductors of the secondary; and  $M_{s1,s2}$  is the mutual inductance between the head/tail and the center section of the secondary (i.e.,  $L_{s1}$  and  $L_{s2}$ ).

The total inductance of the secondary winding,  $L_s$ , and mutual inductance between the primary and secondary,  $M_{p,s}$ , can also be calculated by:

$$L_s = \sum_{j=7}^{12} (L_j + 2 \sum_{k=j+1}^{12} M_{j,k}) \quad (3-8)$$

$$M_{p,s} = \sum_{j=1}^6 \sum_{k=7}^{12} M_{j,k}. \quad (3-9)$$

Once all of the self- and mutual-inductances have been calculated, the various coupling coefficients can be obtained using the relationship:

$$k_{1,2} = \frac{M}{\sqrt{L_1 L_2}}. \quad (3-10)$$

Using (3-1)-(3-10), the designer is able to quickly and efficiently evaluate different physical realizations of the multi-tap transformer and estimate the resulting winding inductances and coupling coefficients. This greatly speeds up the design cycle by reducing the number of iterations between layout and Momentum simulations..

### 3.2.2 Modeling

A broadband, lumped-element model is often required in order to perform circuit-level simulations in both the time and frequency domain. A compact, lumped-element model of the proposed multi-tap transformer is shown in Fig. 3.4. It is based on previously proposed inductor and balun models [42, 44] and consists of a  $\pi$ -network modeling the primary inductor, and three series  $\pi$ -networks modeling the secondary inductor. The magnetic coupling between each section is accounted for by the inclusion of coupling coefficient  $k_{p,s1}$ ,

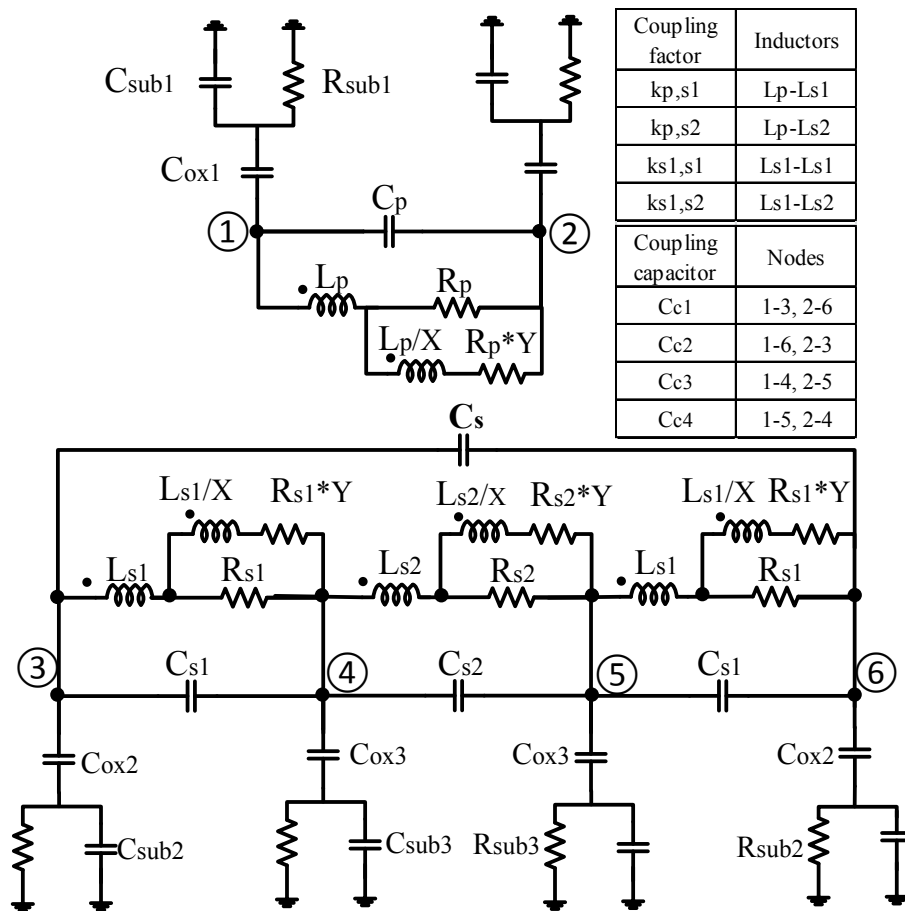


Figure 3.4. Symmetric multi-tap transformer model

$k_{p,s2}$ ,  $k_{s1,s1}$ , and  $k_{s1,s2}$ , and capacitive coupling between each terminal is modeled by coupling capacitors  $C_{c1}$ ,  $C_{c2}$ ,  $C_{c3}$ , and  $C_{c4}$ . The skin effect is modeled by a  $R$ - $L$  ladder in parallel with the series resistor  $R_S$ . The  $R$ - $L$  ladder models the metal surface layer [42] and the inductance and resistance in the ladder are scaled by a factor of  $1/X$  and  $Y$ , respectively, which are empirically fit using optimization tools.

### 3.2.3 Simulation results

Two 3:3 transformers (one concentric and one interleaved structure) were designed in an 8-metal 0.13 $\mu$ m CMOS RF process using the methods described in Section 3.2.1. The targeted inductances of the multi-tap concentric transformer are  $L_p = 2$  nH,  $L_{s1} = 0.4$  nH, and  $L_{s2} = 1.7$  nH; and the targeted coupling coefficients are  $k_{p,s1} = 0.22$  and  $k_{p,s2} = 0.45$ . Using (3-1)-(3-10), it is found that an outer diameter of 270  $\mu$ m, a metal width of 8.5  $\mu$ m, and a metal spacing of 5  $\mu$ m will result in the desired values for inductance and coupling coefficient. The resulting layout is shown in Fig. 3.2(a). The interleaved multi-tap transformer, shown in Fig. 3.2(b), was also designed with the same physical parameters for comparison. The calculated inductances are  $L_p = 2.2$  nH,  $L_{s1} = 0.4$  nH, and  $L_{s2} = 1.23$  nH. The coupling coefficients are  $k_{p,s1} = 0.3$  and  $k_{p,s2} = 0.59$ .

The designed symmetric multi-tap transformers were characterized from DC to 10 GHz with Agilent's ADS Momentum simulator. The required inductances, coupling coefficients, and  $Q$ -factors were extracted from the 6-port S-parameters.

Fig. 3.5 illustrates the setup that was used to extract the self-inductance and mutual inductance of the multi-tap transformer. The terminal numbering matches that shown in Fig. 3.2 and Fig. 3.4. The self-inductance is extracted with the simulation setup depicted in Fig.

3.5(a), in which terminal 1 is connected to a  $50 \Omega$  port and terminal 2 is shorted to ground while leaving all other terminals floating. From the one-port S-parameter simulation, the self-inductance,  $L$ , is given by:

$$L = \frac{\text{Im}(Z_{11})}{2\pi f}. \quad (3-11)$$

The mutual inductance,  $M$ , between two sections is extracted with the 2-port S-parameter simulation setup depicted in Fig. 3.5(b), and is given by:

$$M = \frac{\text{Im}(Z_{12})}{2\pi f}. \quad (3-12)$$

The two multi-tap transformers are characterized in three different configurations: 6-terminal, 5-terminal, and 4-terminal. This demonstrates the intrinsic re-configurability of a multi-tap transformer; i.e., a 6-terminal multi-tap transformer can also operate as a conventional 4-terminal or 5-terminal transformer. Table 3.1 details the resulting self-inductances and coupling coefficients that are extracted at 2.4 GHz with S-parameters obtained from Agilent's ADS Momentum simulation of the layout.

The simulated primary inductances for concentric and interleaved transformers are

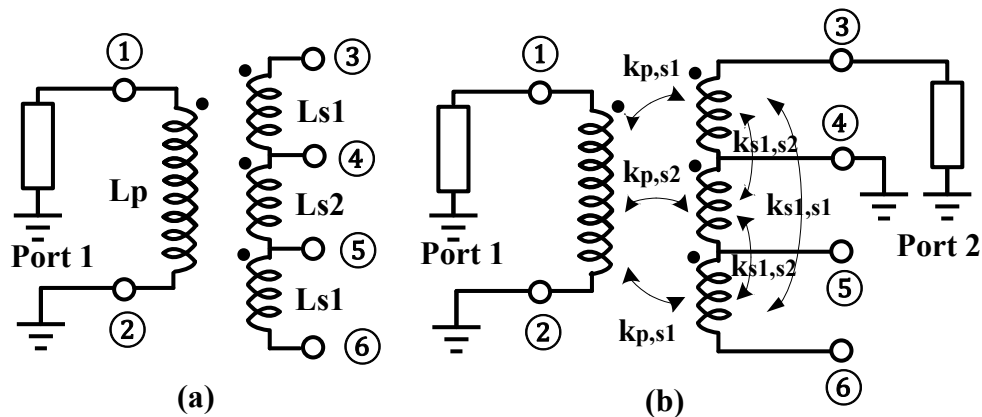


Figure 3.5. Extraction setup for (a) self-inductance and (b) mutual inductance

1.676 nH and 1.933 nH, respectively, and are the same for all test configurations. As expected, the inductances of the secondary and coupling coefficients depend upon the test configuration (i.e., 6-port, 5-port, or 4-port) demonstrating the potential for using multi-tap transformers in reconfigurable applications. The simulation results show that the multi-tap interleaved transformer exhibits a larger coupling coefficient than the concentric transformer, which is expected from analysis of traditional 4-port concentric and interleaved transformers.

Compared to the initial calculated results, it can be seen in Table 3.2 that the results of the calculations presented in Section 3.2.1 closely estimate the inductances and coupling coefficients of the different multi-tap transformers. The simulated inductances are only about 10-20% less than the theoretical values, which is partially due to simplification of the cross-

Table 3.2. Calculated and extracted parameters of 3:3 multi-tap transformers

Type	Parameter	Concentric		Interleaved	
		Theory	Sim.	Theory	Sim.
All	$L_p$ (nH)	2	1.676	2.2	1.933
6-terminal	$L_{s1}$ (nH)	0.4	0.315	0.4	0.317
	$L_{s2}$ (nH)	1.7	1.578	1.23	1.103
	$k_{p,s1}$	0.22	0.219	0.3	0.373
	$k_{p,s2}$	0.45	0.468	0.59	0.821
5-terminal	$L_{s1}$ (nH)	—	0.315	—	0.317
	$L_{s1s2}$ (nH)	—	2.483	—	1.767
	$k_{p,s1}$	—	0.219	—	0.373
	$k_{p,s1s2}$	—	0.466	—	0.801
4-terminal	$L_s$ (nH)	3.5	3.314	2.65	2.327
	$k_{p,s}$	0.47	0.474	0.63	0.84

over sections with straight lines in the theoretical calculation. The theoretical calculation is good enough for the initial design of a transformer. Using the design equations above can greatly cut down on the number of iterations required to design a multi-tap transformer regardless of winding style (i.e., concentric, interleaved , etc.).

Quality factor is an important characteristic of inductors and inductor-like devices. The quality factor of the primary, the secondary, and each section of the secondary is examined separately using the single-port configuration shown in Fig. 3.5(a). The single-port quality factor is defined as:

$$Q = \frac{\text{Im}(Z_{11})}{\text{Re}(Z_{11})}. \quad (3-13)$$

The extracted quality factors for the concentric and interleaved multi-tap transformers are shown in Fig. 3.6(a) and (b), respectively. The maximum quality factor for each transformer is in the range of 10~15 and is achieved in the frequency range of 2 GHz ~ 5 GHz. Both the maximum quality factor and frequency range are comparable with typical values achieved for conventional on-chip inductors and transformers.

The self- and mutual- inductances of the 3:3 multi-tap concentric transformer, that are extracted from simulation, are compared with the developed model in Fig. 3.7, which demonstrates that the broadband model is accurate in the simulated frequency range of DC to 10 GHz. Thus, it can be used in designs targeting most of the current popular wireless applications.

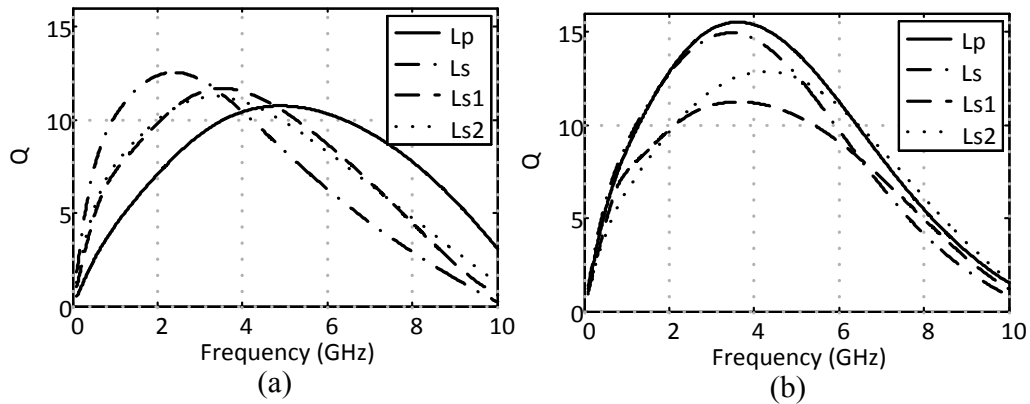


Figure 3.6. Quality factor of primary, secondary and its sub-sections of the designed multi-tap transformer (a) concentric (b) interleaved

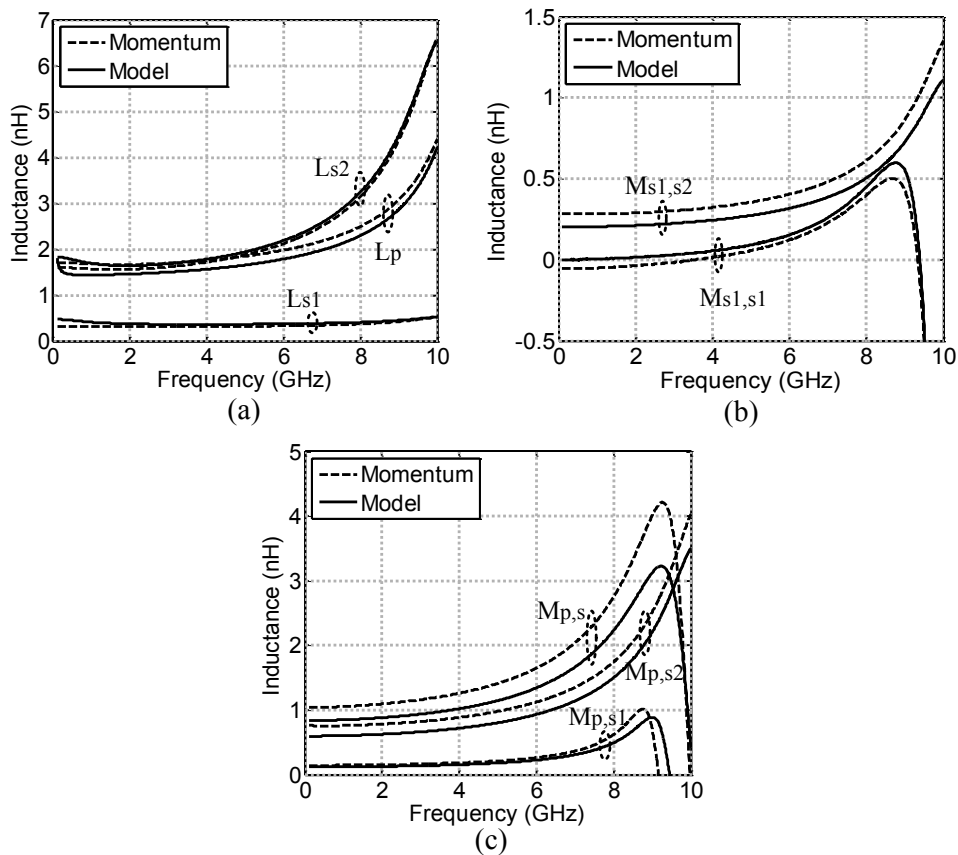


Figure 3.7. Simulation results of Momentum and the lumped-element model versus frequency for (a) self-inductance of the primary and each section of the secondary (b) mutual inductance between the primary and each section of secondary (c) mutual inductance between each section of the secondary.

### 3.3 Characterization of a Switched Multi-Tap Transformer

Recently, switched inductors and transformers were adopted in the LC tank of a VCO to extend its tuning range [13, 19, 47], in the switched output load of a wideband LNA to extend the number of covered bands [38], and in the switched input matching network of a multi-mode LNA to cover a wide frequency range and support single-band, concurrent dual band and wideband operation [32, 48]. The switched asymmetric multi-tap transformer in [32, 48] achieves various inductances with a flexible control of the termination in the secondary with several switches, resulting different secondary inductance and coupling confidence between the primary and the secondary winding. The non-ideality of the switches, such as the switch loss, parasitic capacitance, etc., directly affects the property of the switched multi-tap transformer.

#### 3.3.1 Analysis of the switch loss in a switched multi-tap transformer

The schematic of a switched multi-tap transformer, including a 5-port multi-tap transformer, three switches, a capacitor ( $C_2$ ), and a resistor, is shown in Fig. 3.8. The multi-tap transformer consists of a primary inductor,  $L_1$ , and a secondary inductor,  $L_2$ , that is divided into two sections,  $L_{2a}$ , and  $L_{2b}$ . the coupling coefficient between the primary and each section of the secondary is denoted as  $k_{2a}$ , and  $k_{2b}$ , respectively. The secondary is segmented such that  $L_{2a} < L_{2b}$  and  $k_{2a} < k_{2b}$ . The transistors,  $M_1$ ,  $M_2$ , and  $M_3$ , controlled by the voltage,  $V_{M1}$ ,  $V_{M2}$ , and  $V_{M3}$ , respectively, are the switches that configure the multi-tap transformer into a tunable inductor. When all transistors are turned off, it appears as the primary inductor. When the switches are turned on, either part of the secondary turn is shorted or part of the secondary is terminated with a capacitor. To investigate the effect of the resistances of the

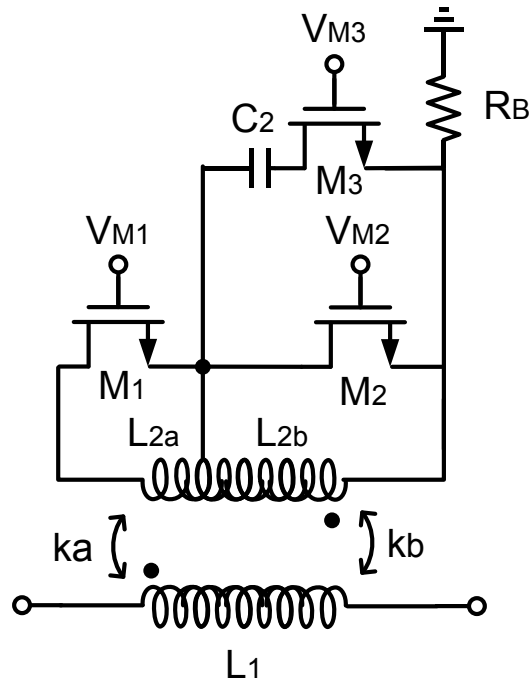


Figure 3.8. Schematic of a switched multi-tap transformer.

switches, the analysis method of a conventional transformer [19, 33, 34] is extended to the asymmetric multi-tap transformer. By assuming the rest of the switches are completely turned off when a switch is turned on, the analysis can be simplified to two categories: short terminated and capacitive terminated transformer, as shown in Fig. 3.9, where the transformer is modeled with two coupled inductors,  $L_1$  and  $L_2$ , with series resistance of  $R_1$  and  $R_2$ . The coupling coefficient is  $k$ .  $R_{SW}$  is the resistance of the switch. The parasitic capacitance thus the effect of the self-resonant frequency is neglected to simplify the analysis.

By analyzing the simplified model in Fig. 3.9, the equivalent impedance of the transformer network is derived as

$$Z_L = R_1(1 + \alpha Q_1 k^2) + j\omega L_1(1 - \beta k^2) \quad (3-14)$$

where  $R_1$ ,  $Q_1$ , and  $L_1$  is the parasitic resistance, the quality factor, and inductance of the primary winding, respectively,  $k$  is the coupling coefficient of the transformer,  $\alpha$  and  $\beta$  are the reflected coefficient determined the secondary winding. When the secondary is directly terminated with a switch, as in Fig. 3.9(a),  $\alpha$  and  $\beta$  are defined as:

$$\alpha = \frac{Q_2 \left(1 + \frac{R_{SW}}{R_2}\right)}{Q_2^2 + \left(1 + \frac{R_{SW}}{R_2}\right)^2} \quad (3-15)$$

$$\beta = \frac{Q_2^2}{Q_2^2 + \left(1 + \frac{R_{SW}}{R_2}\right)^2} \quad (3-16)$$

where  $R_2$  and  $Q_2$  is the parasitic resistance and the quality facto of the secondary winding. From (3-14)-(3-16), it is seen that the inductance and series resistance of the resistive-terminated multi-tap transformer varies as the resistance of the switch changes. When the switch is completely turned-off, the inductance is approximately maximized to  $R_1$  and the series resistance is minimized to  $L_1$ . As the switch is gradually turned-on, the resistance of the switch becomes smaller and the inductance is reduced correspondingly, while the series

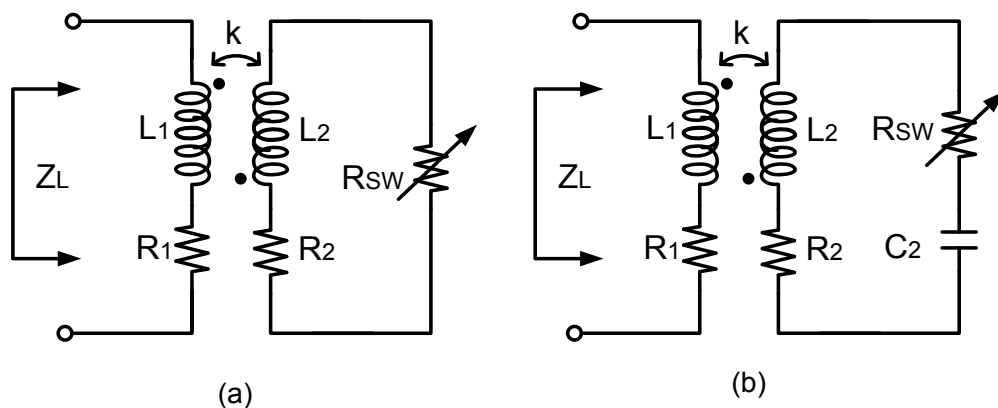


Figure 3.9. Simplified model for the analysis of the multi-tap transformer where the secondary is terminated using either (a) a short-circuit or (b) a capacitor.

resistance first increases and is maximized when  $R_{SW} = R_2(Q_2 - 1)$ , as the switch resistance becomes smaller further, the series resistance reduces. When the switch is completely turned-on with zero ON-resistance, the inductance is approximately minimized to  $L_1(1 - \frac{Q_2^2}{Q_2^2+1}k^2)$  and the series resistance is reduced to  $R_1(1 + \frac{Q_2^2}{Q_2^2+1}Q_1k^2)$ . A high coupling coefficient results in large tuning range, but induced large series resistance thus degrade the quality factor of the switched multi-tap transformer.

When the secondary is terminated by a capacitor with a switch, as in Fig. 3.9 (b),  $\alpha$  and  $\beta$  are defined as:

$$\alpha = \frac{Q_2 \left(1 + \frac{R_{SW}}{R_2}\right) \left(\frac{\omega}{\omega_2}\right)^2}{Q_2^2 \left(\left(\frac{\omega}{\omega_2}\right)^2 - 1\right)^2 + \left(1 + \frac{R_{SW}}{R_2}\right)^2} \quad (3-17)$$

$$\beta = \frac{Q_2^2 \left(\left(\frac{\omega}{\omega_2}\right)^2 - 1\right) \left(\frac{\omega}{\omega_2}\right)^2}{Q_2^2 \left(\left(\frac{\omega}{\omega_2}\right)^2 - 1\right)^2 + \left(1 + \frac{R_{SW}}{R_2}\right)^2} \quad (3-18)$$

where  $\omega_2 = \frac{1}{\sqrt{L_2 C_2}}$  is the resonant frequency of the secondary. From (3-14), (3-17) and (3-18), it is seen that the inductance and series resistance of the capacitive-terminated multi-tap transformer strongly depend on the operation frequency besides the resistance of the switch. The inductance is approximately maximized to  $L_1$  and the series resistance is minimized to  $R_1$  when the switch is completely turned-off. As  $R_{SW}$  reduces while  $R_{SW} > R_2 \left(Q_2 \frac{2-k^2}{2\sqrt{1-k^2}} - 1\right)$ , the switched transformer appears as an inductor across the frequency. When  $R_{SW} < R_2 \left(Q_2 \frac{2-k^2}{2\sqrt{1-k^2}} - 1\right)$ , the capacitive-terminated multi-tap transformer first appears as an inductor when  $\omega < \omega_L$  and  $\omega > \omega_H$ , and appears as a capacitor when  $\omega_L < \omega < \omega_H$ , where

$$\omega_{L,H} = \frac{2-k^2 \pm \sqrt{(2-k^2)^2 - 4 \frac{1}{Q_2^2} \left(1 + \frac{R_{SW}}{R_2}\right)^2 (1-k^2)}}{2(1-k^2)} \omega_2.$$
 As  $R_{SW}$  becomes even smaller,  $\omega_L$  and  $\omega_H$  spreads larger. It is interesting to notice that the equivalent inductance is  $L_1$  regardless of the value of  $R_{SW}$ , while the inductance changes rapidly with frequency in the frequency range close to  $\omega_2$ , which should be avoided, due to the resonance of the secondary. For a given frequency that is not close to  $\omega_2$ , the series resistance of the capacitive-terminated transformer is minimized when the switch is completely turned-off, is increased as the switch resistance decreases and is maximized when  $R_{SW} = R_2 \left( Q_2 \left( \left( \frac{\omega}{\omega_2} \right)^2 - 1 \right) - 1 \right)$ , and is reduced as the switch resistance decrease further. When the switch is completely turned-on with zero ON-resistance, the series resistance and the inductance is reduced to  $R_1$  and  $L_1$ , respectively, when  $\omega \ll \omega_2$ , while the series resistance and the inductance is reduced to  $R_1$  and  $L_1(1 - k^2)$ , respectively, when  $\omega \gg \omega_2$ .

### 3.3.2 Experimental results

To verify the analysis, a switched multi-tap transformer was designed and fabricated in 0.13  $\mu\text{m}$  CMOS. The die photo is shown in Fig. 3.10. The two-port S-parameters of the switched multi-tap transformer were measured through wafer-probing.

#### 3.3.2.1 Switched multi-tap transformer

The 5-port multi-tap transformer was designed in top-most metal with an outer diameter of 300  $\mu\text{m}$ , a metal width of 4.3  $\mu\text{m}$ , and a metal-to-metal spacing of 5  $\mu\text{m}$ . To enable both frequency and time domain simulation, a broadband lumped element model, consisting of three  $\pi$ -networks, was developed similarly as in [37]. The two-port S-

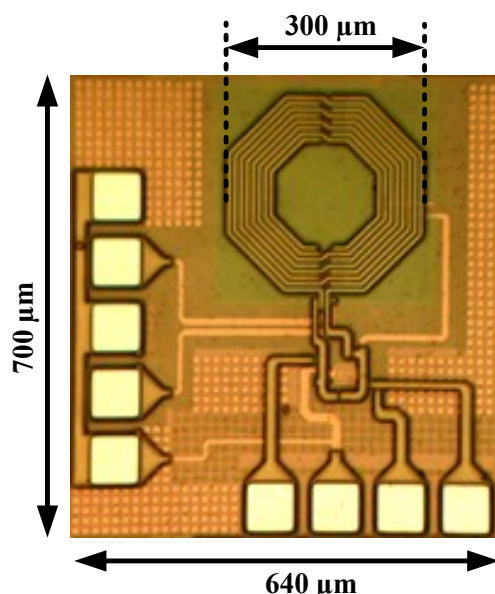


Figure 3.10. Die photo of the switched multi-tap transformer.

parameters of the switched multi-tap transformer were simulated and measured with different control voltages. Its equivalent impedance is extracted with the corresponding Z-parameter as:

$$Z_L = Z_{11} + Z_{22} - Z_{12} - Z_{21} \quad (3-19)$$

The equivalent inductance and quality factor were calculated as

$$L = \frac{\text{imag}(Z_L)}{\omega} \quad (3-20)$$

$$Q = \frac{\text{imag}(Z_L)}{\text{real}(Z_L)} \quad (3-21)$$

The extracted inductance and Q of the switched multi-tap transformer with two-port S-parameter obtained from post-layout simulation and the measurement are shown in Fig. 3.11. It is seen that the measured results reasonably match the post-layout simulation results, but the curves of measured results are slightly shifted to lower frequencies comparing to the simulated ones, which are partially due to the lowered self-resonant frequency because of the parasitic inductance and capacitance of the connection metals, resulting in higher inductance.

The measured  $Q$  is significantly lower than the simulated one when the  $Q$  is relative high since it is more sensitive to the added contact resistance during the measurement. When all switches are tuned off, the switched multi-tap transformer exhibits a simulated and measured peak quality factor of 11.6 and 6.3, respectively, at around 2.5 GHz. The corresponding equivalent inductance of 7.5 nH and 8 nH, respectively. As the switch is turned on, both the inductance and  $Q$  are reduced, but  $Q$  is reduced more dramatically that is partially due the reduced inductance and increased series resistance due to reflected resistance from the secondary. When only  $M_1$  is turned-on with  $V_{M1}=1.2$  V, the simulated and measured inductance was reduced to 4.1 nH and 6.1 nH, and  $Q$  was degraded to 2.7 and 2.9 at 2.5 GHz. When  $M_2$  is tuned on, both inductance and  $Q$  are reduced further to 2.4 nH and 3.2 nH, 1.9 and 2, respectively, at 2.5 GHz because of a larger effective coupling coefficient between the primary and the secondary. When  $M_3$  is turned on, the capacitor  $C_2$  is connected to the circuit and the network appears as an inductor at frequency below 2.5 GHz and above 5 GHz while

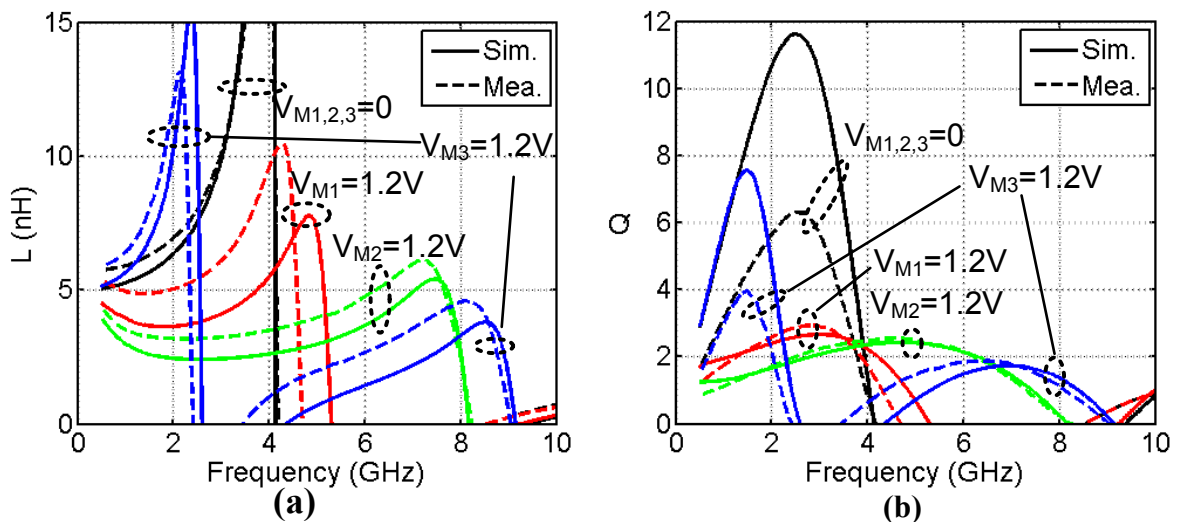


Figure 3.11. (a) Equivalent inductance and (b) quality factor of the switched multi-tap transformer (solid line: post-layout simulation, dashed line: measured).

below the self-resonant frequency of 9 GHz. The simulated and measured peak quality factor is 7.6 and 4, respectively, at 1.5 GHz in the low band, 1.7 and 1.9, respectively at 6.5 GHz in the high band. The corresponding inductance is 6.9 nH and 8 nH, respectively, at 1.5 GHz in the low band, 1.8 nH and 3.1 nH, respectively, at 6.5 GHz in the high band.

It is interesting to notice that the self-resonant frequency increases from 4.2 GHz to 9 GHz as the equivalent inductance is reduced. It is also observed that the self-resonance of the switched multi-tap transformer is closely predicted in the post-layout simulation, implying that the effect of parasitic capacitance of the switches can be captured in the simulation.

### 3.3.2.2 Tunable LC resonators using a switched multi-tap transformer

This type of tunable inductor will most likely be used as the tunable element in an LC-resonator. It is therefore important to evaluate the effect of the switch resistance in this case. In this Section, a series resonator is constructed by connecting the multi-tap transformer in series with an ideal 1 pF capacitor,  $C_1$ , as shown in Fig. 3.12. The quality factor of the resonator is defined as:

$$Q = \frac{f_o}{\Delta f} \quad (3-22)$$

where  $f_o$  is the resonant frequency and  $\Delta f$  is the bandwidth.

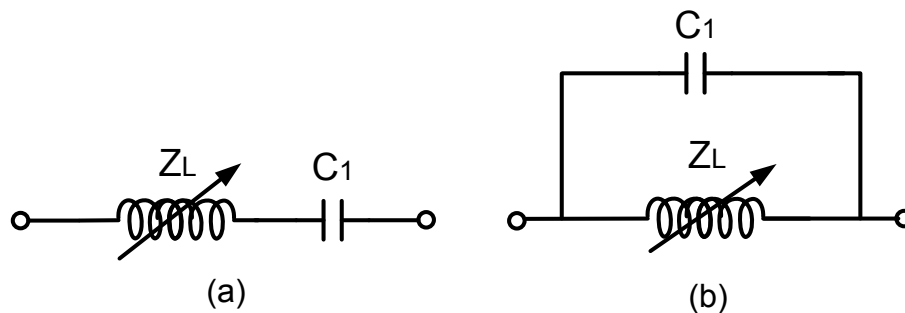


Figure 3.12. (a) Series and (b) parallel resonator with the switched multi-tap transformer as a tunable inductor ( $Z_L$ ).

The resonant frequency and quality factor of the resonators are simulated with the post-layout schematic and the measured two-port S-parameters of the switched multi-tap transformer under different gate control voltages varying from 0 to 1.2 V, which emulates by different level of switch resistance. When the control voltage increases, the switch resistance decreases. The plots of the resonant frequency and the quality factor of the series resonator when  $V_{M1}$  and  $V_{M2}$  vary from 0 to 1.2 V, respectively, are shown in Fig. 3.13 (a) and (b). As  $V_{M1}$  increases from 0 to 1.2 V, the resonant frequency is increased from 1.92 to 2.22 GHz due to the reduced inductance, while the Q of the resonator is reduced from 6.65 to 3.05 due to the reduced Q of the switched transformer, which dominates the quality factor of resonator. As  $V_{M2}$  increases to 1.2 V, the resonant frequency is increased to 2.81 GHz due to the more reduced inductance because of a higher coupling coefficient, while the Q of the resonator is reduced to 2.12 due to the further reduced Q of the switched transformer because of a higher coupling coefficient as well. In both cases, it is seen that the resonance frequency gradually increases as the control voltage increases, while the quality factor first decreases,

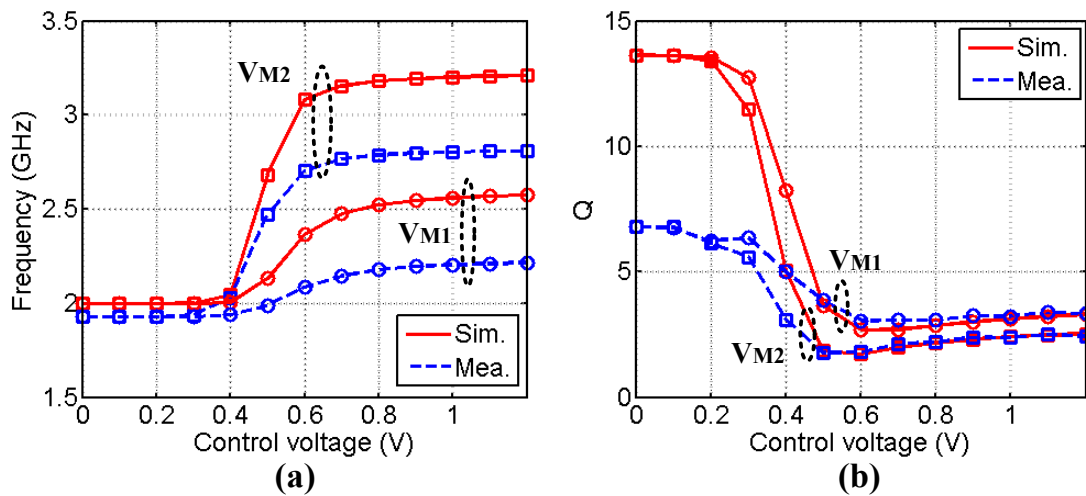


Figure 3.13. (a) Resonant frequency and (b) quality factor of the series resonator with variable control voltage of  $V_{M1}$  and  $V_{M2}$  when  $C_1 = 1$  pF.

reaches minimum at control voltage of around 0.5 ~ 0.6 V, and then increases. It is implied that the resonator may be continuously tuned by the control voltage. However, a high off-resistance and a low on-resistance of the switches are desirable to achieve the best quality factor of a tunable resonator. The switches should operate either in completely on or off state.

Fig. 3.14 shows the resonant frequencies and quality factors of the series resonator when  $V_{M2}$  increases from 0 to 1.2V. As the control voltage is smaller than 0.4 V, only single resonance occurs, and both the resonant frequency and quality factor decreases. As the control voltage increases above 0.4 V, dual resonance occurs. The resonant frequencies in both low band and high band decrease, while the quality factors in both bands increase. When  $V_{M3}$  reaches 1.2 V, it achieves resonance at frequencies of 1.68 GHz and 4.31 GHz concurrently with quality factor of 6.6 and 2.88, respectively.

In Fig. 3.13 and Fig. 3.14, it is seen that the resonant frequency of the resonator with measured S-parameters is lower than that with the post-layout schematic, which are due to the higher equivalent inductance as seen in Fig. 3.11. The quality factors of the resonator are

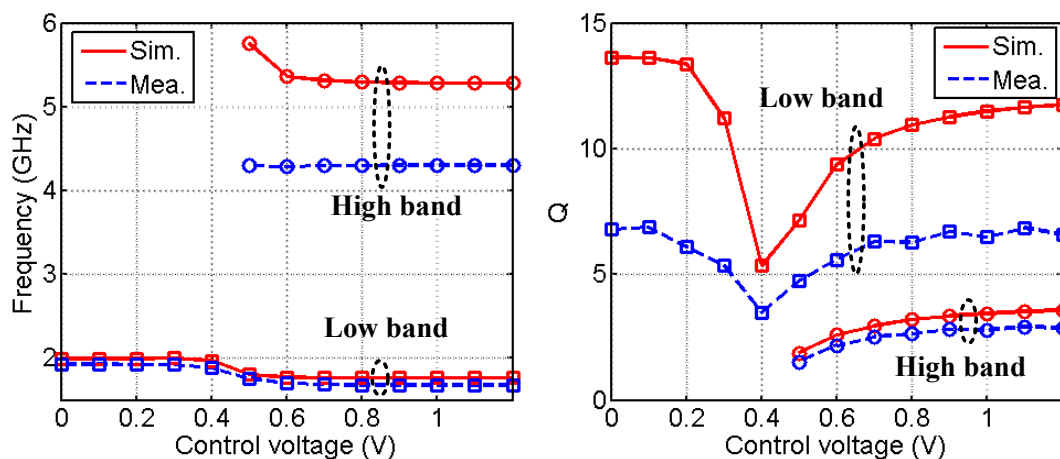


Figure 3.14. (a) Resonant frequency (b) quality factor of the series resonator with variable control voltage of  $V_{M3}$  when  $C_1=1$  pF.

slightly higher than that of the switched multi-tap transformer at corresponding control voltage and frequencies.

Due to the page limit, the plots of the resonant frequency and quality factor of the parallel resonator, which are similar to that of the series resonator but with slightly shifted frequency, are not shown. However, it needs to be mentioned that dual resonance did not occur in the parallel resonator with  $C_1 = 1\text{pF}$  due to the low intrinsic resonant frequencies in both the primary and secondary. When the  $C_1$  is reduced, dual resonance can be observed.

The performance of the series and parallel resonators with the switched multi-tap transformer connected with a 1 pF capacitor is also shown in Table 3.3 when the gate control voltage is either 0 or 1.2 V.

It might be argued that the application of the switched multi-tap transformer is very limited due to the significantly degraded quality factor when the switches are turned on. However, it needs to be noticed that a switched multi-tap transformer with a large  $k$  was characterized for the purpose of wide frequency tuning in this Section. When the quality factor is a key concern, a switched multi-tap transformer with a small  $k$  is preferred at the

Table 3.3. Performance of the series and parallel LC resonator with a switched multi-tap transformer

Control Voltage (V)			Freq. (GHz)		Q	
$V_{M1}$	$V_{M2}$	$V_{M3}$	Ser.	Par.	Ser.	Par.
0	0	0	1.92	1.9	6.8	6.65
1.2	0	0	2.22	2.09	3.33	3.05
0	1.2	0	2.81	2.52	2.44	2.12
0	0	1.2	1.68/4.31	1.64/-	6.6/2.88	6.5/-

cost of smaller tuning range of the inductance. But, the degraded quality factor might not cause significant drawback as it seems. It is observed that the LNA with the switched multi-tap transformer achieved excellent input matching with comparable gain, noise figure, linearity etc. [32]. Also, the inductive tuning would be desirable at higher operation frequencies when the quality factor of a resonator is limited by the capacitor [19]. It is also worth to mention that the self-resonant frequency of the switched multi-tap transformer is extended to a higher frequency when the switch is turned on, which enables the multi-tap transformer to be applicable in a higher frequency range than its intrinsic self-resonant frequency.

### 3.4 Summary

Multi-tap transformers are investigated in detail for the first time. A method for speeding up the design cycle of multi-tap transformers is presented. Symmetric multi-tap concentric and interleaved transformers are designed in 0.13 $\mu\text{m}$  CMOS RF process and characterized up to 10 GHz. The comparison to Momentum simulation results demonstrates the accuracy of the proposed design method as well as the broadband lumped-element model. The feasibility for reconfigurable applications is demonstrated by examining the inductances and coupling coefficients for three different configurations.

The effect of switch loss in a switched asymmetric multi-tap transformer using as a tunable inductor in series and parallel LC resonator, is investigated. The resonant frequency and quality factor of the LC resonators are evaluated under different control voltages of the switches, which emulate the different levels of switch resistance. A switched multi-tap transformer was fabricated in 0.13  $\mu\text{m}$  CMOS, and its equivalent inductance and quality

factor are extracted from the measured S-parameters, which are also used in the evaluation of the LC resonators. It exhibits good flexibility for frequency tuning and shows good potential in RFIC design though the quality factor is reduced when the switch is turned on.

## CHAPTER 4. RECONFIGURABLE MULTIMODE LOW-NOISE AMPLIFIER USING A MULTITAP TRANSFORMER

In a multi-standard multi-band RF system, the low noise amplifier is a key building block that requires input matching across different frequency bands. The limited bandwidth in the matching network of the LNA is a primary bottleneck in realizing such a system. As discussed in Chapter 1, several techniques, such as wideband [1, 3-5], switched multi-band [10, 38], concurrent dual-band [9], tunable narrow band [8], etc., have been proposed for the multi-standard multi-band radio receiver. However, there are severe trade-offs between the number of supported frequency bands and the out-of-band interferer rejection.

To this end, inductors and transformers have been used at the gate of traditional common-source LNAs to provide single-band [49, 50], concurrent dual-band [10], and wideband input matching [26]. A conceptual reconfigurable multi-mode matching network, utilizing a multi-tap transformer and switched capacitors, that supports all three types of input matching, has been proposed in [41], that potentially relaxes the design trade-off between frequency coverage and linearity requirement through adaptive operation.

In this chapter, a reconfigurable multi-mode LNA capable single-band, concurrent dual-band, or wideband operation will be discussed [32, 48]. A detailed analysis and design strategy for implementing a transformer-based multi-mode LNA will be first provided in Section 4.1. Then, the Circuit design details will be shown in Section 4.2 and the experimental results of a prototype multi-mode LNA will be presented in Section 4.3. Finally, Section 4.4 will conclude and summarize this chapter.

## 4.1 Reconfigurable Multimode LNA

In the conventional narrow band LNA, shown in Fig. 4.1(a), a series gate inductor,  $L_1$ , is used for narrow band matching and the input impedance is:

$$Z_{IN}(\omega) = \frac{g_m L_s}{C_{gs}} + j \left\{ \omega L_1 + \omega L_s - \frac{1}{\omega C_{gs}} \right\} \quad (4-1)$$

where  $g_m$  is the transconductance of transistor  $M_1$ . From (1), the operating frequency is given as:

$$f = \frac{1}{2\pi\sqrt{(L_1+L_s)C_{gs}}} \quad (4-2)$$

By controlling the value of  $L_1$ ,  $L_s$ , or  $C_{gs}$ , the operating frequency of the traditional LNA could be dynamically controlled making it suitable for use in applications such as SDR. Changing  $L_s$  or  $C_{gs}$ , however, will also affect the real part of the input impedance, which will have unwanted effects on the input matching and power transfer. Therefore, the only real option for tuning the operating frequency is to control the value of  $L_1$ .

The value of  $L_1$  can be controlled in a number of ways. One popular way to realize a tunable inductor is through the use of active inductors [8]. Unfortunately, active inductors tend to be quite noisy, and placing them at the input of the LNA will result in an increased noise figure. Another option is to use a bank of inductors or multi-tap inductors and then selectively switch them into/out of the signal path. Due to the increase in the noise figure, this approach is unsuitable for use at the input and instead is reserved for use in the load network [38, 51]. A transformer can also be used to realize a tunable inductor. This approach maintains small area and as will be seen, avoids the placement of noisy switches directly in the signal path.

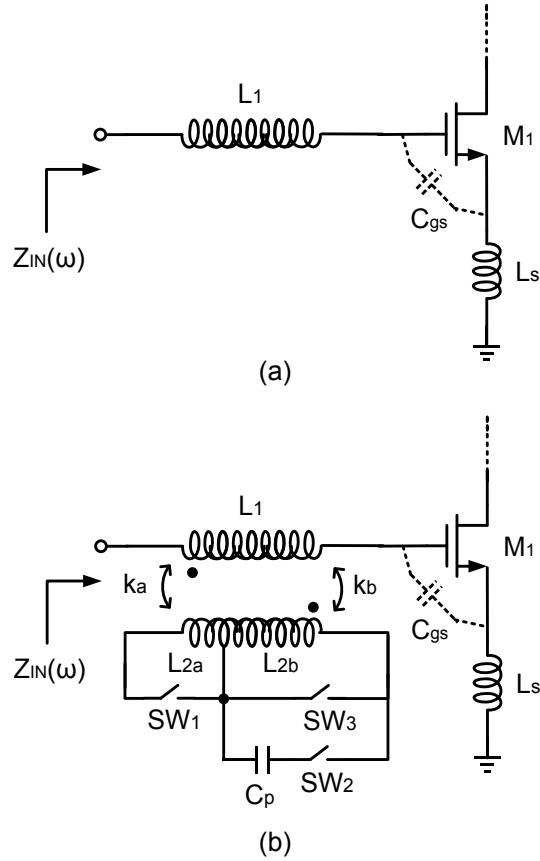


Figure 4.1. Input of (a) a conventional inductively degenerated LNA (b) the proposed multi-mode LNA with a reconfigurable multi-tap transformer as the gate inductor.

#### 4.1.1 Multimode input matching network

A transformer with primary winding,  $L_1$ , secondary winding,  $L_2$ , and coupling coefficient,  $k$ , can be used as an inductor by considering it as a one-port network with terminals  $A$  and  $B$ , as shown in Fig. 4.2(a). When the transformer is considered in this way, the effective inductance appearing between terminals  $A$  and  $B$  is calculated as:

$$L_{AB} = L_1 - \Delta \quad (4-3)$$

where  $\Delta$  is the reflected inductance from the secondary winding,  $L_2$ , and depends on how this winding is terminated. Fig. 4.2 illustrates three basic terminations of the secondary

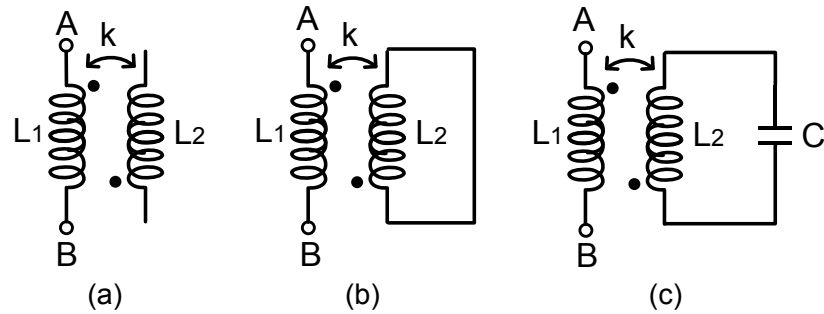


Figure 4.2. Transformer operating as inductor with secondary winding terminated with (a) an open, (b) a short, and (c) a capacitive load

winding: open, shorted, and capacitively terminated. For the networks shown in Fig. 4.2(a), (b), and (c), the  $\Delta$  term in (3) is given as:

$$\Delta = \begin{cases} 0 & \text{(a)} \\ k^2 L_1 & \text{(b)} \\ k^2 L_1 \frac{\omega^2 L_2 C_p}{\omega^2 L_2 C_p - 1} & \text{(c)} \end{cases} \quad (4-4)$$

respectively. Therefore, the inductance,  $L_{AB}$ , of a one-port transformer network can be tuned by controlling the way in which the secondary winding,  $L_2$ , is terminated. Further control of the inductance can be gained by also controlling the coupling coefficient,  $k$ . This can be achieved by using a multi-tap inductor for  $L_2$  where the coupling between  $L_1$  and each section of  $L_2$  are different.

By replacing the inductor,  $L_1$ , in Fig. 4.1(a) with a multi-tap transformer as shown in Fig. 4.1(b), a reconfigurable input matching network can be easily achieved [48]. The transformer consists of a primary inductor,  $L_1$ , and a secondary inductor,  $L_2$  that is divided into two sections,  $L_{2a}$  and  $L_{2b}$ . The coupling coefficient between the primary and each section of the secondary is denoted as  $k_a$  and  $k_b$ , respectively. In general,  $k_a \neq k_b$ , implying that the

multi-tap inductor does not use a symmetric center tap. The parasitic capacitance and resistance of the transformer are neglected in order to simplify the following analysis.

With the asymmetrically segmented secondary inductor and three switches, ideally nine different values of  $L_{AB}$  may be achieved when each segment of the secondary is open, shorted and terminated with a capacitor. In practice, some of these switch combinations result in significant overlap in values and effectively only five modes of operation are used: three single-band modes (modes 1, 2, and 4), one concurrent dual-band mode (mode 3), and one ultra-wideband mode (mode 5). Table 4.1 shows the switch configuration for each mode of operation.

As previously mentioned, (4-3) and (4-4) illustrate that there are two ways in which the inductance can be varied: by changing the impedance of the secondary termination, or by changing the coupling coefficient. The coupling coefficient of a multi-tap transformer can be easily changed by simply selectively short-circuiting different taps.

By changing the coupling coefficient only, the single-band response can be tuned to different operating frequencies. This is indicated in Table 4.1 as mode 1, 2, 4, and 5. The generalized input impedance for these four modes can be written as:

$$Z_{IN}(\omega) = \frac{g_m L_s}{c_{gs}} + j \left\{ \omega L_1 (1 - k_i^2) + \omega L_s - \frac{1}{\omega c_{gs}} \right\} \quad (4-5)$$

where  $i = 0, a, b,$  and  $c$  for mode 1, 2, 4, and 5 respectively. The coupling coefficient  $k_0$  represents the coupling between the primary winding and open-circuited secondary winding and is defined to be  $k_0 = 0$ . Recall that  $k_a$  and  $k_b$  are the coupling coefficients between the primary winding,  $L_1$ , and each section of the multi-tapped secondary,  $L_{2a}$  and  $L_{2b}$ ,

Table 4.1. Switch configuration for different modes of operation

Mode	SW <sub>1</sub>	SW <sub>2</sub>	SW <sub>3</sub>	Note
1	0	0	0	Single band
2	1	0	0	Single band
3	0	1	0	Concurrent dual-band
4	0	0	1	Single band
5	1	0	1	Ultra-wideband

Note: 1 = CLOSED, 0 = OPEN

respectively. Finally, the coupling coefficient  $k_c = k_a\sqrt{L_{2a}/L_2} + k_b\sqrt{L_{2b}/L_2}$  and represents the total coupling between the primary and secondary windings  $L_1$  and  $L_2$ .

The bandwidth over which the LNA is matched is primarily determined by the effective quality factor,  $Q$ , of the input matching network, which is expressed as:

$$Q = \frac{1}{2\pi f g_m L_s}. \quad (4-6)$$

As the operating frequency is increased,  $Q$  becomes smaller and the bandwidth of the matching network will thereby increase. Finally, a general expression for the operating frequency in these modes can be found by analyzing (4-5):

$$f = \frac{1}{2\pi\sqrt{(L_1(1-k_i^2)+L_s)C_{gs}}}. \quad (4-7)$$

When SW<sub>2</sub> is closed, a section of the secondary winding becomes capacitively terminated and the LNA is put into mode 3. It has been shown in [10] that a capacitively terminated transformer will have two resonant frequencies. This will result in a concurrent dual-mode operation. In this case the input impedance is given by:

$$Z_{IN}(\omega) = \frac{g_m L_s}{C_{gs}} + j \left\{ \omega L_1 \left( 1 - \frac{k_b^2}{1 - \left(\frac{\omega_2}{\omega}\right)^2} \right) + \omega L_s - \frac{1}{\omega C_{gs}} \right\} \quad (4-8)$$

where  $\omega_2 = 1/\sqrt{L_{2b}C_p}$ . By analyzing (4-8), it is seen that the circuit achieves an input match at two frequencies simultaneously. These frequencies are given by:

$$f_L^2 = \frac{f_1^2 + f_2^2 - \sqrt{f_1^4 + f_2^4 + f_1^2 f_2^2 (4k_b^2 - 2)}}{2(1 - k_b^2)} \quad (4-9)$$

$$f_H^2 = \frac{f_1^2 + f_2^2 + \sqrt{f_1^4 + f_2^4 + f_1^2 f_2^2 (4k_b^2 - 2)}}{2(1 - k_b^2)} \quad (4-10)$$

where  $f_1$  and  $f_2$  are the resonant frequency of the primary and secondary path, respectively. The frequency  $f_1$  is the same as that which is given in (4-2), while frequency  $f_2$  is expressed as:

$$f_2 = \frac{1}{2\pi\sqrt{L_{2b}C_p}} \quad (4-11)$$

#### 4.1.2 Design strategy

When designing the multi-mode LNA, the first design consideration is the targeted frequency bands. From the previous analysis, the center frequencies of the five modes can be calculated using (4-2), (4-7), (4-9), and (4-10). The key to achieving the desired bands of operation is to properly size the inductances and coupling coefficients of the multi-tap transformer for a given LNA core. The operating frequency of mode 1 is set by the primary inductance  $L_1$ . Then, by choosing different coupling coefficient  $k_a$  and  $k_b$ , the operating frequency of mode 2 and 4 can be set, respectively. Knowing  $k_b$ , the bands of mode 3 can be further determined by sizing  $C_p$ . A limitation of mode 3, however, is that the lower band will always be lower than mode 1 according to (4-9) and (4-10) and only certain dual-band

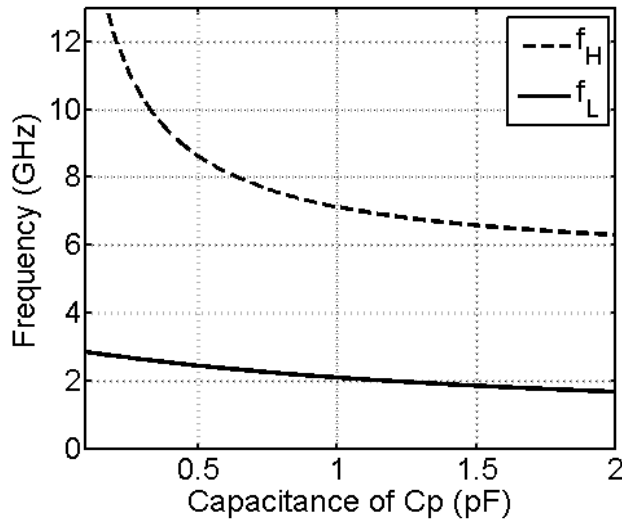


Figure 4.3. Plot of low-band and high-band resonant frequency as a function of capacitance  $C_p$  for  $L_1 = L_2 = 6.8$  nH,  $L_{2a} = 1.7$  nH,  $L_{2b} = 3.4$  nH,  $k_a = 0.63$ , and  $k_b = 0.87$ .

combinations can be realized for a given  $C_p$ , as shown in Fig. 4.3. Ideally, the center frequency of mode 5 can also be chosen by properly determining the total coupling coefficient  $k_c$ , which is normally larger than both  $k_a$  and  $k_b$ , and naturally results in wide-band matching at high frequencies as seen in (4-6). However, in order to simplify the transformer design, often  $L_1 = L_2$  is chosen, which results in  $k_c$  being pre-determined by the choices of  $L_1$ ,  $k_a$  and  $k_b$ , and thus the center frequency of mode 5 will often be set. By allowing  $L_1 \neq L_2$ , mode 5 operation can be independently controlled, but this will also increase the complexity of the transformer design.

The design and optimization techniques for a source degenerated common source amplifier presented in [49, 50] can be directly applied in this multi-mode LNA design to achieve simultaneous noise and input matching. The device sizing of the LNA core, excluding the switched multi-tap transformer network, can be finalized by optimizing the LNA for mode 1. Due to the simultaneous noise and input matching characteristic of the

LNA, it is seen that optimum noise and input matching will be closely achieved for all modes once the LNA is optimized for mode 1, which will be confirmed with simulation results in later part of this section.

The goal of this design was to cover as wide of a frequency range as possible which encompasses as many different standards as possible. To this end, the center frequencies of 2.96 GHz, 3.75 GHz, and 5.56 GHz are targeted for mode 1, 2, and 4, respectively; the frequencies of 2.09 GHz and 7.25 GHz are targeted in mode 3; and 6.99 GHz is the targeted center frequency for mode 5. With the values of  $g_m = 50$  mS,  $C_{gs} = 400$  fF, and  $L_s = 0.4$  nH, initial values for the multi-tap transformer of  $L_1 = L_2 = 6.8$  nH,  $L_{2a} = 1.7$  nH,  $L_{2b} = 3.4$  nH,  $k_a = 0.63$ , and  $k_b = 0.87$  are arrived at. The termination capacitance value of  $C_p = 1$  pF is also used.

### 4.1.3 Noise analysis

Noise is an important consideration in LNA design and careful attention must be paid when adding components to the input of the LNA. The noise model that is used for the following analysis is shown in Fig. 4.4. Resistors  $R_1$ ,  $R_{2a}$ , and  $R_{2b}$  are the parasitic resistance of the transformer windings  $L_1$ ,  $L_{2a}$ , and  $L_{2b}$ , respectively. The parasitic ON resistance, and the corresponding noise contribution, of the switches are modeled as part of resistances  $R_{2a}$  and  $R_{2b}$ . These losses are important to model because they have a significant impact on the overall noise figure of the LNA.

The following noise analysis uses mode 3 operation as an example to derive a general expression for the noise figure that is valid for all five modes. In order to simplify the analysis, only thermal noise and induced gate noise sources are considered. It is verified in

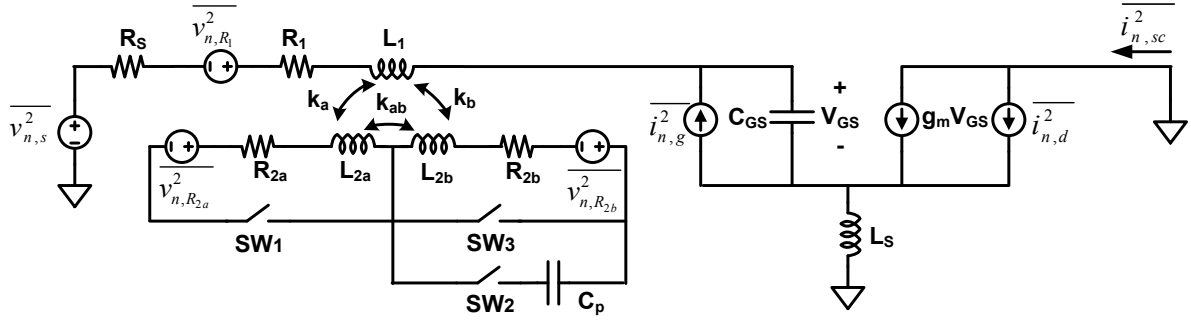


Figure 4.4. Noise model of the multi-mode LNA.

later Sections that this simplification still gives good agreement with simulation results. As seen in Table 4.1, SW<sub>2</sub> is closed for mode 3 while all other switches are open. Using Fig. 4.4, the total short-circuit noise current due to noise contributed by the source can be written as:

$$i_{sc,R_s} = \frac{g_m v_{n,R_s}}{s C_{gs} (R_s + Z'_{IN} - \alpha)} \quad (4-12)$$

where

$$Z'_{IN} = \frac{g_m L_s}{C_{gs}} + s L_s + \frac{1}{s C_{gs}} + R_1 + s L_1, \quad (4-13)$$

$$\alpha = \frac{s^2 M^2}{Z_2} = \frac{k_b^2 s^3 L_1 L_2 b C_p}{s^2 L_2 b C_p + s C_p R_2 b + 1}, \quad (4-14)$$

$M$  is the mutual inductance between the primary and secondary windings which is expressed as  $M = k_b \sqrt{L_1 L_2 b}$ , and  $Z_2$  is the impedance of the secondary tank which is given as  $Z_2 = s L_2 b + \frac{1}{s C_p} + R_2 b$ .

Similarly, an expression for the short circuit noise current due to noise contributed from the lossy transformer is written in two parts. First, the output noise due to the parasitic loss of the primary winding of the transformer is expressed as:

$$i_{sc,R_1} = \frac{g_m v_{n,R_1}}{s C_{gs} (R_s + Z'_{IN} - \alpha)}. \quad (4-15)$$

The contribution of the parasitic loss of the secondary to the output noise current is:

$$i_{sc,R_2} = \frac{\alpha g_m v_{n,R_2b}}{s^2 C_{gs} k_b \sqrt{L_1 L_2 b} (R_S + Z'_{IN} - \alpha)} \quad (4-16)$$

where  $R_{2b}$  is the total effective parasitic resistance of the secondary winding including the ON-resistance of the switch.

The portion of the short-circuit noise current due to induced gate and thermal drain noise of transistor  $M_1$  can be derived as:

$$i_{sc,g} = \frac{g_m (R_S + R_1 + sL_1 - \alpha) i_{n,g}}{s C_{gs} (R_S + Z'_{IN} - \alpha)} \quad (4-17)$$

$$i_{sc,d} = i_{n,d} \left( 1 - \frac{g_m L_s}{C_{gs} (R_S + Z'_{IN} - \alpha)} \right). \quad (4-18)$$

The noise factor of the proposed LNA is expressed as:

$$F = 1 + \frac{\overline{i_{sc,R_1}^2} + \overline{i_{sc,R_2}^2} + \overline{i_{sc,g}^2} + \overline{i_{sc,d}^2}}{\overline{i_{sc,R_S}^2}}. \quad (4-19)$$

Substituting (4-12) and (4-15)-(4-18) into (4-19), the complete noise figure for the proposed LNA operating in mode 3 is given as:

$$F = 1 + \frac{\overline{v_{n,R_1}^2} + \left| \frac{\alpha}{sM} \right|^2 \overline{v_{n,R_2}^2} + |R_S + R_1 + sL_1 - \alpha|^2 \overline{i_{n,g}^2} - \omega^2 \left| \frac{(R_S + Z'_{IN} - \alpha) C_{gs} - g_m L_s}{g_m} \right|^2 \overline{i_{n,d}^2}}{\overline{v_{n,R_S}^2}} \quad (4-20)$$

Equation (4-20) can also be used to calculate the noise factor in other modes by adjusting the expression used for  $\alpha$ , mutual inductance, and the thermal noise contribution from the secondary winding. The mode-dependent expressions for  $\alpha$ ,  $M$ , and  $\overline{V_{n,R_2}^2}/\Delta f$  are summarized in Table 4.2.

Table 4.2. Mode-dependent terms for noise factor calculation

Mode	$\overline{v_{n,R_2}^2}/\Delta f$	$M$	$\alpha$
1	$4kT(R_{2a} + R_{2b})$	$k_a\sqrt{L_1L_{2a}} + k_b\sqrt{L_1L_{2b}}$	0
2	$4kTR_{2a}$	$k_a\sqrt{L_1L_{2a}}$	$\frac{s^2M^2}{sL_{2a} + R_{2a}}$
3	$4kTR_{2b}$	$k_b\sqrt{L_1L_{2b}}$	$\frac{s^3M^2C_p}{s^2L_{2b}C_p + sC_pR_{2b} + 1}$
4	$4kTR_{2b}$	$k_b\sqrt{L_1L_{2b}}$	$\frac{s^2M^2}{sL_{2b} + R_{2b}}$
5	$4kT(R_{2a} + R_{2b})$	$k_a\sqrt{L_1L_{2a}} + k_b\sqrt{L_1L_{2b}}$	$\frac{s^2M^2}{sL_2 + R_{2a} + R_{2b}}$

Note:  $L_2 = L_{2a} + L_{2b} + 2k_{ab}\sqrt{L_{2a}L_{2b}}$

## 4.2 Circuit Details

This Section describes the design and simulation of a multi-mode LNA supporting single-band, concurrent dual-band, and ultra-wideband operations. Fig. 4.5 shows the schematic of the proposed LNA where an output buffer has been added to drive the 50  $\Omega$  test equipment.

The LNA is based on the traditional common-source topology and includes the multi-mode matching network discussed in the previous Section. The input stage is realized by absorbing the gate inductance into the primary winding of a switched multi-tap transformer. The multi-tap secondary winding is terminated in the same way that was demonstrated in Fig. 4.1(b) with the ideal switches replaced by NMOS transistors. The size of the switch transistors  $M_4$ ,  $M_5$ , and  $M_6$ , are maximized so as to minimize the series ON-resistance in

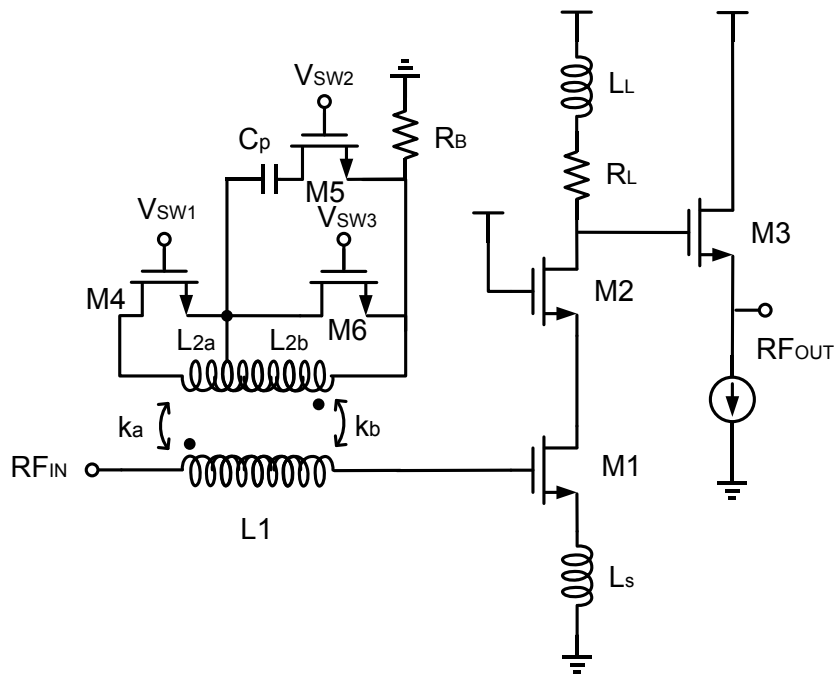


Figure 4.5. Schematic of the proposed multi-mode LNA.

order to achieve high gain and low noise figure. This is balanced, however, with the need to minimize the added parasitic capacitance. Too much parasitic capacitance can cause a significant frequency shift in the different modes and in the extreme case may cause unwanted resonances. A large resistor,  $R_B$ , is added to provide a DC path to ground for the purpose of biasing the switches.

The total response of the LNA is a combination of the input matching network as well as the load network and to avoid unnecessary signal attenuation, the frequency response of the load network should match that of the input network. One option is to use a reconfigurable band-selective load [38], The total response of the LNA is a combination of the input matching network as well as the load network and to avoid unnecessary signal attenuation, the frequency response of the load network should match that of the input network. One option is to use a reconfigurable band-selective load [38], however, for

simplicity a wideband resistive load was used to de- $Q$  the load inductor for bandwidth extension.

#### 4.2.1 Integrated multitap transformer

A key element to the proposed LNA is the design, modeling, and implementation of the fully integrated multi-tap transformer. The transformer structure was obtained through numerical evaluation of many different configurations following the techniques presented in [37, 45]. The final transformer design utilizes an interleaved configuration with an extra tap placed in the secondary winding forming a 5-port network, shown in Fig. 4.6(a). The 8-turn interleaved transformer was designed with an outer diameter of 300  $\mu\text{m}$ , a metal width of 4.3  $\mu\text{m}$ , and a metal-to-metal spacing of 5  $\mu\text{m}$ . The top-most metal was used to achieve a high quality factor and high self-resonant frequency.

In order to simulate the circuit in both the frequency- and time-domain, a broad band lumped element model of the multi-tap transformer, consisting of segments of  $\pi$ -networks was developed using ADS Momentum and is shown in Fig. 4.6(b) [37].

The low frequency behavior is modeled by inductors  $L_1$ ,  $L_{2a}$  and  $L_{2b}$ , and the coupling coefficients,  $k_a$ ,  $k_b$ , and  $k_{ab}$ . The modeled values of  $L_1$ ,  $L_{2a}$ , and  $L_{2b}$  are 5.38 nH, 1.19 nH, and 2.78 nH, respectively. The values for  $k_a$ ,  $k_b$ , and  $k_{ab}$  are 0.62, 0.77, and 0.39, respectively.

The tunable inductance is demonstrated in Fig. 4.6(c) which shows the effective inductance of the multi-tap transformer (i.e.,  $L_{AB}$  from Fig. 4.2) for different modes. The effective inductance is extracted from 1-port S-parameter simulations using the relationship:

$$L_{eff} = \frac{\text{Imag}(Z_{11})}{\omega}. \quad (4-21)$$

The frequency bands of interest for each mode are also shown in Fig. 4.6(c) as bold lines. It is seen that the effective inductance, for a given mode, increases rapidly at higher frequencies. This is due to the interaction of parasitic capacitances and can be controlled through careful design of the transformer. The equivalent quality factor of the multi-tap transformer for each mode is shown in Fig.6 (d). When the switch is turned-on, the quality

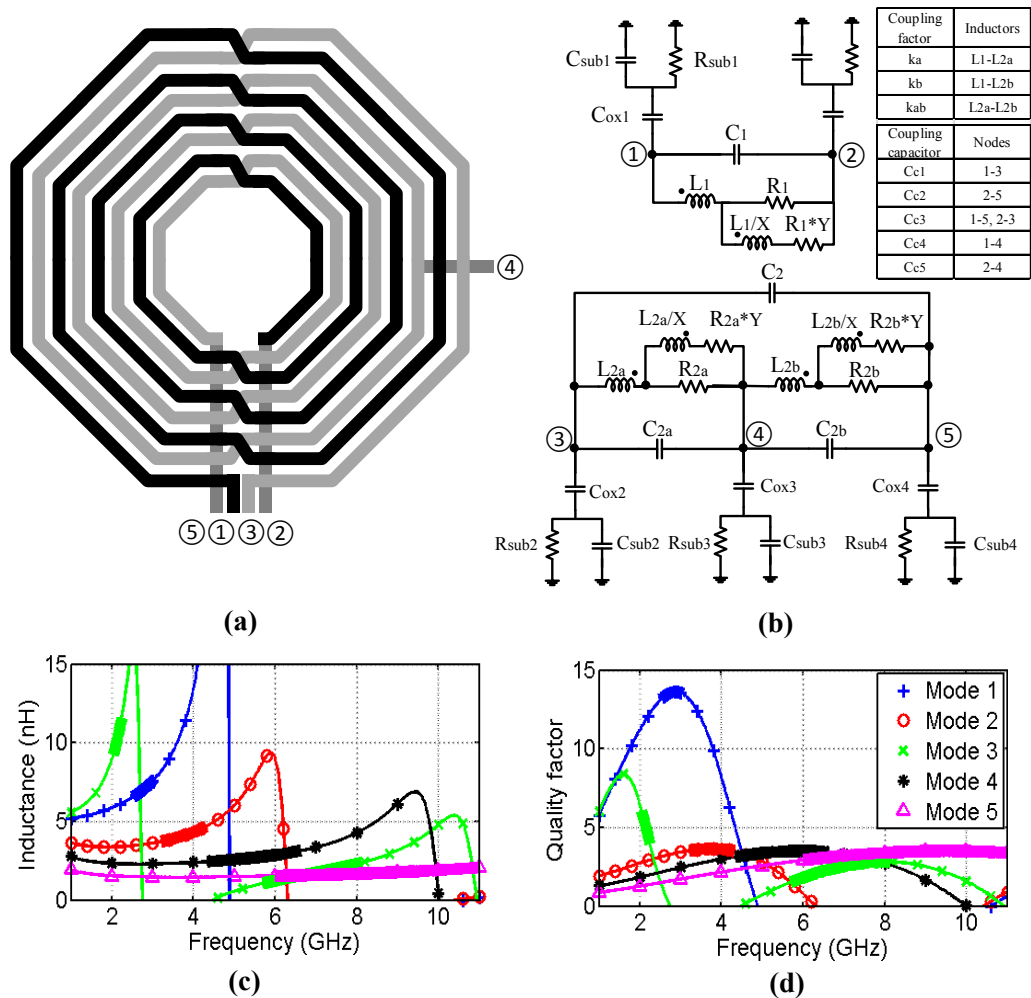


Figure 4.6. (a) Multi-tap transformer layout, (b) broadband lumped-element model of the multi-tap transformer, (c) simulated equivalent inductance, and (d) quality factor of the multi-tap transformer with switches and capacitors (the region of operation are plotted in bold).

factor is reduced due to the switch loss and the increased intrinsic series resistance of the transformer at high frequency.

#### 4.2.2 Simulation results

Circuit operation is verified through simulation. Both simulated as well as calculated  $S_{11}$  is plotted for each mode and is shown in Fig. 4.7. It is seen that, in general, simulations match well with the theory presented in Section 4.1. In mode 1, 2, and 4, the input is configured as a single-band matching network with center frequencies of 2.79 GHz, 3.76 GHz, and 5.49 GHz, respectively. The -10 dB bandwidths for these same modes are 530 MHz, 1.1 GHz, and 2.1 GHz, respectively. The increase in bandwidth with center frequency is clearly seen in Fig. 4.7(a).

In mode 3, the input network is configured to operate as a concurrent dual-band matching network. In this mode, the network operates at both 2.14 GHz and 6.91 GHz. While the simulated and theoretical results match well for the low-frequency band, the simulated -10 dB bandwidth of the high-band is much smaller than the predicted 2.4 GHz. This is due to neglected parasitics in the analysis as well as variations in the desired coupling coefficients; the upper-band of mode 3 depends upon the absolute value of the coupling coefficient [10].

In mode 5, the input network is configured to operate in a wideband mode. The simulated -10 dB bandwidth is underestimated by approximately 30%. This underestimation is again due to the presence of parasitic capacitance. The parasitic capacitance acts like a capacitive termination for the secondary winding and results in a high-order matching network with a wider bandwidth. The theoretical analysis, on the other hand, treats mode 5 as a single inductor with an ideal short-circuit termination of the secondary winding. This is

verified by looking at Fig. 4.7(c), which shows two clear resonant frequencies at 7.4 GHz and 10.2 GHz – a phenomenon only achievable when the secondary winding is capacitively terminated.

The comparisons of Fig. 4.7 clearly show that the analysis of the preceding Section can adequately predict the location of the operating band though larger deviations appear at higher frequencies. Therefore the analysis is a good starting point for numerically evaluating

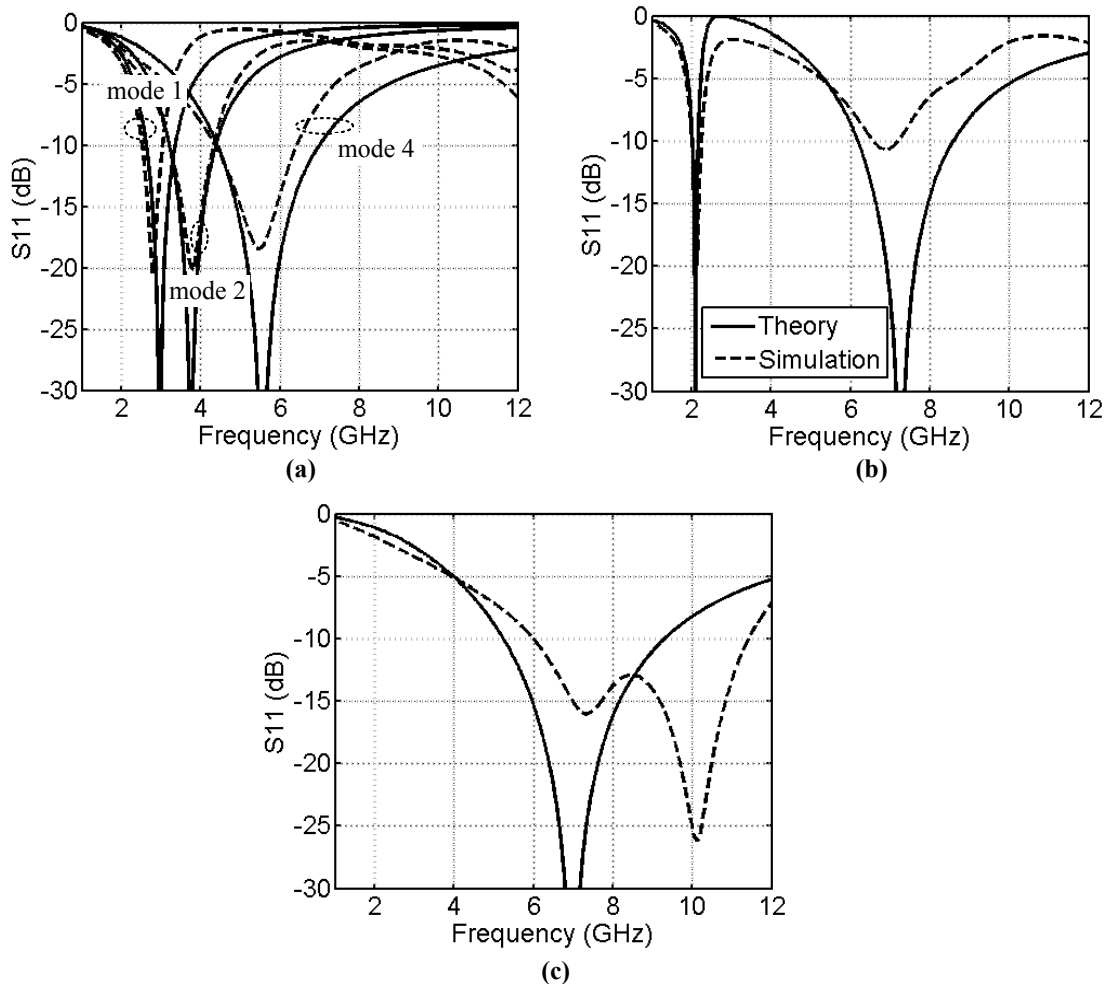


Figure 4.7. Theoretical and simulated  $S_{11}$  for (a) mode 1, 2, and 4, (b) mode 3, and (c) mode 5.

a large number of transformer designs, although simulations are still required for accurate final design.

In Fig. 4.8, the noise analysis is also verified through simulation and compared to the previously presented theoretical analysis. For completeness the simulated and calculated noise figures are shown for a wide range of frequencies, however, shaded boxes identify the desired bands of operation. It is seen that the calculated and simulated noise figures agree quite well in the bands of interest.

In modes 1, 2, and 4, the simulated noise figures at the respective center frequencies are 1.75 dB, 3.18 dB, and 3.67 dB, respectively. In mode 3, the simulated noise figure is 2.76 dB and 5.12 dB for the low and high band, respectively. In mode 5, the simulated noise figure ranges from 3.91–5.98 dB. The increased noise figure at high frequencies is mainly due to the reduction in gain, which may be improved by using transistors with high cut-off frequencies. Due to the simplicity of the input matching network and noise model, the analytical equation could not predict the out-of-band noise figure correctly; however, it is unusual to need such accuracy.

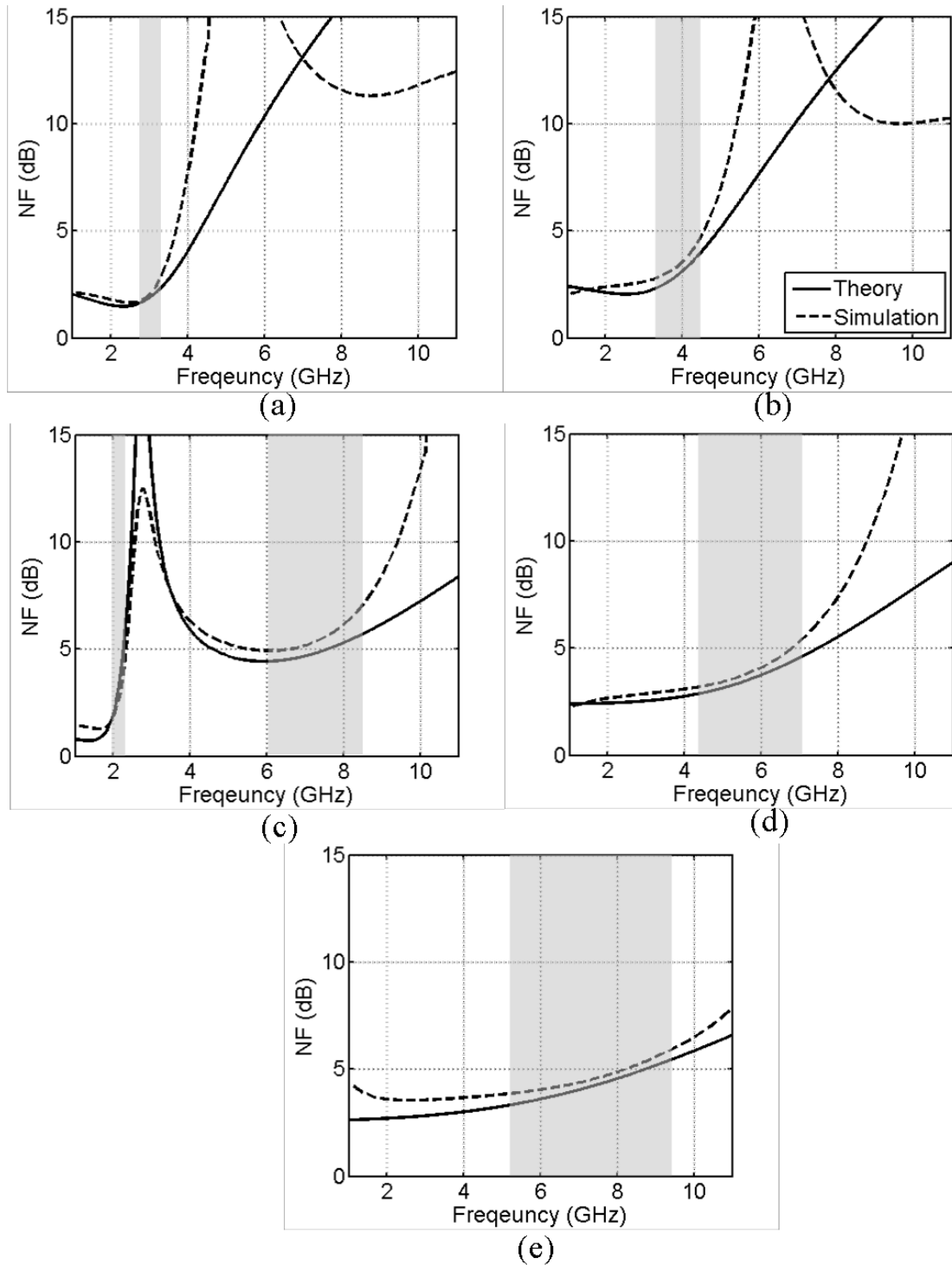


Figure 4.8. Theoretical and simulated noise figure (a) mode 1, (b) mode 2, (c) mode 3, (d) mode 4, and (e) mode 5 (the shaded box denotes the desired band of operation).

### 4.3 Experimental Results

The multi-mode LNA shown in Fig. 4.5 was fabricated in a 0.13  $\mu\text{m}$  CMOS process. The circuit measures 1.04 mm  $\times$  0.7 mm, including pads, and is shown in Fig. 4.9. The LNA was characterized via wafer probing and the effects of the output buffer were de-embedded from the measurement results. The LNA (excluding the buffer) dissipates a total of 6.4 mW from a 1.2 V supply.

The S-parameters were measured using an Agilent E5071C network analyzer. Fig. 4.10 shows the measured  $S_{11}$  and  $S_{21}$  for all modes. The center frequencies of modes 1, 2, and 4 are 2.8 GHz, 3.3 GHz, and 4.6 GHz, respectively. The measured -10 dB bandwidth for these three modes is 700 MHz, 1 GHz, and 2.2 GHz, respectively. The power gain varies between 14.9–16.4 dB, 12.8–14.7 dB, and 14.1–14.8 dB for mode 1, 2, and 4, respectively. In mode 3, the two concurrent bands are centered at 2.05 GHz and 5.65 GHz. The upper-band bandwidth is measured to be 3.1 GHz and the gain ranges between 12–15 dB. Due to an

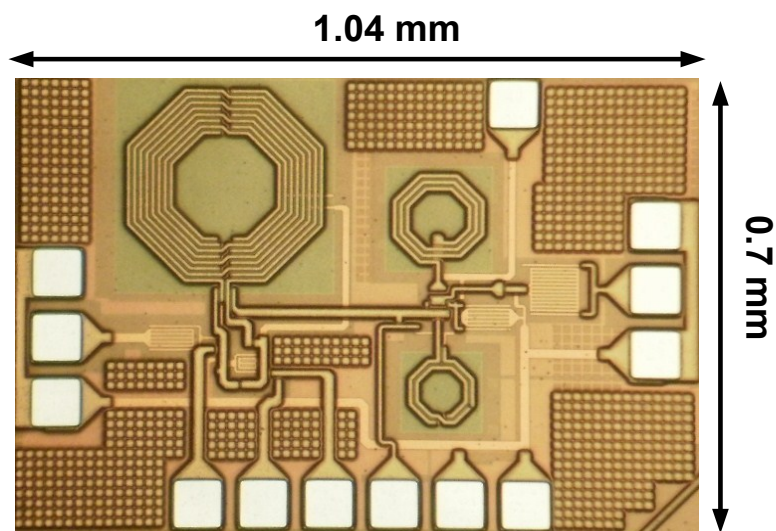


Figure 4.9. Microphotograph of the LNA employing a multi-tap transformer.

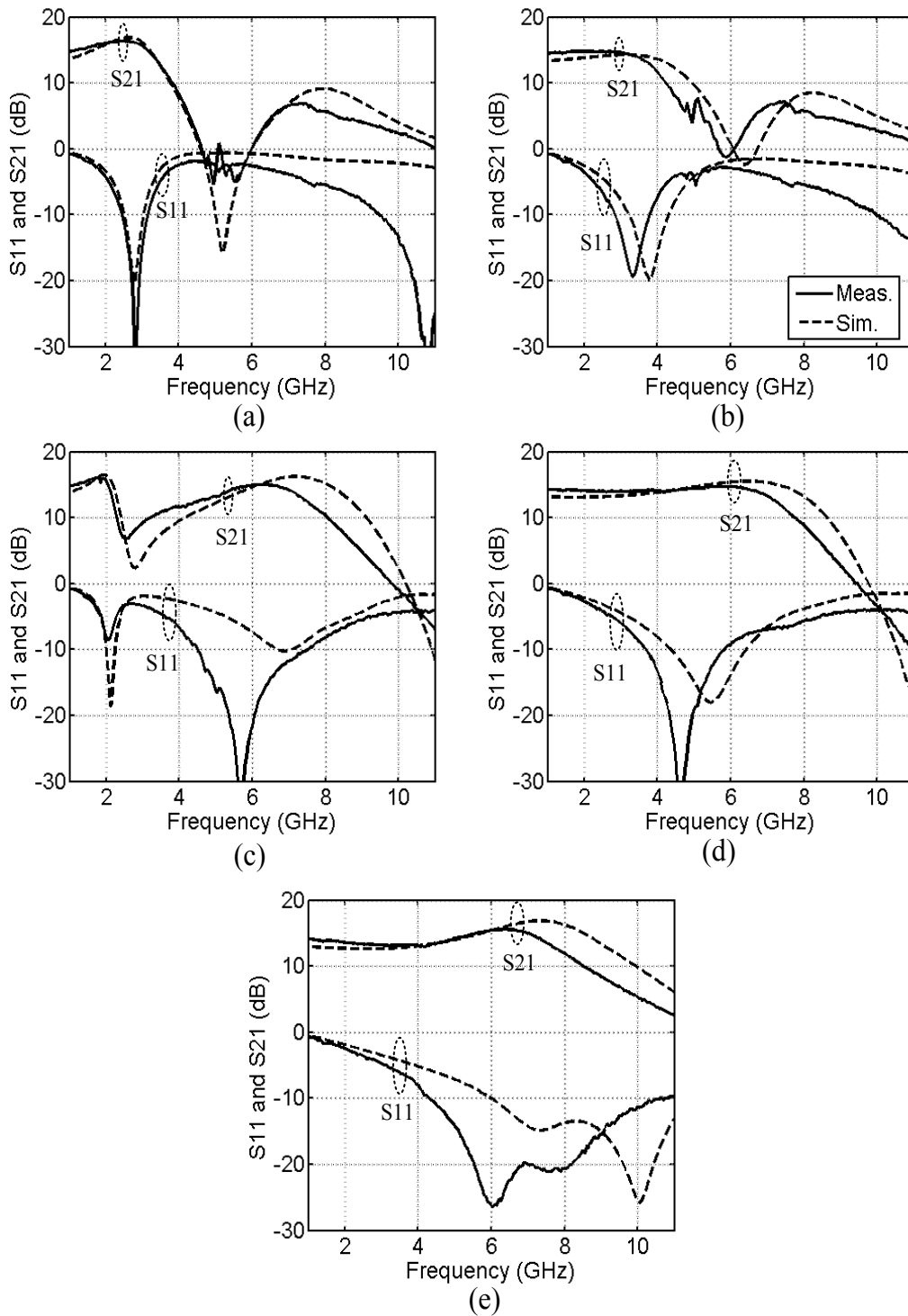


Figure 4.10. Measured and simulated  $S_{11}$  and  $S_{21}$  for (a) mode 1, (b) mode 2, (c) mode 3, (d) mode 4, and (e) mode 5.

underestimation of the parasitic capacitance of the multi-tap transformer and the associated interconnect, the input matching in the low-band of mode 3 was degraded to -8.6 dB. The low-band gain is 14.9 dB.

There are two ways in which the bandwidth can be reported when the LNA is configured to operate in mode 5: 1) the -10 dB bandwidth of the input matching network or 2) the -3 dB bandwidth of the gain. The input matching is below -10 dB over the range of 4.3-10.8 GHz and the peak gain in this region is 15.6 dB. At 10.8 GHz, however, the gain has dropped to +3 dB. By constraining the maximum variation in the gain to 3 dB of the maximum (i.e., the -3 dB bandwidth) the bandwidth is reduced to 7.8 GHz.

It is seen in Fig. 4.10 that  $S_{11}$  falls below -10 dB near 10 GHz in mode 1 and 2 and it appears that dual-band matching is achieved. The gain at these frequencies, however, is near zero and so mode 1 and 2 are considered to have single-band operation. The gain peaking near 7.5 GHz (seen in Fig. 4.10(a) and (b)) is due to the shunt peaking of the load network. With all 5 modes considered, the proposed LNA has a -10 dB bandwidth spanning from 2 GHz to 10.8 GHz and the gain is greater than 10 dB up to 8.5 GHz. To date, this is the largest amount of flexibility reported in the literature.

The noise figure (NF) was measured using the Y-factor method using an Agilent N4001A noise source and a Tektronix RSA 6114A spectrum analyzer. To effectively de-embed the noise of the spectrum analyzer, a Mini-Circuits ZX60-6013E-S amplifier was used before the network analyzer. Due to the limited bandwidth of the ZX60-6013E-S, the NF can only be measured up to approximately 8 GHz. Fig. 4.11 shows the measured and simulated NF for all five modes. The LNA exhibits a NF of 1.9–3.0 dB, 2.4–4.1 dB, and 2.7–5.1 dB over the matched bands of mode 1, 2, and 4, respectively. In mode 3, the NF is measured to

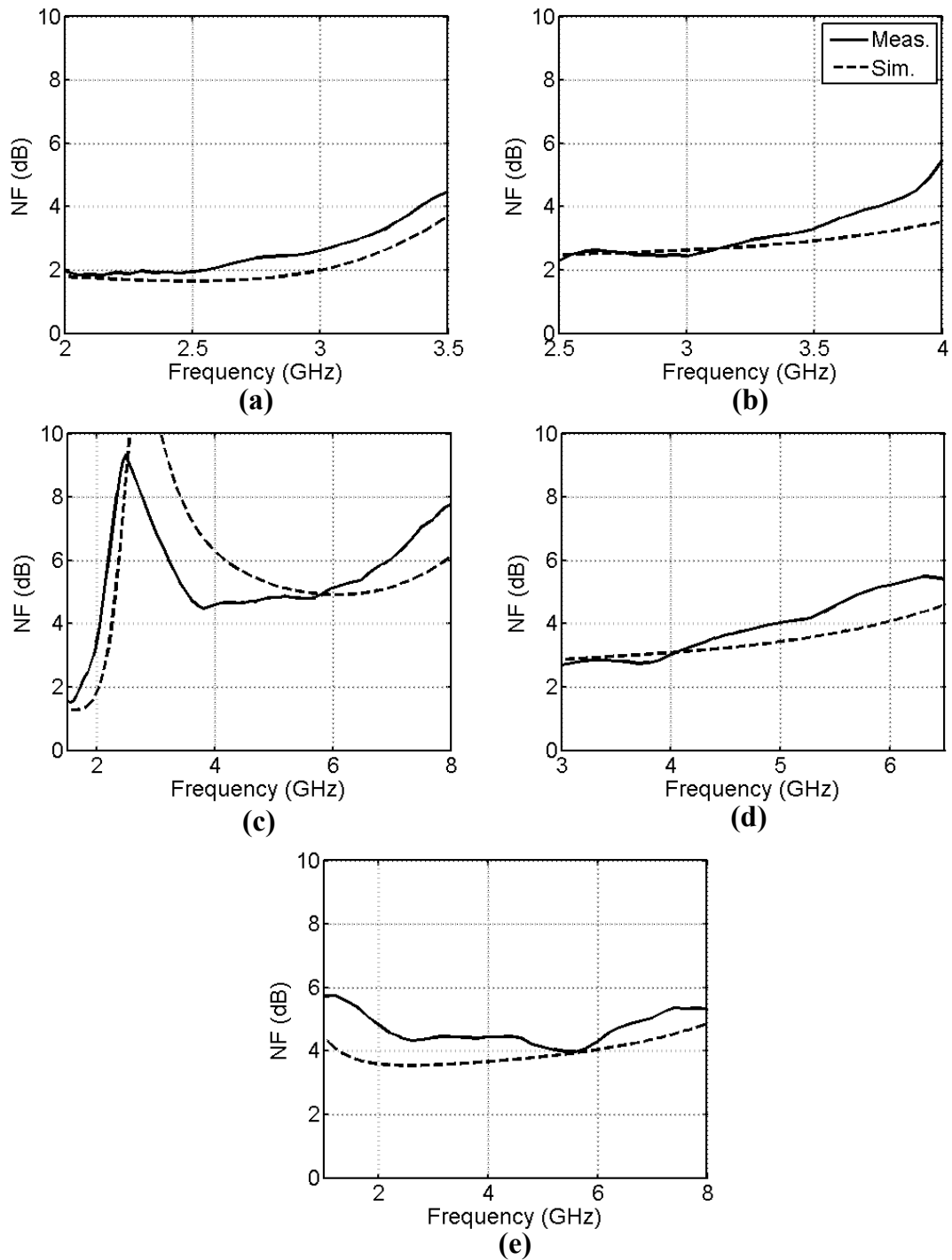


Figure 4.11. Measured and simulated noise figure for (a) mode 1, (b) mode 2, (c) mode 3, (d) mode 4, and (e) mode 5.

be 4.0 dB in the low-band and 4.7–7 dB in the high-band. Finally, the measured NF in mode 5 is 4.0–5.3 dB within the measured -10 dB matching band.

The relatively high NF seen at higher frequencies is due to the reduced gain of the LNA. High noise figures are also observed in the low-band of mode 3 because of the undesired frequency shift of the narrow-band matching network that was previously discussed.

The linearity of the proposed LNA was characterized using a standard two-tone test. The two tones, having equal amplitude and separated by 5 MHz, were generated using an Agilent E4438C vector signal generator and applied to the input of the proposed LNA. The measured IIP3 is shown in Fig. 4.12. Due to limitations in the frequency range of the E4438C, the linearity was only measured up to 6 GHz, but it is expected that the results seen in Fig. 4.12 would be consistent across the entirety of the LNA's bandwidth. The measured

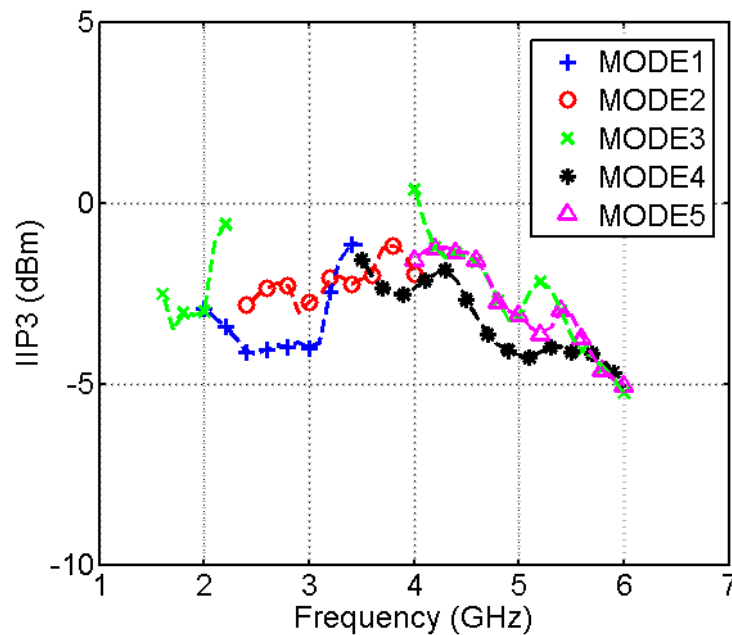


Figure 4.12. Measured IIP3 of the proposed multi-mode LNA across the bands for all 5 modes.

IIP3 varies between -4 dBm and -2 dBm in mode 1, 2, and 4; -5.3 dBm and +0.4 dBm in mode 3; and -5.0 dBm and -1.2 dBm in mode 5.

The performance of the proposed multi-mode LNA is compared with previously reported reconfigurable single-band [8, 38], concurrent dual-band [9, 10], and ultra-wideband [4, 5, 52, 53] LNAs and the results are summarized in Table 4.3. It is seen that the proposed LNA has the highest degree of flexibility and the performance is competitive in terms of gain, noise figure, linearity, and power consumption.

The significantly smaller area of the system reported in [8] comes from the replacement of the series passive inductor with a tunable, active inductor. Traditionally, active inductors have not been used due to their adverse effects on the overall noise figure. This drawback is seen in the higher noise figure of [8] in conjunction with a significantly larger power consumption.

The large gain presented in [38] is due to the two-stage structure that was used. This allowed the gain to be optimized for each operating band rather than finding a tradeoff that is good over all bands. It is noticed in Table 4.3 that the proposed LNA operating in mode 5 and the ultra-wideband LNA of [53], both of which are based on the common-source architecture, exhibit an input matching bandwidth that is larger than the -3 dB bandwidth but a significantly smaller gain and larger noise figure at higher frequencies than the reactive feedback wideband LNAs of [4, 5]. Though the reactive feedback architecture, due to its wideband characteristic, cannot be directly applied to the proposed LNA to improve the noise performance, feedforward-based noise cancellation techniques [54, 55] may be adopted.

Table 4.3. Summary of LNA performance and comparison to previously published designs

Ref.	Tech.	Freq. (GHz)	S <sub>11</sub> (dB)	S <sub>21</sub> (dB)	NF (dB)	IIP3 (dBm)	Power (mW)	Area (mm <sup>2</sup> )	Note	
<b>This Work</b>	0.13μm CMOS	2.8	-32.8	16.1	2.4	-4.0	6.4	0.73† 0.44‡	<b>Single band</b>	Mode 1
		3.3	-18.6	14.2	3.0	-2.0				Mode 2
		4.6	-35.4	14.2	3.7	-3.2				Mode 4
		2.05	-8.6	14.9	4.0	-2.0			<b>Concurrent dual-band</b>	Mode 3
		5.65	-32.4	14.9	4.8	-4.2				
		4 ~ 7.8 (4.3~10.8 <sup>Δ</sup> )	<-10	15.6 (3.0~15.6 <sup>Δ</sup> )	4.0~5.3*	-5.0 ~ -1.2**			<b>Ultra-wideband</b>	Mode 5
[8]	0.13μm CMOS	1.9~2.4	-17~-25	14~10***	3.2~3.7	-6.7	17	0.083‡	Reconfigurable single band	
[38]	0.13μm CMOS	2.4 ~ 5.4	< -12	22 ~ 24	2.2 ~ 3.1	-16 ~ -21	4.6	0.49‡		
[9]	0.35μm CMOS	2.45 5.25	-25 -15	14 15.5	2.3 4.5	0 5.6	10	0.64†	Concurrent dual-band	
[10]	0.13μm CMOS	2.45 6	-12.6 -21	9.4 18.9	2.8 3.8	-4.3 -5.6	2.79	0.61† 0.36‡		
[4]	0.13μm CMOS	2.2 ~ 10.3 (2.2~10.6 <sup>Δ</sup> )	< -9.9	16.5	2.1~2.9	-8.5 ~ -5.1	9	0.87†	Ultra-wideband	
[5]	0.18μm CMOS	1 ~ 8 (1 ~ 9 <sup>Δ</sup> )	< -10	16.5	1.9~2.65	-2 ~ 3	10.8	1.056†		
[52]	90 nm CMOS	2.6 ~ 10.2 (2.6 ~ 10.6 <sup>Δ</sup> )	< -9	12.5	3 ~ 7	—	7.2	0.64†		
[53]	0.18μm CMOS	2.6 ~ 9.2 (2.6 ~ 11.7 <sup>Δ</sup> )	< -9.9	9.3 (1 ~ 9.3 <sup>Δ</sup> )	4 ~ 9.5	-6.7	9	1.1†		

\* Measured up to 8 GHz; \*\* Measured up to 6 GHz; \*\*\* Voltage gain; Δ S<sub>11</sub> < -10 or -9 band; † Including Pads; ‡ Excluding Pads

#### 4.4 Summary

A multi-tap transformer-based reconfigurable multi-mode LNA is proposed and fabricated in 0.13  $\mu\text{m}$  CMOS. To the authors' best knowledge, it is the first reported LNA capable of single band, concurrent dual-band, and ultra-wideband operation and is among the largest bandwidths reported in literature. This is achieved with a novel, reconfigurable, multi-mode input matching network that naturally integrates a switched multi-tap transformer into an inductively degenerated common source amplifier. The proposed LNA achieves single band matching at 2.8 GHz, 3.3 GHz, and 4.6 GHz; concurrent dual-band matching at 2.05 GHz and 5.65 GHz; and ultra-wideband matching from 4.3 GHz to 10.8 GHz. The power gain of 14.7 – 16.4 dB, noise figure of 1.9 – 4.7 dB, and IIP3 of -2 – +0.4 dBm across all bands. The chip occupies an area of  $1.04 \times 0.7 \text{ mm}^2$ , and has a power dissipation of 6.4 mW from a 1.2 V supply. It provides one of the simplest LNA solutions for reconfigurable radios and the topology is a good candidate for software defined and cognitive radio.

## CHAPTER 5. TRANSFORMER-BASED TRIPPLE-MODE VOLTAGE CONTROLLED OSCILLATOR

In multi-standard multi-band RF systems, the voltage controlled oscillator (VCO) is a key building block that limits the operating frequency range. To cover a wide range of frequencies, most reported VCOs targeting such applications have focused on achieving a wide-tuning range with good phase noise. Though the tuning range of the oscillators has been extended to several GHz, only a single frequency can be generated at a time in those oscillators [13, 15, 17-20, 35, 36]. As the introduction of inter-band carrier aggregation techniques, such as in 3GPP LTE [2], it needs two or more local oscillator frequencies at the same time. A straight forward solution is to use several oscillators. Unfortunately, the approach suffers significant problem with power consumption and die area. To save power and area, an oscillator capable of generating two or more frequencies simultaneously becomes very attractive. Oscillators generating multiple independent frequencies simultaneously have been studied since the 1920's [56-61]. It is shown that active devices must be highly nonlinear for stable simultaneous oscillations [62, 63]. Recently, integrated concurrent dual-frequency oscillators was first reported in 0.18  $\mu\text{m}$  SiGe BiCMOS [22]. To enable a low cost solution in CMOS, a triple mode VCO with a transformer-based high order tank, consisting of two magnetic coupled 2<sup>nd</sup> order tanks, shown in Fig. 5.1, was then demonstrated in 65 nm CMOS to generate two frequencies either concurrently or one at a time [23]. In the concurrent dual-oscillation mode, the MOS transistors,  $M_1$  and  $M_2$ , were



design details and the experimental results of a prototype triple-mode VCO will be presented in Section 5.3. Finally, this chapter concludes in Section 5.4.

## 5.1 Multi-Frequency Oscillator

The block diagram of a conceptual dual-frequency oscillator is shown in Fig. 5.2, including a 4<sup>th</sup> order tank, denoted by its impedance, and a nonlinear negative transconductance,  $gm$ , generator. The tank resonates at the frequency of  $\omega_L$  and  $\omega_H$ , and may be realized by inductor- and transformer-based resonator, shown in Fig. 2.3 (a)(d) and Fig. 2.9 (a), while the  $gm$  compensates the tank loss at  $\omega_L$  and  $\omega_H$ . The transconductance is not only frequency dependent, but also very nonlinear in order to sustain concurrent dual oscillation [23, 30].

Fig. 5.3 illustrates an ideal output waveform of an oscillator oscillating at 3 GHz and 5 GHz simultaneously with equal amplitude of 1 V. Assuming the transconductance is realized with cross-coupled pairs, acting as ideal switches, with a total bias current of 1 mA, the current flowing in the tank will be a series of pulses with amplitude of  $\pm 1$  mA, shown in Fig. 5.4 (a). When the tank exhibits the same impedance at 3GHz and 5 GHz, the current

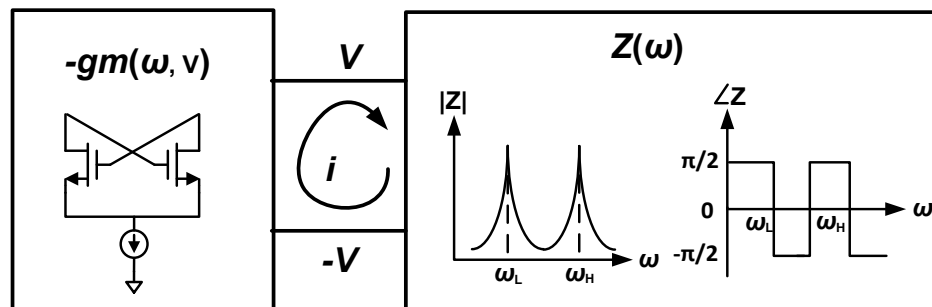


Figure 5.2. Block diagram of a conceptual multi-frequency oscillator.

has same amplitude at 3. The corresponding frequency spectrum is shown in Fig. 5.4 (b). At 3GHz and 5 GHz, the current amplitude is about 0.32 mA. To generate the output waveform in Fig. 5.2, an ideal 4<sup>th</sup> order tank is needed, acting as a band-pass filter with passing band at 3 GHz and 5 GHz respectively, to filter out the harmonics. The equivalent impedance needs to be about 3125  $\Omega$  at both frequencies to achieve 1 V voltage amplitude at 3 GHz and 5 GHz, respectively.

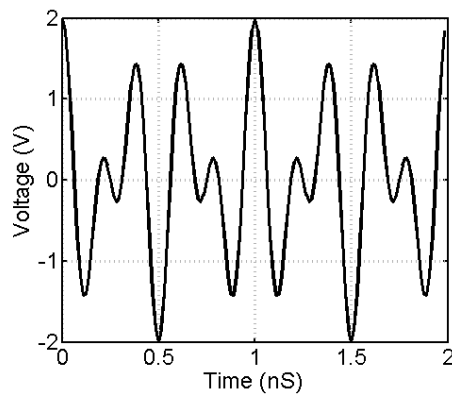


Figure 5.3. Ideal output waveform of an oscillation oscillating at 3 GHz and 5 GHz simultaneously.

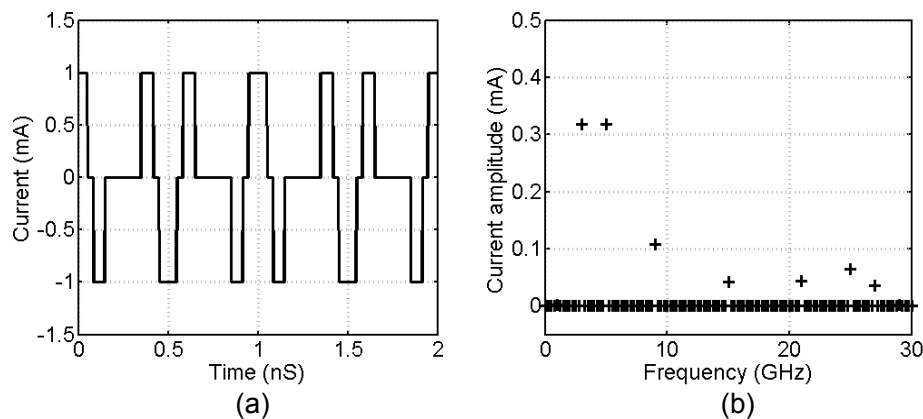


Figure 5.4. Corresponding (a) current waveform following in the tank and (b) its frequency spectrum when the gm is realized with ideal switches and the ideal 4<sup>th</sup> order tank has the same impedance at 3 GHz and 5 GHz.

## 5.2 Operation of Dual-Coupled Triple-Mode VCO

Fig. 5.5 shows the schematic the proposed dual-coupled VCO (DC-VCO), consisting of a transformer-based 4<sup>th</sup> –order tank with a cross-coupled transistor pair,  $M_1$  and  $M_2$ , on its primary winding, and a pair of transistors,  $M_3$  and  $M_4$ , coupling between the primary and secondary windings. The output is taken from the primary winding. The transconductance of the transistors,  $M_1/M_2$  and  $M_3/M_4$ , are  $g_{m1}$  and  $g_{m2}$ , respectively. The DC-VCO oscillates at a single frequency when only a pair of the transistors is enabled, while it oscillates at two

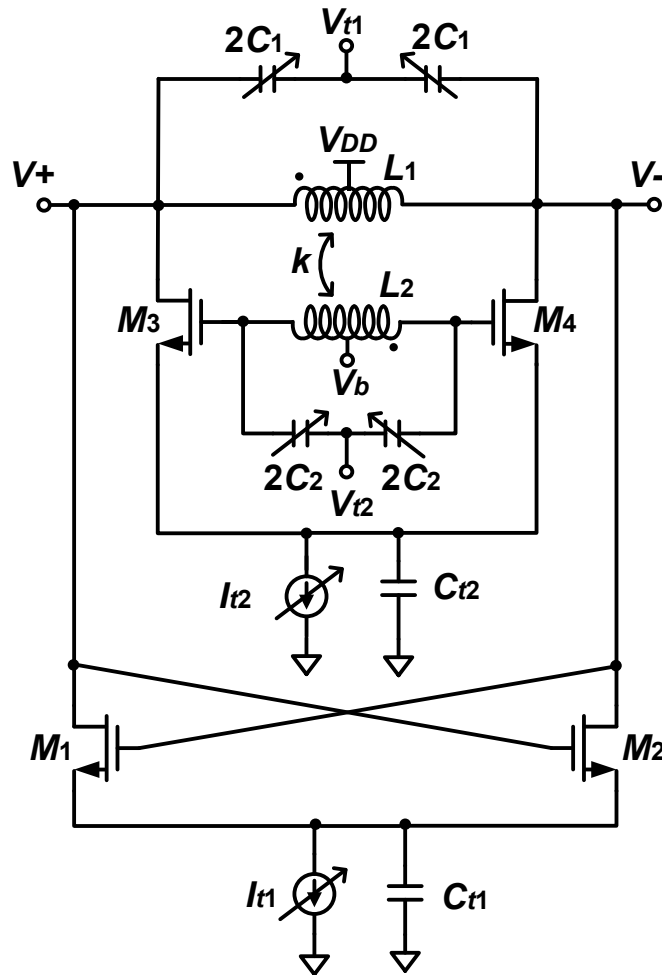


Figure 5.5. Schematic of the proposed dual-coupled triple-mode VCO.

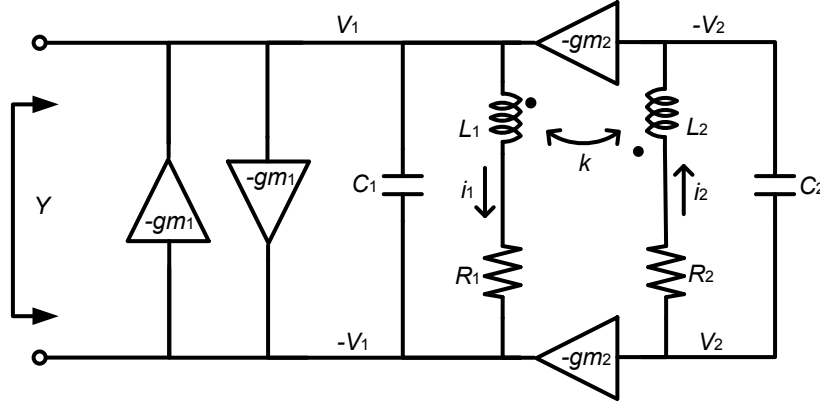


Figure 5.6. Small signal model of the proposed triple mode VCO.

frequencies simultaneously when both transistor pairs are enabled. We will study the oscillation condition of the oscillator using a simplified 1-port network model, shown in Fig. 5.6.

### 5.2.1 Oscillation frequency and start-up conditions

The admittance of the 1-port network can be expressed as:

$$Y = -\frac{gm_1}{2} + sC_1 + \frac{1}{Z'_1} - \frac{gm_2}{2} \frac{v_2}{v_1}. \quad (5-1)$$

where  $C_1$  is the capacitance across the primary tank, respectively,  $Z'_1$  is the effective impedance of the primary inductor,  $v_1$  and  $v_2$  are the AC voltages at the oscillation nodes of the primary and secondary tanks, respectively. The expression of  $Z'_1$  and  $v_2/v_1$  can be obtained by applying KVL and KCL to the model and solving the following equations:

$$2v_1 = i_1 Z'_1 \quad (5-2)$$

$$2v_1 = i_1(sL_1 + R_1) + i_2 sM \quad (5-3)$$

$$2v_2 = i_2(sL_2 + R_2) + i_1 sM \quad (5-4)$$

$$i_2 = -2v_2 sC_2, \quad (5-5)$$

where  $L_1$  and  $R_1$  are the self-inductance and parasitic resistance of the primary turn,  $L_2$  and  $R_2$  are the self-inductance and parasitic resistance of the secondary turn,  $M = k\sqrt{L_1L_2}$  is the mutual inductance of the transformer and  $k$  is the coupling coefficient. Solving (5-2)-(5-5), we get

$$Z'_1 = sL_1 + R_1 - \frac{s^2M^2}{Z_{2,loop}}, \quad (5-6)$$

where  $Z_{2,loop} = sL_2 + R_2 + \frac{1}{sC_2}$ .

The voltage ratio from primary to secondary turn is given as

$$\frac{v_2}{v_1} = \frac{M/C_2}{Z'_1 Z_{2,loop}} = \frac{M/C_2}{(sL_1 + R_1)(sL_2 + R_2 + \frac{1}{sC_2}) - s^2M^2}. \quad (5-7)$$

Then, the admittance  $Y$  is expressed as:

$$Y = -\frac{gm_1}{2} + sC_1 + \frac{sL_2 + R_2 + \frac{1}{sC_2}}{(sL_1 + R_1)(sL_2 + R_2 + \frac{1}{sC_2}) - s^2M^2} - \frac{gm_2}{2} \frac{M/C_2}{(sL_1 + R_1)(sL_2 + R_2 + \frac{1}{sC_2}) - s^2M^2}. \quad (5-8)$$

The impedance of  $Z'_1$  and the voltage ratio may be expressed in the resonant frequencies of the primary and secondary tanks and the quality factor of the primary and secondary inductors as follows:

$$\frac{1}{Z'_1} = \frac{\frac{1}{\omega L_1} \left( \frac{1}{Q_2} + j \left( 1 - \left( \frac{\omega_2}{\omega} \right)^2 \right) \right)}{\left( \frac{\omega_2}{\omega} \right)^2 - 1 + k^2 + \frac{1}{Q_1 Q_2} + j \left( \frac{1}{Q_2} + \frac{1}{Q_1} \left( 1 - \left( \frac{\omega_2}{\omega} \right)^2 \right) \right)} \quad (5-9)$$

$$\frac{v_2}{v_1} = \frac{k \sqrt{\frac{L_2}{L_1}} \left( \frac{\omega_2}{\omega} \right)^2}{\left( \frac{\omega_2}{\omega} \right)^2 - 1 + k^2 + \frac{1}{Q_1 Q_2} + j \left( \frac{1}{Q_2} + \frac{1}{Q_1} \left( 1 - \left( \frac{\omega_2}{\omega} \right)^2 \right) \right)} \quad (5-10)$$

where  $\omega_1 = 1/\sqrt{L_1 C_1}$ ,  $\omega_2 = 1/\sqrt{L_2 C_2}$ ,  $Q_1 = \omega L_1/R_1$ , and  $Q_2 = \omega L_2/R_2$ .

When the oscillator oscillates, there is zero phase shifts in the tank. Thus, the oscillation frequency can be obtained by letting:

$$\text{Im}(Y) = \omega C_1 + \text{Im}\left(\frac{1}{Z_1'}\right) - \frac{g_{m2}}{2} \text{Im}\left(\frac{v_2}{v_1}\right) = 0 \quad (5-11)$$

To gain some insight, high quality factors of the inductors are assumed, that is  $1/Q_1 \ll 1$  and  $1/Q_2 \ll 1$ , to simplify the analysis. By analyzing (9-11), the resonant frequencies can be approximated as:

$$\omega_L^2 = \frac{\omega_1^2 + \omega_2^2 - \sqrt{\omega_1^4 + \omega_2^4 + \omega_1^2 \omega_2^2 (4k^2 - 2)}}{2(1-k^2)} \quad (5-12)$$

$$\omega_H^2 = \frac{\omega_1^2 + \omega_2^2 + \sqrt{\omega_1^4 + \omega_2^4 + \omega_1^2 \omega_2^2 (4k^2 - 2)}}{2(1-k^2)} \quad (5-13)$$

where

$$\omega_L < \min(\omega_1, \omega_2) < \max(\omega_1, \omega_2) < \omega_H. \quad (5-14)$$

The oscillator can potentially oscillate in three modes: 1) at a single frequency of  $\omega_L$ , 2) at a single frequency of  $\omega_H$ , and 3) at two frequencies of  $\omega_L$  and  $\omega_H$  simultaneously, depending whether the start-up condition can be met at  $\omega_L$  and  $\omega_H$  and there are enough nonlinearity in the transconductance. For start-up of oscillation, the loop gain must be larger than one at the resonant frequency base on Barkhausen's criteria. In term of the network admittance, the start-up condition can be expressed as:

$$\text{Re}(Y) = -\frac{g_{m1}}{2} + \text{Re}\left(\frac{1}{Z_1'}\right) - \frac{g_{m2}}{2} \text{Re}\left(\frac{v_2}{v_1}\right) < 0. \quad (5-15)$$

It requires  $\text{Re}(Y)|_{\omega=\omega_L} < 0$  and  $\text{Re}(Y)|_{\omega=\omega_H} > 0$  to start oscillation only at  $\omega_L$  in mode 1, while it requires  $\text{Re}(Y)|_{\omega=\omega_L} > 0$  and  $\text{Re}(Y)|_{\omega=\omega_H} < 0$  to start oscillation only at  $\omega_H$ . To start oscillation at both frequencies, it requires  $\text{Re}(Y)|_{\omega=\omega_L} < 0$  and  $\text{Re}(Y)|_{\omega=\omega_H} < 0$ .

From (5-15), it seems that the three modes of operation may be achieved by properly choosing the transconductance of  $g_{m1}$  and  $g_{m2}$ . However, it also depends on the relationship

between  $\omega_1$  and  $\omega_2$ . When  $\omega_1 > \omega_2$ , three modes of operation can be achieved, but when  $\omega_1 < \omega_2$ , it can only oscillate at  $\omega_L$ . That is because that the impedance of  $Z'_1$  and the voltage ratio of  $v_2/v_1$  are frequency dependent.

From (5-9), it is seen that there is a critical frequency at

$$\omega_c = \frac{\omega_2}{\sqrt{1-k^2+1/Q_1Q_2}}, \quad (5-16)$$

where the impedance of  $Z'_1$  decrease sharply, meaning increased loss, around the frequency of  $\omega_c$ . For a typical coupling coefficient of  $k$ ,  $\omega_c$  is slightly larger than  $\omega_2$ . From (5-15), it can be inferred that  $\omega_H$  is closer to  $\omega_c$  than  $\omega_L$  is and  $Re(1/Z'_1)|_{\omega=\omega_L} < Re(1/Z'_1)|_{\omega=\omega_H}$  when  $\omega_1 < \omega_2$ . While,  $\omega_L$  is closer to  $\omega_c$  than  $\omega_H$  is and  $Re(1/Z'_1)|_{\omega=\omega_L} > Re(1/Z'_1)|_{\omega=\omega_H}$  when  $\omega_1 > \omega_2$ . To illustrate this, the effective conductance of the primary inductor in a transformer-based tank with resonant frequency of 3 and 5.6 GHz are plotted using the extracted inductance, series parasitic resistance, and coupling coefficient of a designed transformer with  $L_1= 1.7$  nH,  $R_1= 3.2$   $\Omega$ ,  $L_2= 3.4$  nH,  $R_2= 3.8$   $\Omega$ ,  $k= 0.45$ , shown as case 1 in Fig. 5.7(a). The corresponding primary and secondary self-resonant frequency is  $\omega_1 = 2\pi * 4.68$  GHz and  $\omega_2 = 2\pi * 3.2$  GHz, respectively, and  $\omega_c = 2\pi * 3.58$  GHz. The conductance of  $1/Z'_1$  is 3.7 mS at 3 GHz and 2.45 mS at 5.6 GHz, respectively. By switching the connection of the primary and secondary tanks, such that  $\omega_1 = 2\pi * 3.2$  GHz and  $\omega_2 = 2\pi * 4.68$  GHz, a new effective conductance of  $1/Z'_1$  is plotted as case 2 in Fig. 5.7(a). The conductance of  $1/Z'_1$  becomes 0.83 mS at 3 GHz and 8.6 mS at 5.6 GHz, respectively.

From (5-10), it is seen that the amplitude of the voltage ratio  $v_2/v_1$  is maximized at  $\omega_c$ , meaning large voltage gain, around the frequency of  $\omega_c$ . But the polarity of  $v_2/v_1$  will change from positive to negative. When  $\omega < \omega_c$ ,  $Re(v_2/v_1) > 0$ ; while  $Re(v_2/v_1) < 0$

when  $\omega > \omega_c$ . From (5-15), it can be inferred that  $Re(v_2/v_1)|_{\omega=\omega_L} > 0 > Re(v_2/v_1)|_{\omega=\omega_H}$ . That is to say  $v_2$  is in phase with  $v_1$  and the transconductance  $g_{m2}$  will compensate the loss of the tank at  $\omega_L$ , while  $v_2$  is out of phase with  $v_1$  and the transconductance  $g_{m2}$  will add loss to the tank at  $\omega_H$ . The voltage ratio is also illustrated in Fig. 5.7(b) for the tanks used in the discussion of  $1/Z'_1$ . The voltage ratio is 2 at 3 GHz and -0.44 at 5.6 GHz, respectively, in case 1, and the voltage ratio is 0.47 at 3 GHz and -1.5 at 5.6 GHz, respectively, in case 2.

Thus, when  $\omega_1 < \omega_2$ ,  $Re(Y)$  is always smaller at  $\omega_L$  than at  $\omega_H$ . It requires smaller negative transconductance to start the oscillation at  $\omega_L$ . When  $g_{m1}$  is large enough, start-up condition might be met at both  $\omega_L$  and  $\omega_H$ , however, the oscillation at  $\omega_L$  starts faster and the oscillator will eventually oscillate at  $\omega_L$  only because  $Re(Y)|_{\omega=\omega_L}$  will become zero after the oscillation stabilizes at  $\omega_L$  thus  $Re(Y)|_{\omega=\omega_H}$  will be eventually larger than zero. The

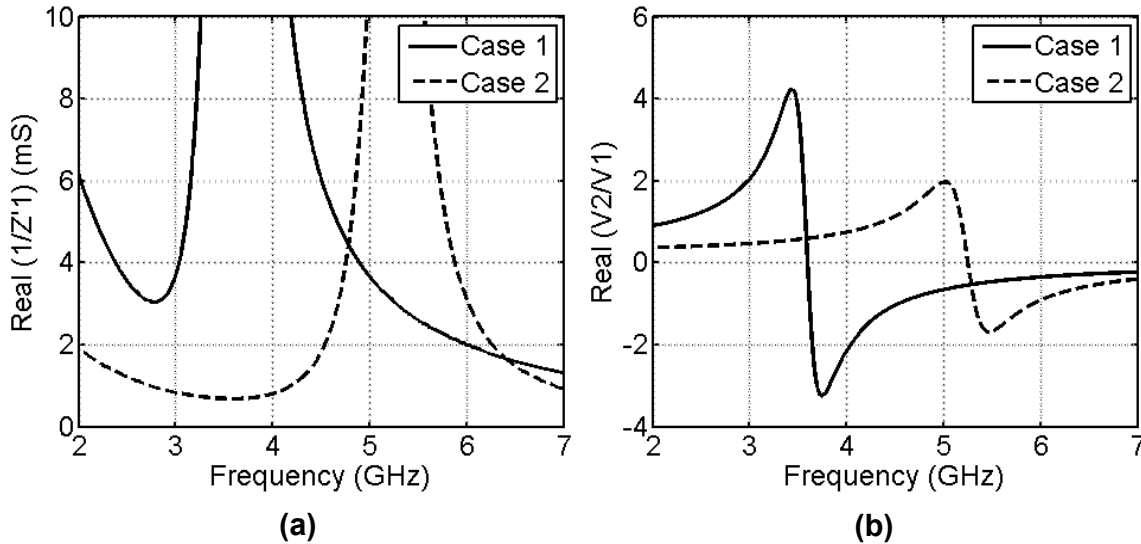


Figure 5.7. (a) Effective conductance of the primary inductor in the tank, and (b) real of the voltage ratio,  $v_2/v_1$ , between secondary and primary turn (case 1:  $L_1=1.7$  nH,  $R_1=3.5$   $\Omega$ ,  $L_2=3.4$  nH,  $R_2=3.8$   $\Omega$ ,  $k=0.45$ ,  $f_1=4.68$  GHz,  $f_2=3.2$  GHz; case 2:  $L_1=3.4$  nH,  $R_1=3.8$   $\Omega$ ,  $L_2=1.7$  nH,  $R_2=3.5$   $\Omega$ ,  $k=0.45$ ,  $f_1=3.2$  GHz,  $f_2=4.68$  GHz).

oscillation at  $\omega_H$  will die out.

When  $\omega_1 > \omega_2$ , the oscillation can be configured in the following way to achieve three modes of operation: 1)  $g_{m1} > 5.9$  mS and  $g_{m2} = 0$  for mode 1, 2)  $g_{m1} = 0$  and  $g_{m2} > 1.85$  mS for mode 2, and 3)  $g_{m1} > 5.4$  mS and  $g_{m2} > 0$  for mode 3. In mode 3,  $g_{m2}$  needs to be chosen such that the equivalent circuit of dual-coupled tank exhibits similar amplitude of impedance at  $\omega_L$  and  $\omega_H$ , in other words, it requires similar  $g_{m1}$  to start and sustain the oscillation at both frequencies. The configuration of operation modes is also summarized in Table 5.1.

Fig. 5.8 illustrates the phase and amplitude of tank impedance when  $g_{m2}$  varies from 0 to 2 mS. From Fig. 5.8(a), it is seen that  $g_{m2}$  has negligible effect on the phase, meaning

Table 5.1. Configuration of operation modes

Mode		$g_{m1}$	$g_{m2}$	Note
1	$\omega_H$ only	Active	0	$\omega_1 > \omega_2$
2	$\omega_L$ only	0	Active	
3	$\omega_L$ and $\omega_H$	Active	tuning	

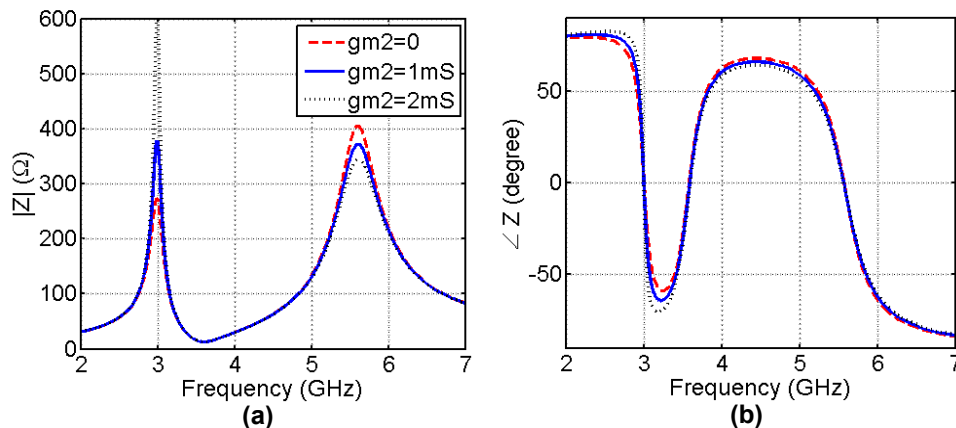


Figure 5.8. (a) Impedance and (b) phase of the tank with various  $g_{m2}$ .

that the oscillation frequency stays the same. Fig. 5.8(b) shows that the amplitude of the tank impedance increases at  $\omega_L$  while decreases at  $\omega_H$  as  $g_{m2}$  increases, implying that it becomes easier to start an oscillation at  $\omega_L$  and becomes harder to start an oscillation at  $\omega_H$  as  $g_{m2}$  increases. The oscillation modes can be gradually changed from single oscillation at  $\omega_H$  only, to concurrent oscillation at  $\omega_L$  and  $\omega_H$ , and finally to single oscillation at  $\omega_L$  only. In the concurrent dual resonant mode,  $g_{m2}$  is small and the start-up of oscillation is set by  $g_{m1}$ , which is much greater than  $g_{m2}$ .

### 5.2.2 Oscillation amplitude and stable oscillation condition

After the oscillation starts-up, the oscillation amplitude rises and the transistors become strongly nonlinear such that the transconductance on average is reduced until the oscillator reaches steady state when the tank loss is completely compensated by the average transconductance. The steady state oscillation condition of the proposed oscillator can be expressed as:

$$-\frac{G_{m1}}{2} + Re\left(\frac{1}{Z'_1}\right) - \frac{G_{m2}}{2} Re\left(\frac{v_2}{v_1}\right) = 0, \quad (5-17)$$

where  $G_{m1}$  and  $G_{m2}$  are the corresponding large signal transconductance of  $g_{m1}$  and  $g_{m2}$  at the resonant frequency  $\omega_o$ , respectively, and are a function of the non-differential oscillation amplitude of  $A_1$  and  $A_2$  in the primary and secondary tank, respectively.  $Re(1/Z'_1)$  and  $Re(v_2/v_1)$  represent the tank conductance at  $\omega_o$  looking into the primary winding and voltage gain from the secondary winding to the primary winding at  $\omega_o$ , respectively. In mode 1 and 2,  $\omega_o = \omega_H$  and  $\omega_o = \omega_L$ , respectively. In mode 3,  $\omega_o = \omega_H$  and  $\omega_L$ .

To simplify the analysis, the transistors,  $M_1$ ,  $M_2$ ,  $M_3$  and  $M_4$ , are assumed to act as ideal switches. Thus, their drain current waveforms are a series of periodic pulses. Their

period,  $T$ , duty cycle,  $D$ , and amplitude,  $I_{pk}$ , relate to their modes of operation. In mode 1, the oscillator oscillates at a single frequency of  $\omega_H$  with  $I_{t2} = 0$  and  $G_{m2} = 0$ . The large signal transconductance  $G_{m1}$  can be expressed as:

$$G_{m1,mod1} \approx \frac{1}{\pi D_{mod1}} \frac{I_{t1}}{A_{1,mod1}} \sin(\pi D_{mod1}). \quad (5-18)$$

where  $A_{1,mod1}$  is the oscillation amplitude at the terminals of the primary windings,  $L_1$ ,  $D_{mod1}$  is the duty cycle of the drain current of the transistors,  $M_1$  and  $M_2$ , in mode 1. From (5-17)(5-18), the oscillation amplitude can be given as:

$$A_{1,mod1} \approx \frac{1}{2\pi D_{mod1}} I_{t1} R_{p,\omega_H} \sin(\pi D_{mod1}), \quad (5-19)$$

where  $R_{p,\omega_H} = \frac{1}{\text{Re}\left(\frac{1}{Z_1}\right)\bigg|_{\omega=\omega_H}}$  is the equivalent parallel tank resistant at  $\omega_H$ .

In mode 2, the oscillator oscillates at a single frequency of  $\omega_L$ . When the oscillator oscillates at a single frequency of  $\omega_L$  with  $I_{t1} = 0$  and  $G_{m1} = 0$ . Similarly, the large signal transconductance  $G_{m2}$  and the oscillation amplitude at  $\omega_L$  can be given as:

$$G_{m2,mod2} \approx \frac{1}{\pi D_{mod2}} \frac{I_{t2}}{A_{1,mod2} \left| \frac{v_2}{v_1} \right|_{\omega=\omega_L}} \sin(\pi D_{mod2}), \quad (5-20)$$

where  $D_{mod2}$  is the duty cycle of the drain current of the transistors,  $M_3$  and  $M_4$ , in mode 2, and  $\left| \frac{v_2}{v_1} \right|_{\omega=\omega_L}$  is the voltage gain amplitude from the secondary winding to the primary winding at  $\omega_L$ . Because  $v_2$  is in phase with  $v_1$  at  $\omega_L$ ,  $\left| \frac{v_2}{v_1} \right|_{\omega=\omega_L} = \text{Re}(v_2/v_1)\big|_{\omega=\omega_L}$ . From (5-17)(5-20), the oscillation amplitude at the terminals of the primary winding,  $L_1$ , is given as:

$$A_{1,mod2} \approx \frac{1}{2\pi D_{2,\omega_L}} I_{t2} R_{p,\omega_L} \sin(\pi D_{mod2}). \quad (5-21)$$

where  $R_{p,\omega_L} = \frac{1}{\text{Re}\left(\frac{1}{Z_1}\right)\bigg|_{\omega=\omega_L}}$  is the equivalent parallel tank resistant at  $\omega_L$ .

In mode 3, the oscillator oscillates at two frequencies simultaneously. By neglecting the harmonics and intermodulation components for simplified analysis, the output signal can be expressed as:

$$v_1(t) = A_{1,\omega_L} \cos(\omega_L t + \phi_L) + A_{1,\omega_H} \cos(\omega_H t + \phi_H), \quad (5-22)$$

where  $A_{1,\omega_L}$  and  $A_{1,\omega_H}$  are the oscillation amplitude at the frequency  $\omega_L$  and  $\omega_H$ , respectively, in mode 3. Then, the drain current of the transistors,  $M_1$  and  $M_2$ , can be assumed to be a combination of two series of periodic pulses with period of  $1/2\pi\omega_L$  and  $1/2\pi\omega_H$ , respectively, and duty cycle of  $D_{1,\omega_L}$  and  $D_{1,\omega_H}$ , respectively. The bias currents,  $I_{t1}$ , are assumed to be equally divided between the pulses. Similarly, the drain current of the transistors,  $M_3$  and  $M_4$ , is also assumed a combination of two series of periodic pulses with period of  $1/2\pi\omega_L$  and  $1/2\pi\omega_H$ , respectively, and duty cycle of  $D_{2,\omega_L}$  and  $D_{2,\omega_H}$ , respectively. The bias currents,  $I_{t2}$ , are assumed to be equally divided between the pulses. Then, the large signal transconductance  $G_{m1}$  and  $G_{m2}$  at the two frequencies  $\omega_L$  and  $\omega_H$  can be expressed as:

$$G_{m1,\omega_L} \approx \frac{1}{2\pi D_{1,\omega_L}} \frac{I_{t1}}{A_{1,\omega_L}} \sin(\pi D_{1,\omega_L}) \quad (5-23)$$

$$G_{m1,\omega_H} \approx \frac{1}{2\pi D_{1,\omega_H}} \frac{I_{t1}}{A_{1,\omega_H}} \sin(\pi D_{1,\omega_H}) \quad (5-24)$$

$$G_{m1,\omega_L} \approx \frac{1}{2\pi D_{1,\omega_L}} \frac{I_{t1}}{A_{1,\omega_L}} \sin(\pi D_{1,\omega_L}) \quad (5-25)$$

$$G_{m1,\omega_H} \approx \frac{1}{2\pi D_{1,\omega_H}} \frac{I_{t1}}{A_{1,\omega_H}} \sin(\pi D_{1,\omega_H}) \quad (5-26)$$

where  $\left|\frac{v_2}{v_1}\right|_{\omega=\omega_L} = \text{Re}\left(\frac{v_2}{v_1}\right)\Big|_{\omega=\omega_L}$  and  $\left|\frac{v_2}{v_1}\right|_{\omega=\omega_H} = -\text{Re}\left(\frac{v_2}{v_1}\right)\Big|_{\omega=\omega_H}$  because  $v_1$  and  $v_2$  are in phase at  $\omega_L$  while are out of phase at  $\omega_H$ . Solving (5-17)(5-23)-(5-26) for the frequencies of  $\omega_L$  and  $\omega_H$ , the oscillation amplitude at the terminals of the primary winding can be given as (5-27) an (5-28), respectively:

$$A_{1,\omega_L} \approx \frac{1}{4\pi D_{1,\omega_L}} I_{t1} R_{p,\omega_L} \sin(\pi D_{1,\omega_L}) + \frac{1}{4\pi D_{2,\omega_L}} I_{t2} R_{p,\omega_L} \sin(\pi D_{2,\omega_L}) \quad (5-27)$$

$$A_{1,\omega_H} \approx \frac{1}{4\pi D_{1,\omega_H}} I_{t1} R_{p,\omega_H} \sin(\pi D_{1,\omega_H}) - \frac{1}{4\pi D_{2,\omega_H}} I_{t2} R_{p,\omega_H} \sin(\pi D_{2,\omega_H}). \quad (5-28)$$

From (5-19)(5-21)(5-27)(5-28), it is seen that the oscillation amplitude depends on the duty cycle, which depends on the operating conditions, such as the gate biasing voltage, the tail current, etc. For a conventional cross-coupled VCO, the drain current is normally assumed to be square wave, in other word, the duty cycle is 50%. When a tail capacitor is included in parallel with the tail current source [64], the tail current is shaped such that duty cycle of the drain current is less than 50%, thus the voltage amplitude is increased. Comparing to the oscillation amplitude of a conventional cross-coupled VCO, the amplitude is boosted by 4/3 times in [64]. The amplitude is boosted by  $\pi/2$  times when the duty cycle is near zero, corresponding to Class-C operation [65]. However, this requires the gate of the transistors to be biased at a lower voltage than the supply voltage in addition to using the tail capacitors.

From (5-27)(5-28), it is also seen that the oscillation amplitude is increased at the low frequency while the amplitude is reduced at the high frequency as the tail current,  $I_{t2}$ , increases, implying that concurrent dual-oscillation with similar amplitude can be achieved by tuning the tail current  $I_{t2}$ . But, a large  $I_{t2}$  would degrade the performance at the high frequency band. In order to avoid the use of a large  $I_{t2}$ , the transformer-based tank should be

designed such that.  $R_{p,\omega_L}$  is only slightly smaller than  $R_{p,\omega_H}$ . A small difference between  $R_{p,\omega_L}$  and  $R_{p,\omega_H}$  would also help maintain stable concurrent dual oscillation easier.

### 5.2.3 Choice of the coupling coefficient

To implement a transformer-based 4<sup>th</sup>-order tank with the desired resonant frequencies of  $\omega_L$  and  $\omega_H$ , the coupling coefficient,  $k$ , must meet the following condition:

$$k \leq \frac{\omega_H^2 - \omega_L^2}{\omega_H^2 + \omega_L^2}. \quad (5-29)$$

The upper bound of the coupling coefficient,  $k$ , with respect to the frequency ratio,  $\omega_H/\omega_L$ , is plotted in Fig. 5.9. With a smaller frequency ratio, the upper bound of  $k$  reduces. A ratio of less than 2 is desired to avoid the potential disturbance to the high frequency,  $\omega_H$ , due to the 2<sup>nd</sup> and higher order harmonics of the lower frequency,  $\omega_L$ , in the concurrent dual-oscillation mode, thus  $k$  should be less than 0.6. However, a very small  $k$  will result in a large area of the transformer.

For the same desired resonant frequencies of  $\omega_L$  and  $\omega_H$ , it results in different sets of required self-resonant frequencies of the primary and secondary tanks,  $\omega_1$  and  $\omega_2$ , when different  $k$  is chosen. The impedance and quality factor of the tank at  $\omega_L$  and  $\omega_H$  will also change. A larger  $k$  leads to a higher impedance and quality factor at low band, while gives lower impedance and quality factor at high band [35]. The impedance of a tank with resonant frequencies of  $\omega_L = 2\pi \cdot 3$  GHz,  $\omega_H = 2\pi \cdot 5.6$  GHz for various coupling coefficients,  $k$ , is plotted in Fig. 5.10, where the inductance and the loss of the primary and secondary inductors are kept the same as the extracted values of the designed transformer ( $L_1 = 1.7$  nH,  $R_1 = 3.2$   $\Omega$ ,  $L_2 = 3.4$  nH, and  $R_2 = 3.8$   $\Omega$ ) for the VCO. To achieve balanced impedance at 3GHz and 5.6

GHz, the desired  $k$  is in the range of 0.35-0.55. As discussed in Section 5.2.1, the proposed VCO requires slightly lower impedance at the low oscillation frequency. A  $k$  of 0.45 will be chosen for the transformer later in the design of the proposed VCO.

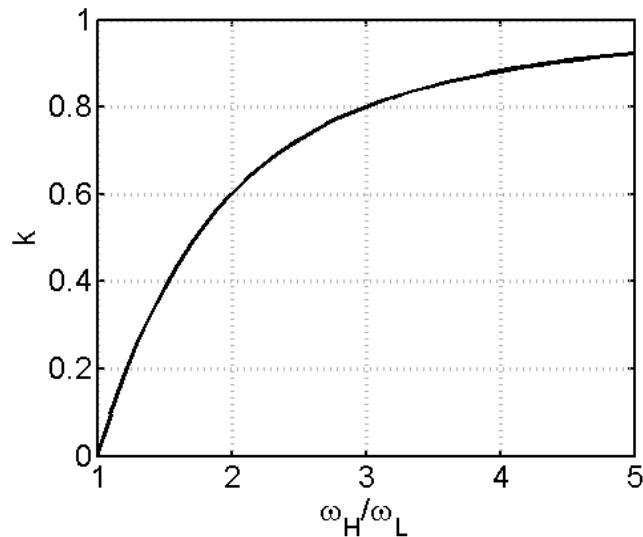


Figure 5.9. Upper bound of the coupling coefficient,  $k$ , vs. the frequency ratio,  $\omega_H/\omega_L$ .

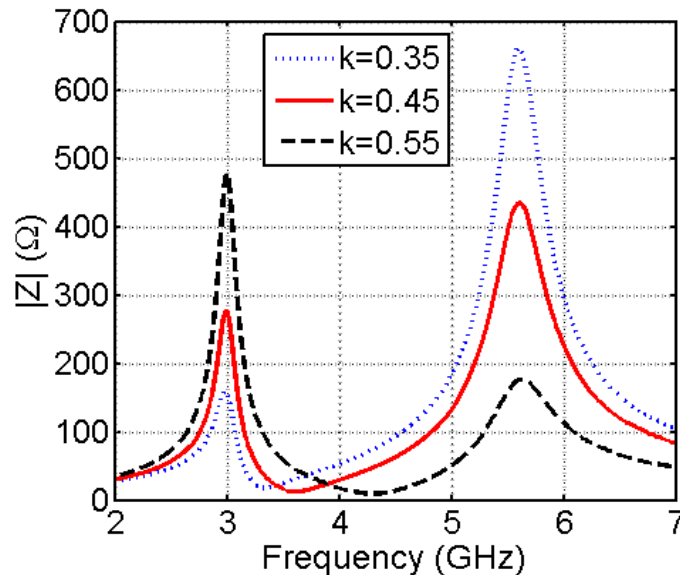


Figure 5.10. Impedance of the tank with resonant frequencies of  $\omega_L = 2\pi \cdot 3$  GHz,  $\omega_H = 2\pi \cdot 5.6$  GHz for various coupling coefficients,  $k$ , for the configuration of  $L_1 = 1.7$  nH,  $R_1 = 3.5$   $\Omega$ ,  $L_2 = 3.4$  nH, and  $R_2 = 3.8$   $\Omega$ .

### 5.3 Circuit Details and Experimental Results

The circuit of Fig. 5.5 together with a differential open drain buffer was implemented in CMOS 0.13  $\mu\text{m}$  technology. The main focus of this design is to achieve triple-mode operation, especially the concurrent dual oscillation mode, with the control of the biasing currents. In order to investigate the circuit flexibly after fabrication, the two biasing currents are tuned externally through two current mirrors. The biasing voltage,  $V_b$ , is also controlled externally for investigating its effect on the triple-mode operation. Since a wide tuning range is not the main scope, each variable capacitor was only implemented using a varactor and a switched capacitor to simplify the design. Thus only limited tuning range is achieved, which would be seen later from the measurement results. But, the tuning range could be improved by using more switched capacitors.

As discussed in Section 5.2.3,  $k$  of 0.35-0.55 is desired in the design of an oscillator in 3-and 5- GHz bands.  $k$  of 0.45 is chosen and a transformer with concentric structure is used. The method of designing a multi-tap transformer [37] is adopted in the design of the concentric transformer. With the targeted inductance of  $L_1= 1.7$  nH and  $L_2= 3.4$  nH and consideration of area and quality factor, the final realized 4-port concentric transformer with center-taps is realized with 3x3 turns, metal with of 8.4  $\mu\text{m}$ , metal spacing of 5  $\mu\text{m}$ , and outer diameter of 270  $\mu\text{m}$ . The spacing between the primary and secondary inductor is 9.5  $\mu\text{m}$ . Top two metals connected in parallel are used for good quality factor. Broadband lumped element model of the transformer using  $\Pi$ -networks is developed to enable both time-domain and frequency domain simulation [37].

The extracted self-inductance, quality factor, and coupling coefficient from the Momentum EM simulation results using the transformer layout and the developed broadband

lumped element model are shown in Fig. 5.11. The primary windings exhibits lower Q than the secondary winding.

The fabricated dual-coupled triple mode VCO is shown in Fig. 12, and occupies an area of 0.93 mm x 0.8 mm, including pads. The core area of the oscillator is 0.54 mm x 0.3 mm. The VCO was characterized with Tektronix RSA 6114A spectrum analyzer with phase noise option via wafer probing the differential outputs of the buffer, which were biased using two Bias-Tees and were converted to a single-ended output using an external hybrid-coupler. Direct measurement results are reported in the paper to be consistent with the screen captures

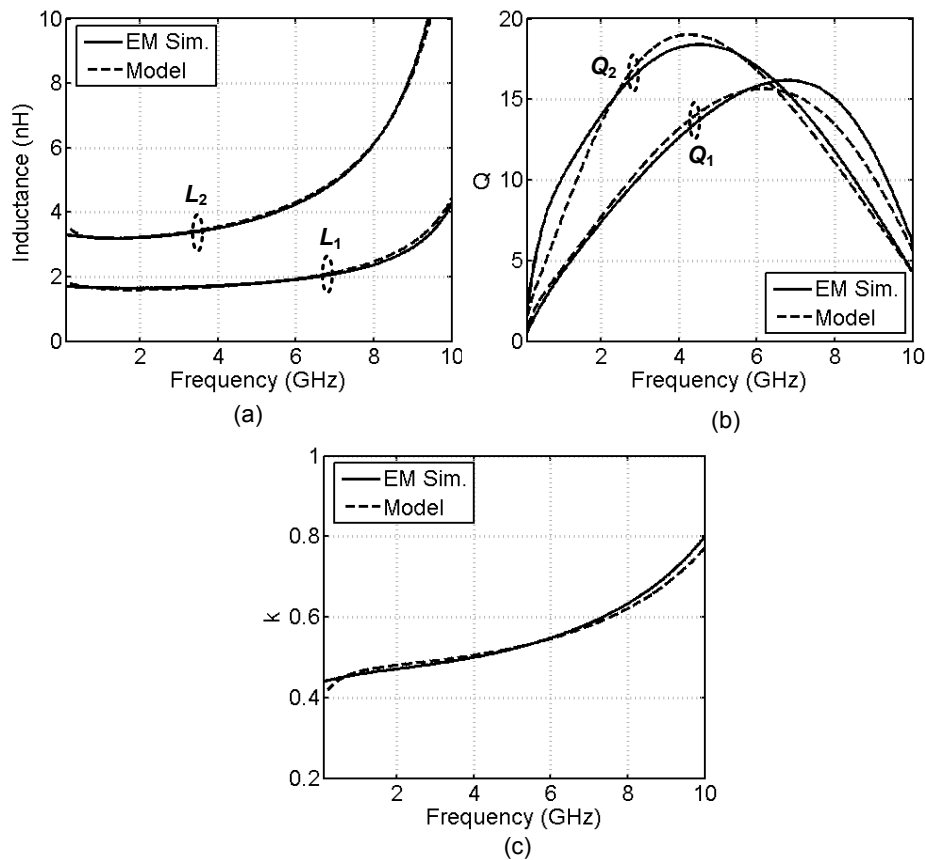


Figure 5.11. The extract (a) The self-inductance, (b) quality factor, and (c) coupling coefficient from the EM simulation and the lumped-element model.

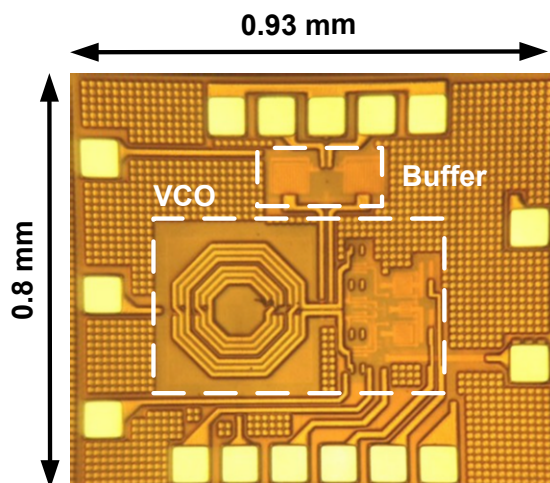


Figure 5.12. Microphotograph of the dual-coupled triple mode VCO.

of the Spectrum analyzer. The VCO including the buffer dissipates a total of 17.4 mW from a 1.2-V supply, while only 5.4 mW is dissipated by the VCO core.

The VCO is configured to mode 1, the single oscillation mode in the 5 GHz band, when  $I_{t1}$  is set to turn on  $M_1$  and  $M_2$ , generating enough  $gm_1$  to compensate the loss at the high frequency band, while  $M_3$  and  $M_4$  are turned off, making  $gm_2=0$ , by disabling the current source  $I_2$ . In practice,  $V_b$  is shorted to ground in order to completely turn off  $M_3$  and  $M_4$  because they could be turned on part of the time when the oscillation amplitude is large while  $V_b$  is kept at 1.2 V. If  $M_3$  and  $M_4$  are still turned on partly,  $gm_2$  is generated and it increases as the oscillation amplitude becomes larger, which would degrade the performance in mode 1 because it appears as positive impedance in the high frequency band. A more significant problem is that a small value of  $gm_2$  could increase the impedance of the tank in the low frequency band, as seen in Fig. 5.8 (a). Though  $gm_2$  is small, it would still large enough to induce concurrent dual oscillation. Then the VCO will eventually operate in mode 3. To avoid the potential concurrent dual oscillation,  $V_b$  is shorted to ground in mode 1. Fig. 5.13(a)

shows a measured output spectrum from 1 to 7 GHz in mode 1 when  $I_{t1} = 4.5$  mA,  $I_{t2} = 0$ , and  $V_b = 0$ . The oscillator oscillates at 5.25 GHz with power of -8.23 dBm.

The VCO is configured to mode 2, the single oscillation mode in the 3 GHz band, when  $V_b$  is biased at 1.2 V and  $I_{t2}$  is set to turn on  $M_3$  and  $M_4$ , generating enough  $g_{m2}$  to compensate the loss at low frequency band and increase the loss at the high frequency band, while  $M_1$  and  $M_2$  are turned off, making  $g_{m1} = 0$ , by disabling the current source  $I_{t1}$ . Though

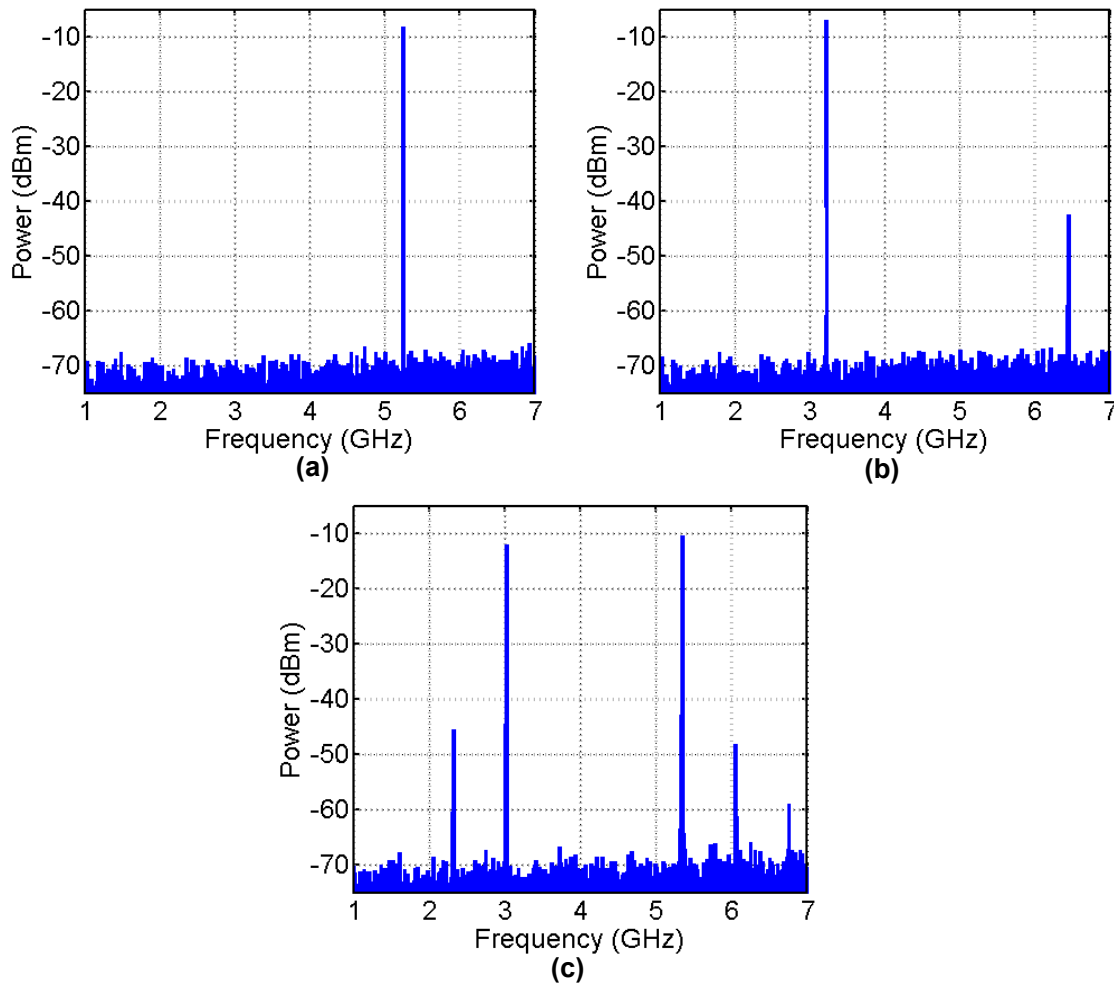


Figure 5.13. Measured output spectrum of (a) mode 1, single oscillation in high band, (b) mode 2, single oscillation in low band, and (c) mode 3, concurrent dual oscillation in both low and high band.

$M_1$  and  $M_2$  are not completely turned off when the oscillation amplitude is large, the start-up condition at the high frequency band could not be met because of the significant loss introduced by  $gm_2$  to the high frequency band. Thus, concurrent dual oscillation could not occur so long as  $gm_2$  is large, which is the case of mode 2. Fig. 5.13 (b) shows a measured output spectrum from 1 to 7 GHz in mode 2 when  $I_{t1} = 0$ ,  $I_{t2} = 4.5$  mA, and  $V_b = 1.2$ . The oscillator oscillates at 3.22 GHz with power of -7.04 dBm.

The VCO is configured to mode 3, the concurrent dual oscillation mode in both the 3- and 5 GHz band, when  $I_{t1}$  is set to turn on  $M_1$  and  $M_2$ , generating enough  $gm_1$  to compensate the loss at both bands, while  $V_b$  is biased at 1.2 V and  $I_{t2}$  is tuned to adjust the generated  $gm_2$  by  $M_3$  and  $M_4$  such that the impedance at both bands are close to each other and may be compensated with a similar value of  $gm_1$ . It is worth to mention that  $gm_2$  may be also tuned by controlling the biasing level of  $V_b$ . Fig. 5.13 (c) shows a measured output spectrum from 1 to 7 GHz in mode 3 when  $I_{t1} = 4.3$  mA,  $I_{t2} = 0.2$  mA, and  $V_b = 1.2$ . The oscillator oscillates both at 3.03- and 5.34 GHz with power of -11.95 and -10.5 dBm, respectively. The output power at each frequency is on average 3 dB less than that that in mode 1 and 2, while the total output power is the same, which is primarily determined on the total biasing current.

The tuning range is also tested for the three modes with fixed DC conditions that  $I_{t1} = 4.5$  mA,  $I_{t2} = 0$ , and  $V_b = 0$  in mode 1,  $I_{t1} = 0$ ,  $I_{t2} = 4.5$  mA, and  $V_b = 1.2$  V in mode 2, and  $I_{t1} = 4.3$  mA,  $I_{t2} = 0.2$  mA, and  $V_b = 1.2$  V in mode 3. The oscillation frequency may be tuned by  $V_{t1}$  and  $V_{t2}$ , controlling the capacitance of the varactors, and by switching in-and-out a pair of switched capacitors. Fig. 14 illustrates the measured oscillation frequency ranges in the three modes. In mode 1, the oscillation frequency is in the range of 4.83 ~ 5.28 GHz, shown in Fig. 5.14 (a), resulting in tuning range of 8.9%. It needs to be mention that  $V_{t2}$  is not tuned and is

set at 0 because  $V_b$  is 0 V and the varactor should be reverse biased. In mode 2, the oscillation frequency is in the range of 2.76 ~ 3.22 GHz, shown in Fig. 5.14 (b), resulting in tuning range of 15.6%. Fig. 5.14 (c) shows the oscillation frequency range in mode 3 when only effective concurrent dual oscillation is counted, where the signal power at both oscillation frequencies is larger than -16 dBm. The oscillation frequency is in the range of 4.8 ~ 5.42 GHz for the high frequency band, corresponding to tuning range of 12%, and is in the

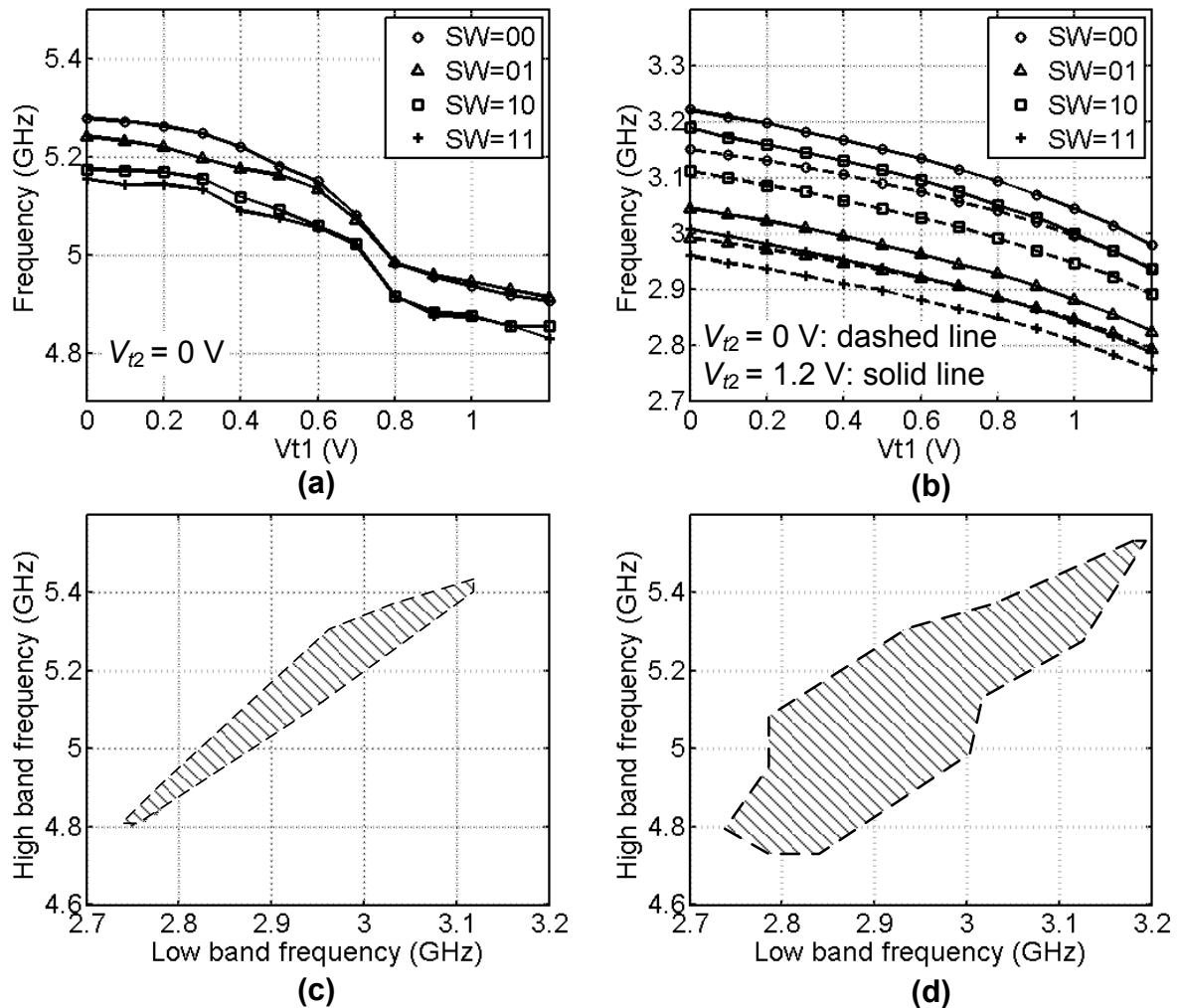


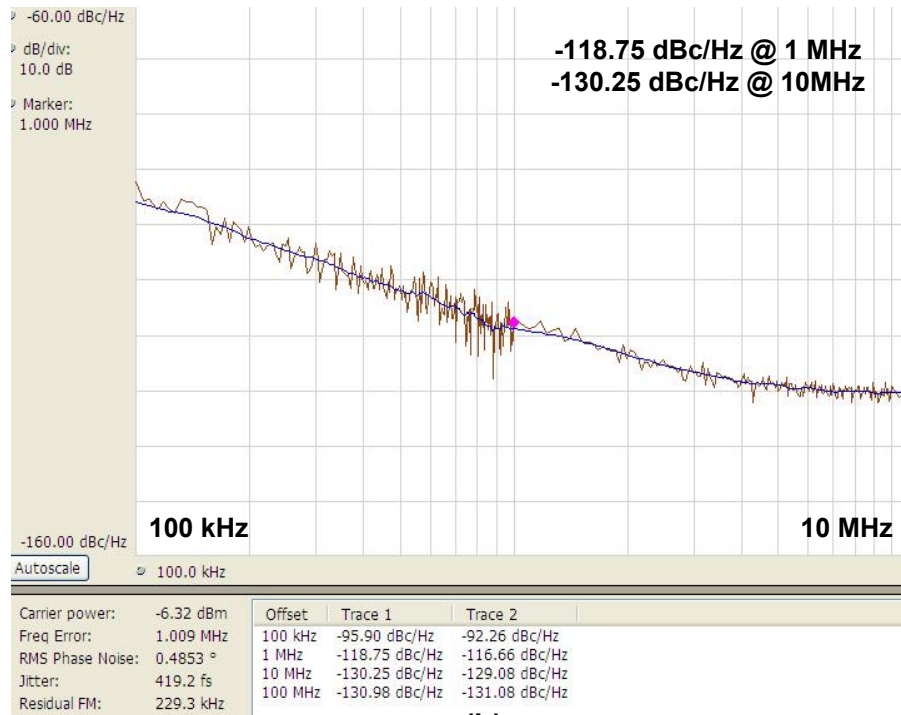
Figure 5.14. Measured tuning range of (a) mode 1 ( $V_{t2}=0$ ), (b) mode 2 ( $V_{t2}=0$ : dashed line and  $V_{t2}=1.2$  V: solid line), and (c) mode 3 for fixed  $I_2=0.2$  mA, (d) mode 3 for tunable  $I_2$ .

range of 2.74 ~ 3.11 GHz for the low frequency band, corresponding to tuning range of 13%. The effective concurrent dual oscillation frequency range, shown as the shaded area in Fig. 12 (c), is only a small portion of the paired frequencies between 4.8 GHz and 5.42 GHz in the high frequency band and between 2.74 GHz and 3.11 GHz in the low frequency band. The frequency ratio of the high and low oscillation frequencies is in the range of 1.73 ~ 1.78. But, concurrent dual oscillation can be actually observed in a wider frequency range when the biasing current  $I_{t2}$  is tuned to adjust the signal power at the two concurrent oscillation frequencies, shown in Fig. 5.14 (d). When the power of the high band signal is much lower than that of the low band signal,  $I_{t2}$  is reduced, while when the power of the low band signal is much lower than that of the high band signal,  $I_{t2}$  is increased.

The phase noise is measured with the same DC conditions as in the tuning range test. Fig 5.15 shows the measured phase noise in the range of 100 kHz ~ 10 MHz offset from the carrier frequency of 5.24 and 3.22 GHz in mode 1 and 2, respectively. The carrier power is -8.8 and -6.3 dBm, respectively. The measured phase noise is -109.5 and -118.8 dBc/Hz at 1 MHz offset, respectively, and -125.5 and -130.3 dBc/Hz at 10 MHz offset, respectively. It is seen that the phase noise in mode 1 is lower than that in mode 2. That is primary due to lower tank quality factor in the low frequency band than that in the high frequency band. The smaller different at 10 MHz offset than at 1 MHz is due to higher noise floor in the measurement. The phase noise in mode 3 is measured at carrier frequency of 5.34 and 3.03 GHz in the high band and low band, respectively. The carrier power is -11.8 and -10.2 dBm, respectively. The phase noise is -104.3 and -112.6 dBc/Hz at 1 MHz offset, and -121.6 and -128.5 dBc/Hz at 10 MHz offset, respectively. Similar to mode 1 and 2, the phase noise at high frequency band is about 8~9 dB higher than that in low frequency band at 1 MHz offset,



(a)



(b)

Figure 5.15. Measured phase noise of (a) mode 1, single oscillation in high band, (b) mode 2, single oscillation in low band.

and is about 5~7 dB higher at 10 MHz offset. The phase noise in mode 3 is about 4~5 dB higher than that in the corresponding band of mode 1 and 2 at 1 MHz offset and about 2~4 dB higher at 10 MHz offset. That is in part due to the 3 dB lower of the carrier power in the mode 3 than that in mode 1 and 2. The smaller different at 10 MHz offset than at 1 MHz is due to the higher noise floor in the measurement.

The measured phase noise in mode 3 is further compared with the simulated phase noise, shown in Fig. 16. It is seen that measured curve is roughly agree with simulated one. It needs to be mentioned that two ideal band pass filters (BPF) are used in the simulation of the phase noise in mode 3 because the current commercial circuit simulators, such as SpectreRF and the ADS harmonic-balance simulator, could not simulate the phase noise of a dual-frequency oscillator. After the BPFs, two individual sinusoidal signals are obtained and the commercial circuit simulators can be used to simulate the phase noise of the individual

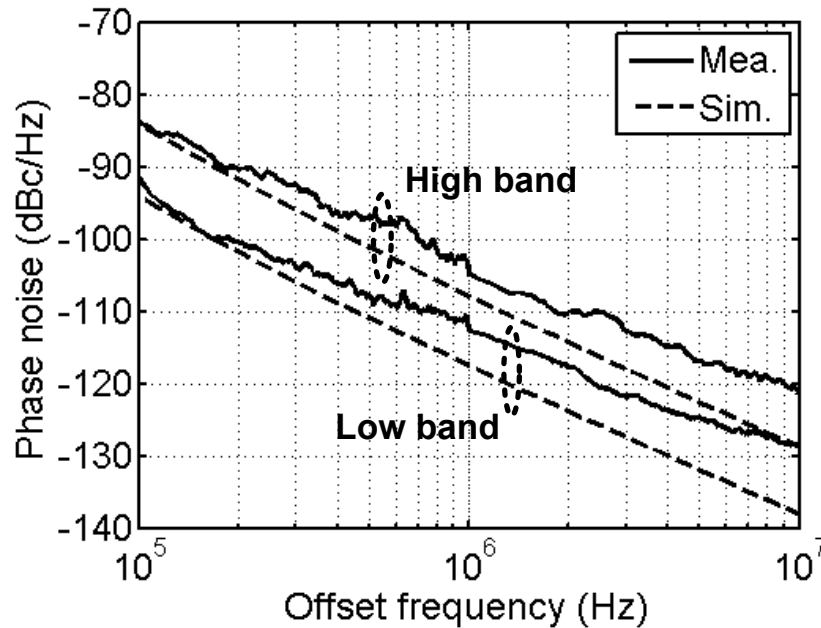


Figure 5.16. Measured and simulated phase noise in mode 3.

sinusoidal signals. The transient waveforms at the output of the buffer of the oscillator and the two BPFs are shown in Fig. 5.17 (a)-(c), respectively.

Table 5.2 compares the performance of the proposed VCO against the recently reported concurrent dual oscillation VCO. The figure of merit (FoM) in the table is defined as:

$$FoM = 10 \log \left( \left( \frac{f_o}{\Delta f} \right)^2 \frac{1}{L(\Delta f) \times P_{diss}} \right). \quad (5-30)$$

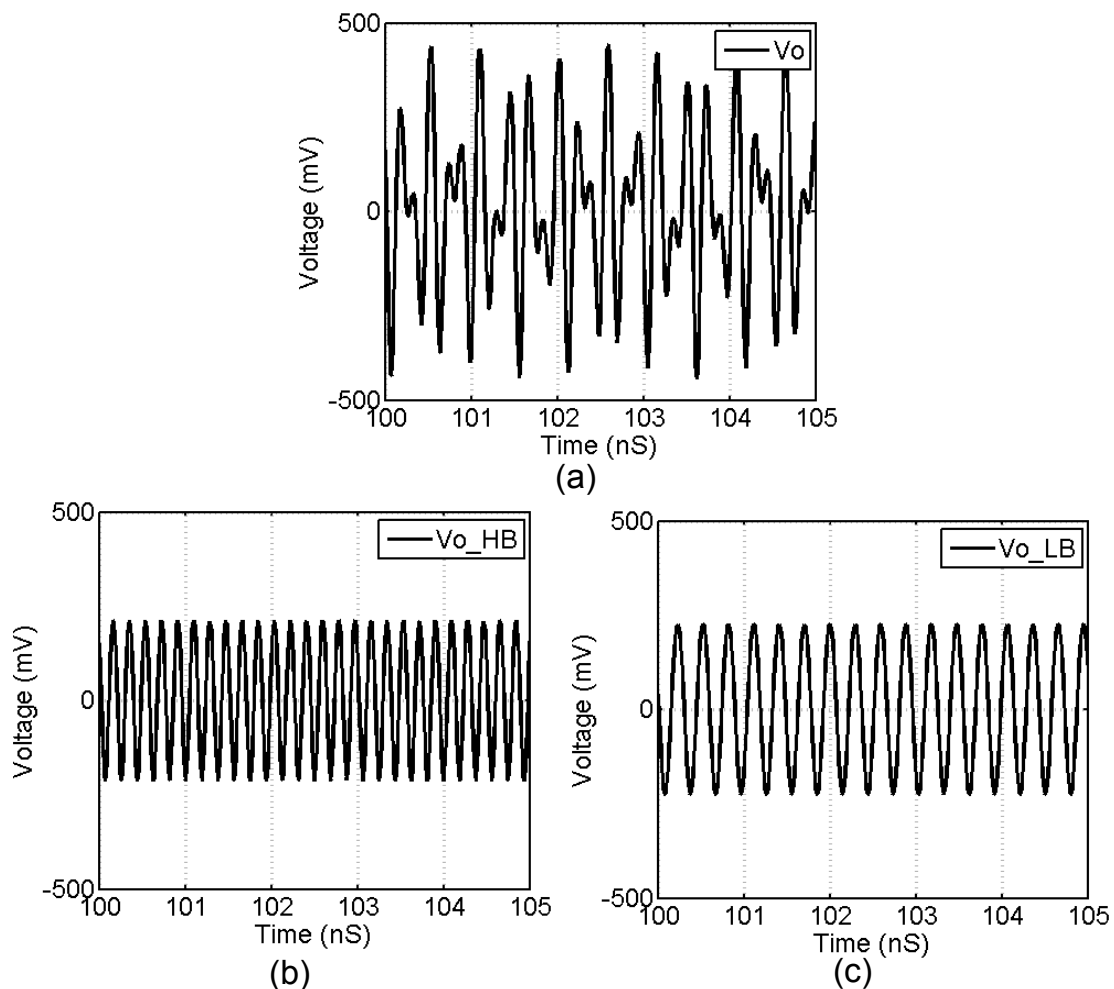


Figure 5.17. Simulated transient waveform of mode 3 (a) the differential output, (b) the output filtered by an ideal BPF centered at 5.3 GHz, and (c) the output filtered by an ideal BPF centered at 3.45 GHz.

where is  $\mathcal{L}(\Delta f)$  the phase noise at  $\Delta f$ , and  $P_{diss}$  is the power consumption in mW. The FoM with tuning range (FoM<sub>T</sub>) is given as:

$$FoM_T = FOM + 10 \log \left( \frac{TR (\%)}{10} \right). \quad (5-31)$$

The FoM of the proposed oscillator is calculated to be 177, 182, and 176/172 dB for the three modes, respectively. The FoM<sub>T</sub> is calculated to be 176, 186, and 178/173, respectively for the three modes. In the calculation of the concurrent mode FoM, the power in each band is both assumed half of the total power. The proposed VCO exhibits better performance than the concurrent oscillator in [22]. Comparing to [23], the performance is comparable in the low frequency band, but is worse in the high frequency band. That is mainly because of the low tank quality factor of the designed oscillator in the high frequency band, which can be improved with a more optimized transformer design. The FoM and FoM<sub>T</sub> is higher in [23] is partly because of the reduced current consumption with more advanced CMOS technology. Its large tuning range is because of the use of a large number of switched capacitor tanks. However, only a pair of switched capacitors is used for primary and secondary tank in the designed VCO. The tuning range of the proposed VCO can be improved by adopting more switched capacitors. Besides the switched capacitors, the tuning range in mode 1 may be extended by using bias circuitry for the varactors in the secondary tank so that it can still be tuned even when  $V_b=0$ . Though the overall performance is not better than the work reported in [23],  $V_b$  in the proposed VCO may be biased up to  $V_{DD}$  for concurrent oscillation. For a simplified design of a concurrent dual- oscillator,  $V_b$  may be directed connected to the supply voltage and balanced oscillation amplitude is achieved by tuning the tail current,  $V_{I2}$ .

Table 5.2. Summary of VCO performance and comparison to previously published designs

Ref	[22]	[23]			This work		
Type	Concurrent dual band	Dual band and concurrent dual band			Dual band and concurrent dual band		
		High band	Low band	Concurrent dual band	High band (mode 1)	Low band (mode 2)	Concurrent dual band (mode 3)
Tech.	0.18 $\mu\text{m}$ SiGe BiCMOS	65 nm CMOS			0.13 $\mu\text{m}$ CMOS		
Area ( $\text{mm}^2$ )	1.2	0.23*			0.74 (0.16*)		
$V_{DD}$ (V)	2	1.2			1.2		
Current (mA)	17.5	1.43	0.75	1.6	4.5		
Freq. (GHz)	2.23/4.98	9.53	5.44	5.15/9.28	5.24	3.22	3.03/5.34
Tuning range (%)	12.5/10.3	23.2	33.7	34.7/22.8	8.9	15.6	12.1/12.8
Phase noise (dBc/Hz)	-109/-103 @1MHz	-127.54 @10MHz	-131.08 @10MHz	-129.94/ -127.68 @10MHz	-109.5 @1MHz	-118.8 @1MHz	-112.6/-104.3 @1MHz
					-125.5 @10MHz	-130.6 @10 MHz	-128.5/-121.6 @10MHz
FoM (dB)	164/165	185	186	184/187	177	182	176/172
FoM <sub>T</sub> (dB)	166/165	192	197	195/194	176	186	178/173

\* Excluding pads

## 5.4 Summary

A transformer-based dual-coupled triple mode VCO is proposed and fabricated in 0.13  $\mu\text{m}$  CMOS. The VCO is able to generate a single frequency in the 3 and 5 GHz bands, respectively, as well as two frequencies in the 3- and 5 GHz bands simultaneously. The triple mode operation is realized with a transformer-based 4<sup>th</sup> order tank with tunable transconductance feedback between the primary and secondary coils and is flexibly reconfigured by controlling the bias current. The VCO achieves phase noise of -109.5, -118.8, and -112.6/-104.3 dBc/Hz at 1 MHz offset when the oscillator oscillates at 5.24 GHz, 3.22 GHz, and 3.03/5.34 GHz, respectively. The turning range is 8.9%, 15.6%, and 12.1/12.8% in the three modes, respectively. The VCO core occupies an area of  $0.54 \times 0.3 \text{ mm}^2$ , and has a power dissipation of 5.4 mW from a 1.2 V supply. It provides a compact and flexibly tuned frequency generator solution for soft-ware defined radios supporting concurrent intra-band receptions.

## CHAPTER 6. CONCLUSIONS

### 6.1 Contributions

This research investigates two building blocks in the multi-band multi-standard SDR receiver capable of concurrent reception, the LNA and the VCO, utilizing transformer-based series and parallel resonators.

Transformers, however, are not provided by the foundry in the product design kit (PDK) and must be designed and modeled first before adopted in the circuit design. To facilitate the design cycles, a design method of a multi-tap transformer, applicable to conventional transformers, is outlined. A broadband lumped model is also proposed. The design methods and broadband model were verified with the implemented multi-tap transformers in 0.13  $\mu\text{m}$  CMOS.

A reconfigurable multi-mode input matching network of a LNA utilizing an asymmetric multi-tap transformer is then proposed. The matching network is analyzed in details regarding the parameters of the multi-tap transformer. Based on the analysis, a design strategy is outlined. Noise analysis is also provided. The multi-mode LNA was prototyped in 0.13  $\mu\text{m}$  CMOS and achieves comparable performance with state-of-art narrow-band, concurrent-dual band, and wideband LNAs, while supporting all three types of operation.

Finally, a dual-feedback triple-mode VCO is presented, generating two frequencies either concurrently or one at a time. The VCO features a transformer-based high order tank with its impedance tuned by feedback transconductance cells between the primary and

secondary inductor. Three operation modes are realized by tuning the transconductance. The oscillation frequency, start-up condition, and oscillation amplitude are analyzed for each operation mode. The triple mode VCO was prototyped in 0.13  $\mu\text{m}$  CMOS and achieves a FOM comparable with state-of-art VCOs.

## 6.2 Future Work

While this research prototype a multi-mode LNA and a triple-mode VCO supporting concurrent reception, there are various fields that need further study in order to implement a fully integrated SDR receiver supporting carrier aggregation. For example, system level frequency plan and the nonlinearities of the LNA and mixer must be re-studied to minimize the interference among the simultaneously received signals because the number of harmonics and intermodulation signals increases substantially. Besides, it will become much more complicated when taking the concurrent resonant VCO into account since there are as well a significant number of harmonics and cross-modulation signals from the VCO.

To support the popular quadrature operation, a quadrature version of the triple mode VCO is needed. A dual-loop PLL is also needed to precisely control the frequencies when the VCO operates in the concurrent dual-resonant mode. A possible solution is to use a conventional PLL and include a bandpass filter after the frequency divider to separate the two frequencies. Only very little extra current consumption is expected in the bandpass filter because it operates at very low frequency.

This dissertation investigates multi-tap transformers in details for the first time and adopts it into the design of a LNA. There are various opportunities for future research in the application of multi-tap transformers in various RF circuits besides the LNA. For example, a

multi-tap transformer may be used in the matching network and power combining circuitry of a power amplifier. A multi-tap transformer may also be used to provide flexible feedbacks in a broad range of RF circuits that have adopted reactive feedbacks..

## BIBLIOGRAPHY

- [1] A. A. Abidi, "The path to the software-defined radio receiver," *IEEE J. Solid-State Circuits*, vol. 42, no. 5, pp. 954-966, May 2007.
- [2] "Evolved Universal Terrestrial Radio Access (E-UTRA); User Equipment (UE) Radio Transmission And Reception," *3GPP, 3rd Generation Partnership Project (3GPP)*. TR 36.101, 2012.
- [3] R. Bagheri, A. Mirzaei, S. Chehrazi, M. E. Heidari, M. Lee, M. Mikhemar, W. Tang, and A. A. Abidi, "An 800-MHz-6-GHz software-defined wireless receiver in 90-nm CMOS," *IEEE J. Solid-State Circuits*, vol. 41, no. 12, pp. 2860-2876, Dec. 2006.
- [4] M. T. Reihha and J. R. Long, "A 1.2 V reactive-feedback 3.1-10.6 GHz low-noise amplifier in 0.13 um CMOS," *IEEE J. Solid-State Circuits*, vol. 42, no. 5, pp. 1023-1033, May 2007.
- [5] R.-F. Ye, T.-S. Horng, and J.-M. Wu, "Wideband common-gate low-noise amplifier with dual-feedback for simultaneous input and noise matching," in *Proc. IEEE Radio Freq. Integr. Circuits (RFIC) Symp.*, 2011, pp. 1-4.
- [6] Z. Ru, N. A. Moseley, E. A. M. Klumperink, and B. Nauta, "Digitally enhanced software-defined radio receiver robust to out-of-band interference," *IEEE J. Solid-State Circuits*, vol. 44, no. 12, pp. 3359-3375, Dec 2009.
- [7] J. Borremans, G. Mandal, V. Giannini, B. Debaillie, M. Ingels, T. Sano, B. Verbruggen, and J. Craninckx, "A 40 nm CMOS 0.4-6 GHz receiver resilient to out-of-band blockers," *IEEE J. Solid-State Circuits*, vol. 46, no. 7, pp. 1659-1671, Jul 2011.
- [8] M. El-Nozahi, E. Sanchez-Sinencio, and K. Entesari, "A CMOS low-noise amplifier with reconfigurable input matching network," *IEEE Trans. Microw. Theory Tech.*, vol. 57, no. 5, pp. 1054-1062, May 2009.
- [9] H. Hashemi and A. Hajimiri, "Concurrent multiband low-noise amplifiers-theory, design, and applications," *IEEE Trans. Microw. Theory Tech.*, vol. 50, no. 1, pp. 288-301, Jan 2002.
- [10] N. M. Neihart, J. Brown, and X. Yu, "A dual-band 2.45/6 GHz CMOS LNA utilizing a dual-resonant transformer-based matching network," *IEEE Trans. Circuits Syst. I, Reg. Papers*, vol. 59, no. 8, pp. 1743-1751, Aug. 2012.
- [11] B. Razavi, *RF Microelectronics*: Prentice Hall, 1998.

- [12] Y. Seong-Mo and K. K. O, "Switched resonators and their applications in a dual-band monolithic CMOS LC-tuned VCO," *IEEE Trans. Microw. Theory Tech.*, vol. 54, no. 1, pp. 74-81, 2006.
- [13] A. Tanabe, K. Hijioka, H. Nagase, and Y. Hayashi, "A novel variable inductor using a bridge circuit and its application to a 5-20 GHz tunable LC-VCO," *IEEE J. Solid-State Circuits*, vol. 46, no. 4, pp. 883-893, Apr. 2011.
- [14] J. Borremans, A. Bevilacqua, S. Bronckers, M. Dehan, M. Kuijk, P. Wambacq, and J. Craninckx, "A compact wideband front-end using a single-inductor dual-band VCO in 90 nm digital CMOS," *IEEE J. Solid-State Circuits*, vol. 43, no. 12, pp. 2693-2705, Dec. 2008.
- [15] G. Li and E. Afshari, "A distributed dual-band LC oscillator based on mode switching," *IEEE Trans. Microw. Theory Tech.*, vol. 59, no. 1, pp. 99-107, Jan. 2011.
- [16] G. Li, L. Liu, Y. Tang, and E. Afshari, "A low-phase-noise wide-tuning-range oscillator based on resonant mode switching," *IEEE J. Solid-State Circuits*, vol. 47, no. 6, pp. 1295-1308, Jun 2012.
- [17] Z. Safarian and H. Hashemi, "Wideband multi-mode CMOS VCO design using coupled inductors," *IEEE Trans. Circuits Syst. I, Reg. Papers*, vol. 56, no. 8, pp. 1830-1843, Aug. 2009.
- [18] S. Rong and H. C. Luong, "Analysis and design of transformer-based dual-band VCO for software-defined radios," *IEEE Trans. Circuits Syst. I, Reg. Papers*, vol. 59, no. 3, pp. 449-462, Mar. 2012.
- [19] M. Demirkan, S. P. Bruss, and R. R. Spencer, "Design of wide tuning-range CMOS VCOs using switched coupled-inductors," *IEEE J. Solid-State Circuits*, vol. 43, no. 5, pp. 1156-1163, Nov. 2008.
- [20] G. Cusmai, M. Reposi, G. Albasini, A. Mazzanti, and F. Svelto, "A magnetically tuned quadrature oscillator," *IEEE J. Solid-State Circuits*, vol. 42, no. 12, pp. 2870-2877, Dec. 2007.
- [21] U. L. Rohde and A. K. Poddar, "Reconfigurable concurrent oscillators for multi-band multi-mode wireless communication systems," in *IEEE Sarnoff Symp.*, 2007, pp. 1-6.
- [22] A. Goel and H. Hashemi, "Concurrent dual-frequency oscillators and phase-locked loops," *IEEE Trans. Microw. Theory Tech.*, vol. 56, no. 8, pp. 1846-1860, Aug. 2008.
- [23] A. Li and H. C. Luong, "A reconfigurable 4.7-6.6GHz and 8.5-10.7GHz concurrent and dual-band oscillator in 65nm CMOS," in *Proc. IEEE Radio Freq. Integr. Circuits (RFIC) Symp.*, 2012, pp. 523-526.

- [24] S. J. Yun, N. D. B. Yen, I. Lee, J. T. Lee, and S. G. Lee, "A differentially-tuned voltage controlled oscillator using symmetric transformer," *IEEE Microw. Wireless Components Letters*, vol. 18, no. 7, pp. 464-466, Jul 2008.
- [25] S. Saberi and J. Paramesh, "A 11.5-22 GHz dual-resonance transformer-coupled quadrature VCO," in *Proc. IEEE Radio Freq. Integr. Circuits (RFIC) Symp.*, 2011, pp. 1-4.
- [26] D. H. Shin, J. Park, and P. Yue, "A low-power, 3-5-GHz CMOS UWB LNA using transformer matching technique," in *Proc. IEEE Asian Solid-State Circuits Conf. (A-SSCC)*, 2007, pp. 95-98.
- [27] N. M. Neihart, D. J. Allstot, M. Miller, and P. Rakers, "Twisted transformers for low coupling RF and mixed signal applications," in *Proc. IEEE Int. Symp. Circuits Syst. (ISCAS)*, 2009, pp. 429-432.
- [28] J. R. Long, "Monolithic transformers for silicon RF IC design," *IEEE J. Solid-State Circuits*, vol. 35, no. 9, pp. 1368-1382, Sep. 2000.
- [29] N. T. Tchamov, S. S. Broussev, I. S. Uzunov, and K. K. Rantala, "Dual-band LC VCO architecture with a fourth-order resonator," *IEEE Trans. Circuits Syst. II: Exp. Briefs*, vol. 54, no. 3, pp. 277-281, Mar 2007.
- [30] A. Goel and H. Hashemi, "Frequency switching in dual-resonance oscillators," *IEEE J. Solid-State Circuits*, vol. 42, no. 3, pp. 571-582, Mar. 2007.
- [31] J. L. Brown and N. M. Neihart, "An analytical study of a magnetically tuned matching network," in *Proc. IEEE Int. Symp. Circuits Syst. (ISCAS)*, 2012, pp. 1979-1982.
- [32] X. Yu and N. M. Neihart, "Analysis and design of a reconfigurable multimode low-noise amplifier utilizing a multitap transformer," *IEEE Trans. Microw. Theory Tech.*, vol. 61, no. 3, pp. 1236-1246, Mar. 2013.
- [33] B. Georgescu, H. Pekau, J. Haslett, and J. McRory, "Tunable coupled inductor Q-enhancement for parallel resonant LC tanks," *IEEE Trans. Circuits Syst. II: Exp. Briefs*, vol. 50, no. 10, pp. 705-713, Oct. 2003.
- [34] T. Soorapanth and S. S. Wong, "A 0-dB IL 2140 $\pm$ 30 MHz bandpass filter utilizing Q-enhanced spiral inductors in standard CMOS," *IEEE J. Solid-State Circuits*, vol. 37, no. 5, pp. 579-586, May 2002.
- [35] B. Catli and M. M. Hella, "A 1.94 to 2.55 GHz, 3.6 to 4.77 GHz tunable CMOS VCO based on double-tuned, double-driven coupled resonators," *IEEE J. Solid-State Circuits*, vol. 44, no. 9, pp. 2463-2477, Sep. 2009.

- [36] D. Hauspie, E.-C. Park, and J. Craninckx, "Wideband VCO with simultaneous switching of frequency band, active core, and varactor size," *IEEE J. Solid-State Circuits*, vol. 42, no. 7, pp. 1472-1480, Jul. 2007.
- [37] X. Yu and N. M. Neihart, "Design and characterization of symmetric multi-tap transformers," in *Proc. IEEE Int. Symp. Circuits Syst. (ISCAS)*, 2012, pp. 954-957.
- [38] C.-T. Fu, C.-L. Ko, C.-N. Kuo, and Y.-Z. Juang, "A 2.4-5.4-GHz wide tuning-range CMOS reconfigurable low-noise amplifier," *IEEE Trans. Microw. Theory Tech.*, vol. 56, no. 12, pp. 2754-2763, Dec. 2008.
- [39] T. Ito, K. Okada, and K. Masu, "Characterization of on-chip multi-port inductors for small-area RF circuits," *IEEE Trans. Circuits Syst. I, Reg. Papers*, vol. 56, no. 8, pp. 1590-1597, Aug. 2009.
- [40] I. Bhatti, R. Roufoogaran, and J. Castaneda, "A fully integrated transformer-based front-end architecture for wireless transceivers," in *ISSCC Dig. Tech. Papers*, 2005, pp. 106-107.
- [41] X. Yu and N. M. Neihart, "Integrated multi-tap transformer for reconfigurable multimode matching networks," in *Proc. IEEE Int. Symp. Circuits Syst. (ISCAS)*, 2011, pp. 1395-1398.
- [42] Y. Cao, R. A. Groves, X. J. Huang, N. D. Zamdmer, J. O. Plouchart, R. A. Wachnik, T. J. King, and C. M. Hu, "Frequency-independent equivalent-circuit model for on-chip spiral inductors," *IEEE J. Solid-State Circuits*, vol. 38, no. 3, pp. 419-426, Mar 2003.
- [43] O. El-Gharniti, E. Kerherve, and J. B. Begueret, "Modeling and Characterization of on-chip transformers for silicon RFIC," *IEEE Trans. Microw. Theory Tech.*, vol. 55, no. 4, pp. 607-615, Apr. 2007.
- [44] F. Rotella, B. K. Bhattacharya, V. Blaschke, M. Matloubian, A. Brotman, Y. Cheng, R. Divecha, D. Howard, K. Lampaert, P. Miliozzi, M. Racanelli, P. Singh, and P. J. Zampardi, "A broad-band lumped element analytic model incorporating skin effect and substrate loss for inductors and inductor like components for silicon technology performance assessment and RFIC design," *IEEE Trans. Electron Devices*, vol. 52, no. 7, pp. 1429-1441, Jul. 2005.
- [45] J. S. Walling and D. J. Allstot, "Monolithic spiral transformers: a design methodology," in *Proc. IEEE Int. Symp. Circuits Syst. (ISCAS)*, 2007, pp. 3351-3354.
- [46] F. W. Grover, *Inductance Calculations: Working formulas and Tables*, 1 ed. ed. New York: D. Van Nostrand Company, Inc., 1946.

- [47] S.-M. Yim and K. K. O, "Switched resonators and their applications in a dual-band monolithic CMOS LC-tuned VCO," *IEEE Trans. Microw. Theory Tech.*, vol. 54, no. 1, pp. 74-81, Jan. 2006.
- [48] X. Yu and N. M. Neihart, "A 2-11 GHz reconfigurable multi-mode LNA in 0.13 $\mu$ m CMOS," in *Proc. IEEE Radio Freq. Integr. Circuits (RFIC) Symp.*, 2012, pp. 475-478.
- [49] T. K. Nguyen, C. H. Kim, G. J. Ihm, M. S. Yang, and S. G. Lee, "CMOS low-noise amplifier design optimization techniques," *IEEE Trans. Microw. Theory Tech.*, vol. 52, no. 5, pp. 1433-1442, May 2004.
- [50] D. K. Shaeffer and T. H. Lee, "A 1.5-V, 1.5-GHz CMOS low noise amplifier," *IEEE J. Solid-State Circuits*, vol. 32, no. 5, pp. 745-759, May 1997.
- [51] V. K. Dao, Q. D. Bui, and C. S. Park, "A multi-band 900MHz/1.8GHz/5.2GHz LNA for reconfigurable radio," *IEEE Radio Frequency Integrated Circuits Symposium*, pp. 69-71, 2007.
- [52] G. Sapone and G. Palmisano, "A 3 -10-GHz low-power CMOS low-noise amplifier for ultra-wideband communication," *IEEE Trans. Microw. Theory Tech.*, vol. 59, no. 3, pp. 678-686, Mar. 2011.
- [53] A. Bevilacqua and A. M. Niknejad, "An ultrawideband CMOS low-noise amplifier for 3.1-10.6-GHz wireless receivers," *IEEE J. Solid-State Circuits*, vol. 39, no. 12, pp. 2259-2268, Dec 2004.
- [54] F. Bruccoleri, E. A. M. Klumperink, and B. Nauta, "Wide-band CMOS low-noise amplifier exploiting thermal noise canceling," *IEEE J. Solid-State Circuits*, vol. 39, no. 2, pp. 275-282, Feb 2004.
- [55] K.-H. Chen and S.-I. Liu, "Inductorless wideband CMOS low-noise amplifiers using noise-canceling technique," *IEEE Trans. Circuits Syst. I, Reg. Papers*, vol. 59, no. 2, pp. 305-314, Feb. 2012.
- [56] B. van der Pol, "On oscillation hysteresis in a triode generator with two degrees of freedom," *Philosophical Magazine*, vol. 43, no. 256, pp. 700-719, Apr 1922.
- [57] J. Schaffner, "Simultaneous oscillations in oscillators," *IRE Trans. Circuit Theory*, vol. CT-1, no. 2, pp. 2-8, Jun. 1954.
- [58] H. J. Reich, J. G. Skalnik, and J. D. Crane, "Simultaneous oscillation at two or more frequencies," *Proc. IEEE*, vol. 51, no. 7, pp. 1051-1052, Jul. 1963.
- [59] G. Bertrand, A. Bonnot, and Capiomon.AI, "Simultaneous asynchronous oscillations in marginal oscillators," *IEEE Trans. Circuit Theory*, vol. 19, no. 3, pp. 271-277, Mar. 1972.

- [60] M. I. Disman and W. A. Edson, "Simultaneous asynchronous oscillations in Class-C oscillators," *Proc. IRE*, vol. 46, no. 5, pp. 895-903, May 1958.
- [61] N. M. Nguyen and R. G. Meyer, "Start-up and frequency stability in high-frequency oscillators," *IEEE J. Solid-State Circuits*, vol. 27, no. 5, pp. 810-820, May 1992.
- [62] L. V. Skinner, "Criteria for stability in circuits containing non-linear resistance," Ph.D. dissertation, University of Illinois, Urbana, IL, 1948.
- [63] H. Hashemi, "Integrated concurrent multi-band radios and multiple antenna systems," Ph.D. dissertation, California Inst. Tech., Pasadena, CA, 2003.
- [64] B. Soltanian and P. R. Kinget, "Tail current-shaping to improve phase noise in LC voltage-controlled oscillators," *IEEE J. Solid-State Circuits*, vol. 41, no. 8, pp. 1792-1802, Aug 2006.
- [65] A. Mazzanti and P. Andreani, "Class-C harmonic CMOS VCOs, with a general result on phase noise," *IEEE J. Solid-State Circuits*, vol. 43, no. 12, pp. 2716-2729, Dec 2008.

## VITA

Xiaohua Yu received the B.E. degree in electronic information engineering from the University of Shanghai for Science and Technology, Shanghai, China, in 2005, the M.S. degree in electrical engineering from the Information and Communications University (now KAIST), Daejeon, South Korea, in 2008, and the Ph.D. degree in electrical engineering from Iowa State University, Ames, IA, in 2013.

From 2008 to 2010, he was with the Electronics and Telecommunications Research Institute (ETRI), Gwangju, South Korea, where he was involved in CMOS optical receiver integrated circuit (IC) design for 10G-EPON. His research interests include analog/RF circuits and devices for cognitive and reconfigurable radio and high-speed circuits.